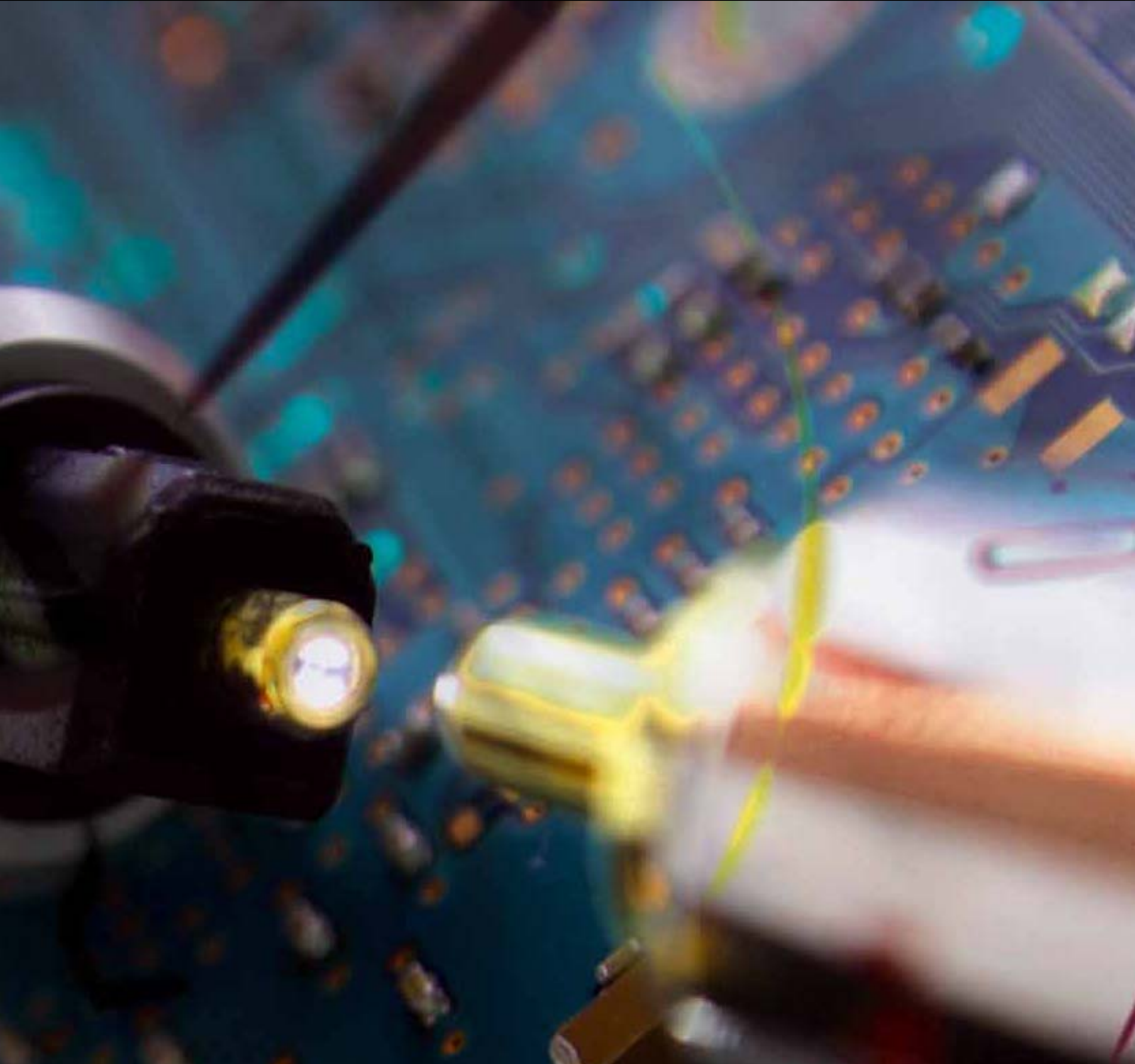# Nanomechanical Sensing

Guest Editors: Martin Hegner, Maria Tenje, and Sangmin Jeon

Nanomechanical Sensing

Nanomechanical Sensing

Guest Editors: Martin Hegner, Maria Tenje, and Sangmin Jeon

Editorial Board

Contents

Editorial
Nanomechanical Sensing

Martin Hegner,[1] Maria Tenje,[2] and Sangmin Jeon[3]

[1] *School of Physics, Center for Research on Adaptive Nanostructures and Nanodevices (CRANN), Trinity College Dublin, Dublin 2, Ireland*
[2] *Department of Measurement Technology and Industrial Electrical Engineering, Lund University, 221 00 Lund, Sweden*
[3] *Department of Chemical Engineering, Pohang University of Science and Technology, Pohang, Kyungbuk, Republic of Korea*

Correspondence should be addressed to Martin Hegner, martin.hegner@tcd.ie

Received 5 November 2012; Accepted 5 November 2012

This special issue represents the first proceedings of the 8th International Workshop Series on Nanomechanical Sensing (http://www.nmc2011.org/), which was hosted by the CRANN Institute of the Trinity College, Pearse street, Dublin 2, Ireland, from May 11th to May 13th 2011.

This meeting was a followup of workshops held in Madrid (2004), Knoxville (2005), Copenhagen (2006), Montréal (2007), Mainz (2008), Jeju (2009), and Banff (2010). At the conference in Dublin more than 120 researchers from all over the world gathered to report on their newest research in 57 talks in 11 different sessions. A poster session with 33 posters was held on the evening of the 11th of May. The workshop brought together companies and academia and provided lively debates in a personal atmosphere. The meeting focused on new developments, investigations, applications of cantilever-based sensors, cantilever systems engineering, and other nanomechanical sensing techniques (QCM, Nanowires and Graphene).

Nanomechanical sensors are an interesting new type of sensors (dimensions: nanometers to micrometers) that can detect biological species and trace elements in liquid and gaseous media when analysed differentially with an in situ-reference sensor. The main competitive advantages offered are label-free sensing and miniaturized size, which opens up for hand-held devices that can perform multiple detections simultaneously. The areas where nanomechanical sensors can see applications range from environmental monitoring (e.g., heavy-metal ion detection), via homeland security, to biomedical applications (e.g., DNA sequencing).

We would like to take this opportunity to thank all of the authors for their valuable contributions to make this special issue a reflection of the scientific excitement of the NMC2011 conference.

Martin Hegner
Maria Tenje
Sangmin Jeon

Research Article

Modelling of Atomic Imaging and Evaporation in the Field Ion Microscope

Keith J. Fraser and John J. Boland

School of Chemistry and CRANN, Trinity College Dublin, Dublin 2, Ireland

Correspondence should be addressed to Keith J. Fraser, fraserk@tcd.ie

Imaging and evaporation of atoms in the field ion microscope (FIM) has been modelled by using finite difference methods to calculate the voltage distribution around a tip and hence the electric field strength experienced by individual atoms. Atoms are evaporated based on field strength using a number of different mathematical models which yield broadly similar results. The tip shapes and simulated FIM images produced show strong agreement with experimental results for tips of the same orientation and crystal structure. Calculations have also been made to estimate the effects on resolution of using a field-sharpened tip for scanning probe microscopy.

1. Introduction

Field ion microscopy (FIM) has been used by several groups to examine and prepare tungsten tips for scanning tunnelling microscopy (STM) and atomic force microscopy (AFM) [1–3]. Field evaporation can produce a tip apex consisting of only a few atoms or even a single atom. The imaging resolution is reported to be improved through the use of tips sharpened in this way; however, this has generally not been quantified or investigated systematically. The forces measured in AFM operate over longer ranges than the tunnelling current measured in STM and are thus more sensitive to the atomic structure of the tip beyond the apex. Our aim is to numerically model field-induced tip sharpening in order to better understand the phenomenon and quantify the tip shapes produced, with a view to refining/designing scanning probe microscope (SPM) tip sharpening procedures and choosing the optimal materials.

Various theoretical studies have been carried out in the past on evaporation of atoms from tips under high electric fields; most of these have been aimed at simulating imaging in the 3D atom probe (e.g., the work of Geiser, Marquis et al. [4, 5]) and have therefore focused on the trajectories of evaporated ions rather than on the evolution of the atomic structure of the tip and its application to scanning probe microscopy. Our work builds on aspects of the approach of Vurpillot et al. [6], exploring alternative methods for determining which atoms undergo field evaporation and extending to different tip materials and orientations. *W* tips oriented along the 110 and 111 directions and Pt tips oriented in the 100 direction are discussed here. *W* tips are most commonly used in SPM, with the 110 orientation being observed in FIM experiments on tips made from polycrystalline wire and 111-oriented tips made from single-crystal wire being used in some experiments. Pt tips were considered due to future plans to use noble-metal-coated Si cantilever tips for combined AFM/STM.

2. Method

2.1. Overview. Here we introduce a modelling program capable of generating and simulating tips of different geometric shapes (including faceted tips) or materials and with different values of the aspect ratio between length and base radius. The tip surface and surrounding vacuum are modelled as a series of cells of fixed size—in contrast to the studies discussed above where the focus was on image formation, it was not necessary for this model to operate over large differences in length scale, so a variable mesh was not used.

| (a) | (b) | (c) |
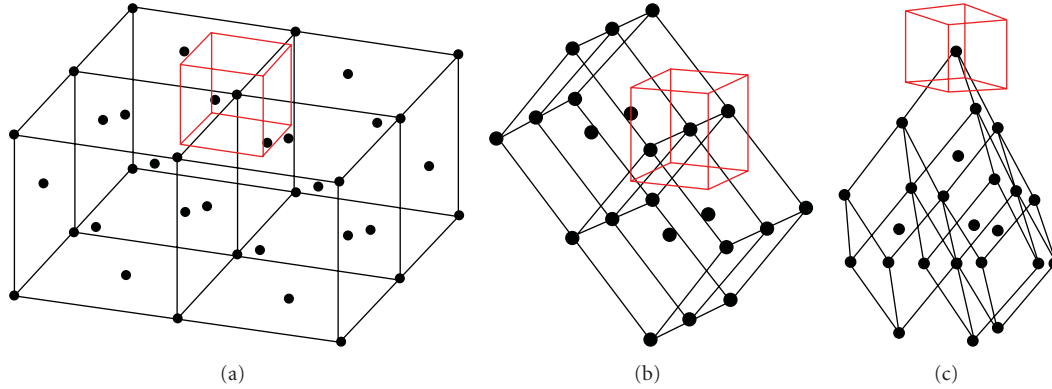
FIGURE 1: Illustration of cell shapes used for different crystal structures and orientations, compared with crystal unit cells: (a) face-centred cubic (100 orientation), (b) body-centred cubic (110 orientation), and (c) body-centred cubic (111 orientation). Atoms and unit cells shown in black; model cells shown in red.

Each cell is centred on an atomic site as shown in **Figure 1**. The cell shape and dimensions are dictated by the tip's crystal structure and orientation; the cell z-axis is oriented along the tip axis with the x- and y-axes defined by the shortest interatomic distances in the plane perpendicular to the tip axis. In simple cubic materials, each cubical cell (**Figure 1(a)**) contains one atom; in other crystal systems, some cells are empty due to the periodicity and the cell shape is different. In the 110 orientation, the cell is a cuboid (**Figure 1(b)**), while in the 110 orientation it is a prism where the base is a rhombus with an interior angle of $120°$.

The voltage distribution around the tip is calculated using a finite difference approximation in which the voltage within each cell is held constant. Within the tip surface, the voltage is set equal to the applied voltage V_0. Far from the tip, the voltage is set to zero. The voltage in the remaining cells is calculated using these boundary conditions and Poisson's equation ($\nabla^2 V = 0$). The resulting series of simultaneous equations is solved iteratively for the values of voltage in each cell. Steady state is deemed to have been reached when the deviation from Poisson's equation summed over all cells falls below a set threshold.

The electric field experienced by each atom at the tip surface is equal to the gradient of the voltage distribution ($F = \nabla V$) and is calculated under the finite difference approximation using the difference between voltage values in adjacent cells and the cell dimensions. When an atom chosen according to the criteria discussed below is evaporated from the tip surface, the voltage distribution is recalculated to steady state in all the cells, including those now outside the tip surface. This simulates the change in potential distribution caused by the removal of the evaporated atom.

The values of electric field calculated at each surface atomic site are also used to simulate a field ion image of the tip for comparison with experiment. Atoms experiencing a field above a set threshold are assumed to appear on a field ion image, which thus consists of a series of bright spots corresponding to these atoms (this does not take into account convolution of the image due to bending of the field lines near the tip). Scaling can be added to the image so that the brightness of individual atoms reflects the extent to which

○ $F > 0.9F_{max}$
◐ $F > 0.8F_{max}$
◔ $F > 0.7F_{max}$
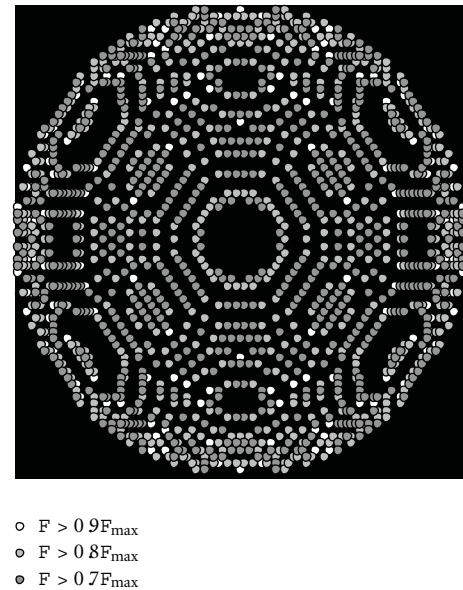
FIGURE 2: Schematic field ion image of a hemispherical 110-oriented W tip (radius ~8 nm, or 50 atomic spacings in the 100 direction) displaying surface atoms experiencing a field within the indicated bounds (expressed as a function of the maximum field).

the field they experience exceeds the threshold value (**Figure 2**). Images obtained in this fashion are only schematic as convolution due to variations in ion trajectory between the tip, and FIM screen is not taken into account.

To allow larger tips to be modelled in acceptable lengths of time, tip symmetry is used as a means of reducing the number of calculations carried out per iteration when solving for the steady-state voltage distribution. 100- and 110-oriented tips have 4-fold symmetry, while 111-oriented tips have 3-fold symmetry. As a result, only just over 1/4 or 1/3 of the tip need be considered by the model.

Processing speed is also increased by initially treating the tip as radially symmetric and modelling the voltage distribution up to steady-state using cylindrical coordinates. The results are then converted into a three-dimensional coordinate

system and recalculated to steady-state before beginning field evaporation. Only cells within a set distance of the tip surface are converted in this way, reducing the overall number of cells and again increasing the tip size that can be simulated; the voltage outside this region is assumed to remain constant during evaporation. This approximation is found not to significantly affect results provided the cutoff distance is set high enough.

2.2. Field Evaporation Mechanisms. In the simplest form of the model, the surface atom chosen for evaporation is the one which experiences the highest field [6]. This method does not calculate the time between evaporation events or adjustments in the applied voltage; it therefore provides less information about the evaporation process to compare with experimental results. A more sophisticated, time-dependent approach is to calculate the effect of the field on the activation energy for field evaporation. Several mathematical models exist for this [7]; in this work, those used were the image-force model [8] and the approach of Kreuzer and Nath using the universal binding-energy curve [9]. These models use approximations that do not reflect the true nature of the tip surface (e.g., the image-force model is based on the removal of an ion from a flat surface under a field that is constant with distance), but have been found to produce results consistent with experiment for some materials.

Under the image-force model, the activation energy E_A at field F for an n-fold charged ion is given by (1), where Λ is the heat of sublimation of a neutral atom (also known as the cohesive energy), I_n is the nth ionization energy, and Φ_e is the work function. A polarization term $c_a F^2$ can optionally be included [7], where c_a is an empirical coefficient with a value of around $1\,\mathrm{meVnm^2V^{-2}}$:

$$E_A = \Lambda + \sum_n I_n - n\Phi_e - \sqrt{\frac{n^3 e^3 F}{4\pi\varepsilon_0}}. \tag{1}$$

The approach of Kreuzer and Nath, shown in (2), expresses the activation energy in terms of the parameter $\delta = F/F_{\mathrm{ev}}$, where F_{ev} is the value of field at which $E_A = 0$. F_{ev} can be calculated for a given material using (3), where λ is the Thomas-Fermi screening length

$$\frac{EA}{\Lambda} = \delta^{1/2} + \frac{1}{2}(1-\delta)\ln\left(\frac{1-\delta^{1/2}}{1-\delta^{1/2}}\right), \tag{2}$$

$$F_{\mathrm{ev}} = \frac{3\Lambda}{2ne\lambda}. \tag{3}$$

When the activation energy for field evaporation is calculated using (1) or (2), the probability of evaporation for a given atom in the interval between time t and time $t+\tau_0$, where τ_0 is the inverse of the atomic vibration frequency, is given by the expression $p = \exp(-E_A/kT)$, based on the evaporation rate formula $R = (1/\tau_0)\exp(-E_A/kT)$ [8]. To take into account changes in local field as the voltage is ramped and/or atoms evaporate, a cumulative probability is recorded as time passes for each surface atom. Once this probability reaches 1, the atom is evaporated and the cumulative value reset to zero for the newly revealed atom below.

At present, it is assumed that the energy barrier for field evaporation is the same for all atoms. In real materials, the zero-field evaporation energy will vary. Calculating the binding energy for every atom on the tip surface would be highly complex for a tip of significant size; differences in binding energy may be approximated with a simple weighting function that adjusts the value depending on the number of adjacent atoms. A similar approach was used by Vurpillot et al. [6] to simulate evaporation from a tip made up of more than one element.

The different mechanisms are found to produce similar but not identical results. The applied voltage at which evaporation begins to occur varies between the three time-dependent methods; the polarization term in the image-force model increases this threshold by $\sim$20% in the case of $W(110)$ tips, whereas the value under the Kreuzer-Nath model depends on the set value of evaporation field. The single-atom tip (SAT) produced for a tip of a given starting size and shape looks almost exactly the same regardless of which criteria are used (Figures 3(a)–3(d)). The principal difference between the methods is the stability of the single-atom tip. The image-force model and to a lesser extent the Kreuzer-Nath model predict the SAT to persist for a relatively high number of evaporation events before the apex atom is lost, whereas evaporation at highest field predicts that the single-atom tip will be lost almost immediately after forming.

Figures 3(e)–3(h) show the formation of a SAT produced on a polycrystalline W sample which persisted for $\sim$30 s before the voltage was turned down. The dot at the centre of the tip apex in Figures 3(g)–3(h) is assumed to be a single atom rather than a cluster as the same structure was seen in separate experiments and for successive evaporations of layers of material, with the dot disappearing in a single evaporation event. Atoms were observed to evaporate from below the apex during this period, as predicted by the time-dependent models, suggesting that as expected, these models better simulate real field evaporation behaviour. All the results presented in the rest of this paper use the image-force method without polarization.

2.3. Simulating Effect of Tip Sharpening on SPM Resolution. Since the purpose of this work is to investigate the production of sharpened SPM tips using field evaporation, a method is required to quantify the expected effect of a given tip shape on SPM resolution. This is accomplished by calculating the variation of the interatomic force or tunnelling current as the tip is scanned over a feature on a flat surface and using the results to create a schematic AFM or STM image. The signal can be plotted directly to simulate scanning in constant-height mode, or the scan height can be adjusted as a function of position to create a topographical image.

The force between the tip and sample is calculated using the 8-6 Lennard-Jones potential (4), where the negative term represents the attractive van der Waals force, while the positive term is an empirical representation of the electrostatic repulsion. The 8-6 potential was used in preference to the 12-6 potential as it is less computationally expensive and is considered more suitable for nonbonding interactions [10].

(a)

(b)

(e)

(f)

(c)

(d)

(g)

(h)
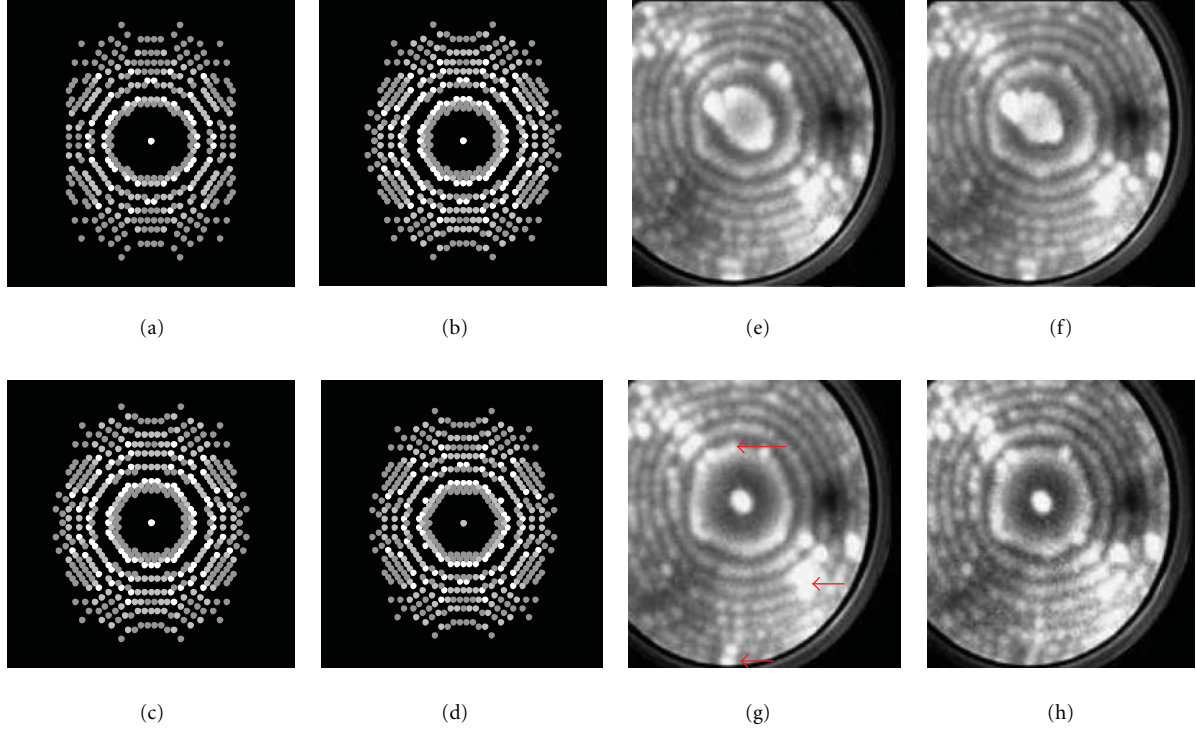
FIGURE 3: (a–d) Schematic field ion images of single-atom $W(110)$ tips produced from a hemispherical starting tip (radius 8 nm) via field evaporation according to highest-field, image-force (with/without polarization), and Kreuzer-Nath criteria; (e–h) experimental field ion images (voltage ~8.8 kV) showing the formation of an SAT and evaporation of atoms from below the apex. Arrows indicate features which change between (g) and (h).

The quantity r is the distance between the atomic centres, and r_m is a factor denoting the distance at which the energy reaches a minimum, set to 3 Å in all the calculations used here. The vertical force acting between the two atoms is given by $-\delta E/\delta z$. The resulting force between each atom in the tip and each atom in the imaged feature is calculated and added to the total force. The surface below is considered to have uniform atomic density, and the force is integrated over and through it in all directions to calculate the "background" signal for each tip atom which is added to the total force. The remainder of the tip shank above the portion of the tip modelled on the atomic scale is also factored in the longer-ranged attractive force which is integrated over a uniform truncated cone and over and through the surface,

$$E \propto \frac{3}{4} \frac{r_m^2}{r^8} - \frac{1}{r^6}. \tag{4}$$

The tunnelling current across a gap s is given by (5), where $\kappa = [m_e(V - E)e]^{0.5}/\hbar$; m_e is the electron mass and $V - E$ (taken as 4 eV) is the tunnelling barrier height. For the purposes of calculating tunnelling current, the tip and sample atoms are considered to be spheres with radii based on the interatomic distance in the crystal lattice, and s is the edge-to-edge distance between two atoms (i.e., the centre-to-centre distance minus the sum of their radii). To calculate the total current, (5) is used to calculate the current through each

imaged atom and integrated over the sample surface for each atom on the tip surface,

$$I \propto \exp(-2\kappa s). \tag{5}$$

The results are shown in Figure 4 for the imaging of a single-raised atom on a flat surface by two $W(110)$ tips of similar size, one hemispherical with a flat apex and the other an idealized cone with a single-atom apex. The setpoint in AFM mode is defined as the point of maximum attractive force (i.e., the point where the total force is a minimum). This was chosen as the simplest method of maintaining a short-tip-sample separation. The setpoint current in STM mode was the same for both tips. In both modes, the conical tip gives vastly superior lateral resolution and increased vertical displacement. The latter indicates that the imaged atom produces a greater perturbation in the force or tunnelling current signal relative to the background signal from the underlying surface, which will lead to improved experimental signal-to-noise ratios. The hemispherical tip produces an image of the atomic corrugation of its apex rather than of the sample atom (image convolution) due to each apex atom interacting with the sample atom as they pass over it. The perturbation to the total signal due to the sample atom, and thus the vertical displacement, is smaller due to the larger number of atoms in the blunt tip producing a larger background signal.

(a) Hemispherical tip

(b) Conical tip

(c) AFM (hemispherical tip)

(d) AFM (conical tip)

(e) STM (hemispherical tip)

(f) STM (conical tip)
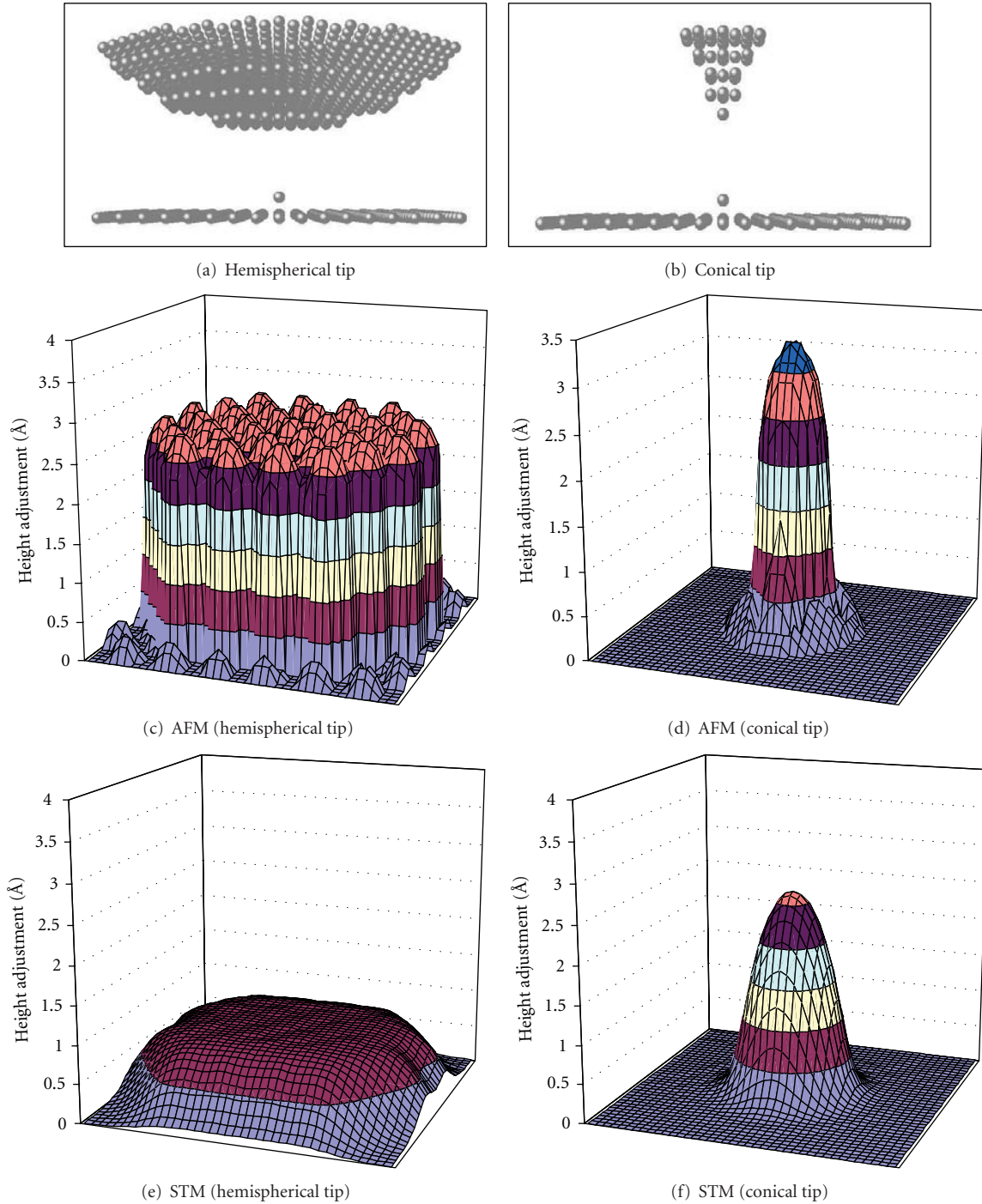
FIGURE 4: (a, b) Atomic structures of hemispherical and conical (aspect ratio = 1) 110-oriented W tips (radius 3 nm, lowest 5 atomic layers shown) scanning over a raised atom on a flat plane. Interatomic distances are to scale (sample atomic spacing = 2.5 Å); for clarity, tip-sample separation is larger than used in calculations and atoms are shown smaller than their derived radii. (c, d) Topographical images produced by simulated imaging of sample atom and surface in AFM mode by hemispherical and conical tips (setpoint defined as point of maximum attractive force). (e, f) Topographical images produced by simulated imaging of sample atom and surface in constant-current STM mode (same setpoint) by hemispherical and conical tips. Scanned area: 20×20 Å^2.

3. Results

3.1. Effect of Tip Size on Electric Field. The electric field F at the surface of a charged sphere of radius r at voltage V is given by the relation $F = V/r$. For a hemispherical tip at

the end of a long shank, the relation is modified to $F = V/kr$ [8]. Lucier et al. [11] correlated the radii of W STM tips (measured using scanning electron microscope images) with the best imaging voltage and estimated a value of k of 3.3–3.4 for annealed tips with radii of 20–40 nm. Evaporation

(a)

(b)
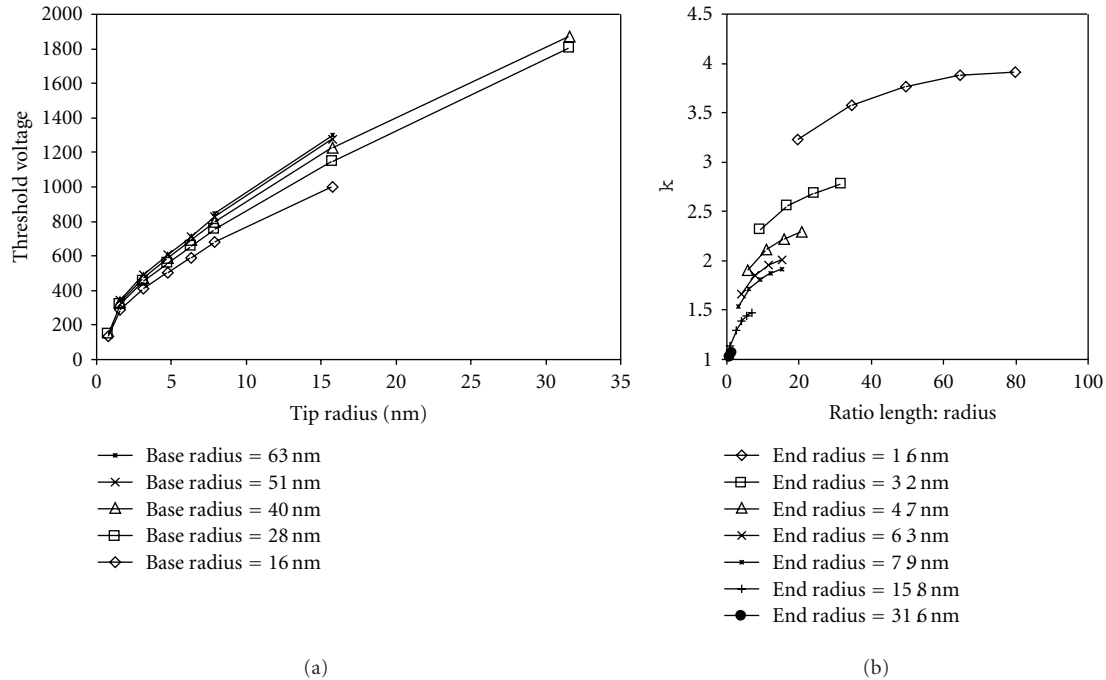
FIGURE 5: (a) Values of field evaporation threshold voltage for $W(110)$ tips consisting of a hemisphere on top of a conical shank for different shank and hemisphere sizes (b) effective values of field reduction factor κ as a function of the ratio of tip length to end radius. Cone aspect ratio = 1 (opening angle $51.2°$).

(a)

(b)

(c)
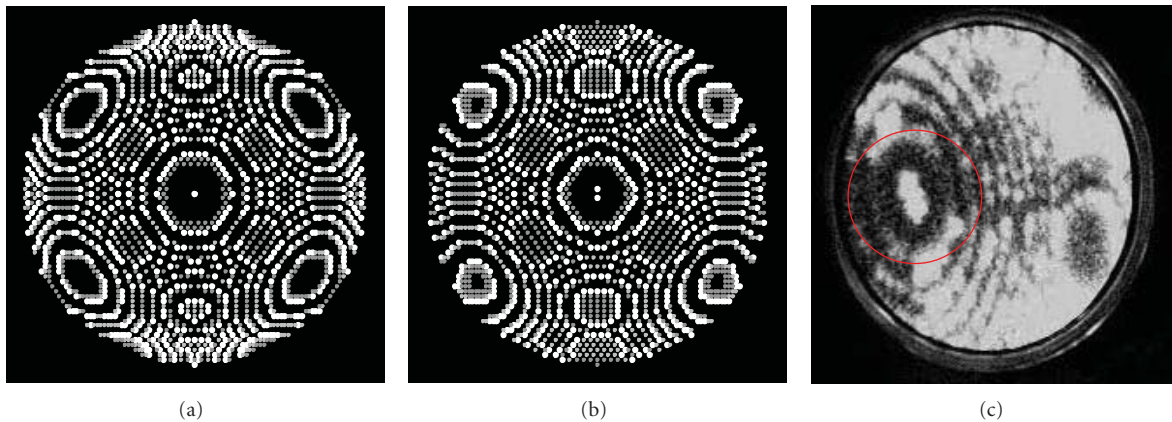
FIGURE 6: (a, b) Schematic FIM images of 110-oriented hemispherical W tip (radius 8 nm) subjected to field evaporation (image-force model) without polarization component) at 77 K, single-atom and double tip; (c) experimental image of polycrystalline W tip (apex circled) imaged at 77 K, 8.0 kV.

and imaging took place from 2.4–6.2 kV. This is consistent with our experiments and other results from the literature—in general, where field evaporation is possible, it is carried out in the regime 10^3–10^4 V with sharper tips requiring lower voltages.

Figure 5(a) shows the applied voltage required for field evaporation (based on the value at which the activation energy equals zero under the image-force model) of conical $W(110)$ tips with a hemispherical cap under the model. The threshold voltage rises linearly with increasing end radius as expected (except for very small tips), and increases with the shank size. The effective value of k increases nonlinearly

with the ratio of tip length to end radius (Figure 5(b)). For larger tips comparable to those examined by Lucier et al., the threshold voltage is at the lower end of the expected range and can be expected to rise for tips with larger radii or longer shanks (modelling of larger structures than those used to generate the data in Figure 5 is very time-consuming and was therefore not carried out).

Notably, although the size of the shank strongly affects the strength of the electric field around the tip, the field distribution near the apex is found to be very similar regardless of whether or not a long shank is present. Field evaporation therefore tends to remove the same atoms from the apex,
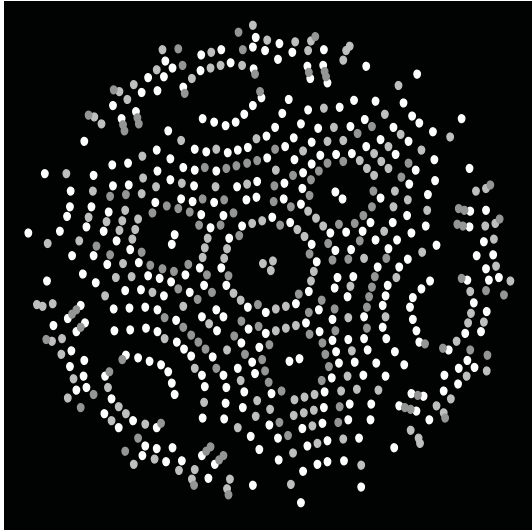
FIGURE 7: Schematic FIM image of 111-oriented hemispherical W tip (radius 13 nm) subjected to field evaporation at 77 K (image-force model without polarization component).
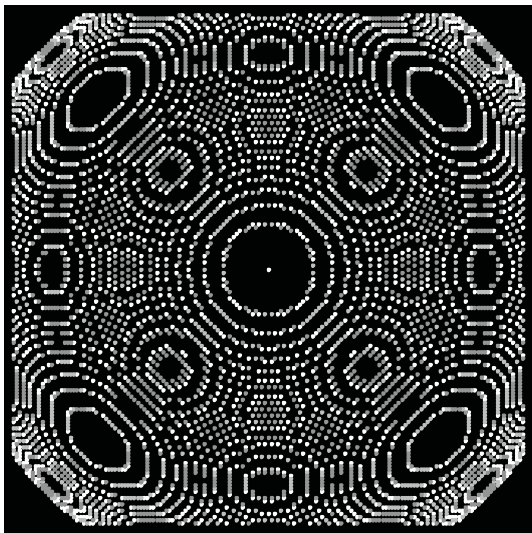
FIGURE 8: Schematic FIM image of 100-oriented hemispherical Pt tip (radius 16 nm) subjected to field evaporation at 77 K (image-force model without polarization component).

giving rise to the same configurations. Hence, the results presented below for the shapes of field-evaporated tips were derived from hemispherical tips without a large shank.

3.2. Evaporated Tip Structures for Different Materials. Figures 6–8 show schematic FIM images for three different types of tip subjected to field evaporation. Structures similar to those seen in the literature [1–3, 12–16] and our own experiments (Figure 6(c)–compare Figure 6(b)) are found, including faceting along close-packed crystal directions. SATs where the apex atom lies atop a flat terrace can be formed from $W(110)$ (Figure 6(a)) and Pt(100) (Figure 7), again as seen experimentally (Figure 3(c)). A symmetrical single-atom

apex cannot be formed on $W(111)$—the sharpest symmetrical configuration is a trimer (Figure 8). If the tip is modelled in its entirety rather than using 3-fold symmetry, the atoms of the trimer can be removed one by one to produce an asymmetrical single-atom apex [14]. This again mirrors experimental results in the literature—a pyramidal apex consisting of a single atom atop the trimer can be formed by, for example, chemically etching the tip at high voltage [15] or depositing atoms from the gas phase [16], but not by field evaporation. This correspondence with well-documented experimental results confirms the validity of the model.

Simulations of the effect on STM and AFM resolution of using field-sharpened tips compared to their preevaporated forms are presented as supplementary material.

4. Conclusions

Field evaporation of atoms in the field ion microscope is simulated using an iterative finite difference method that builds on the work of Vurpillot et al. [6]. Our model differs from other work on simulation of FIM and atom probe experiments [4–6] due to its focus on field evaporation and changes in tip structure rather than on the trajectories of emitted ions. Mathematical models of field evaporation taken from the literature are compared, and it is found that the time-dependent kinetic models used all produce similar results which match experimental observations more closely than the simpler method used by Vurpillot et al. The field-evaporated endforms of tips made from materials suitable for SPM are modelled, with results in reasonable agreement with those seen experimentally in our own work and in the literature. The effect of field-induced tip sharpening on tip convolution in scanning probe microscopy is also simulated.

The simulation methods developed in this work are expected to be very useful in future STM/AFM experiments. In addition to aiding in the production of single-atom tips for improved resolution, it is hoped that improved understanding of the structure of such tips will aid the measurement and understanding of surface forces at an atomic level. If the surface atomic structure is determined by STM and the tip structure by FIM, then simulations of the interatomic forces can be refined via comparison with simultaneously gathered AFM data. In this way, more accurate mathematical models of surface forces may be produced.

Acknowledgments

References

[1] Y. Kuk and P. J. Silverman, "Role of tip structure in scanning tunneling microscopy," *Applied Physics Letters*, vol. 48, no. 23, pp. 1597–1599, 1986.

[2] A. Fian and M. Leisch, "Study on tip-substrate interactions by STM and APFIM," *Ultramicroscopy*, vol. 95, pp. 189–197, 2003.

 [3] T. An, T. Eguchi, K. Akiyama, and Y. Hasegawa, "Atomically-resolved imaging by frequency-modulation atomic force microscopy using a quartz length-extension resonator," *Applied Physics Letters*, vol. 87, no. 13, Article ID 133114, pp. 1–3, 2005.

 [4] B. P. Geiser, D. J. Larson, S. S. A. Gerstl et al., "A system for simulation of tip evolution under field evaporation," *Microscopy and Microanalysis*, vol. 15, supplement 2, pp. 302–303, 2009.

 [5] E. A. Marquis, B. P. Geiser, T. J. Prosa, and D. J. Larson, "Evolution of tip shape during field evaporation of complex multilayer structures," *Journal of Microscopy*, vol. 241, no. 3, pp. 225–233, 2011.

 [6] F. Vurpillot, A. Bostel, and D. Blavette, "A new approach to the interpretation of atom probe field-ion microscopy images," *Ultramicroscopy*, vol. 89, no. 1–3, pp. 137–144, 2001.

 [7] R. G. Forbes, "Field evaporation theory: a review of basic ideas," *Applied Surface Science*, vol. 87-88, pp. 1–11, 1995.

 [8] M. K. Miller, A. Cerezo, M. G. Hetherington, and G. D. W. Smith, *Atom Probe Field Ion Microscopy*, Oxford Science Publications, 1996.

 [9] H. J. Kreuzer and K. Nath, "Field evaporation," *Surface Science*, vol. 183, no. 3, pp. 591–608, 1987.

[10] D. N. J. White, "A computationally efficient alternative to the Buckingham potential for molecular mechanics calculations," *Journal of Computer-Aided Molecular Design*, vol. 11, no. 5, pp. 517–521, 1997.

[11] A. S. Lucier, H. Mortensen, Y. Sun, and P. Grütter, "Determination of the atomic structure of scanning probe microscopy tungsten tips by field ion microscopy," *Physical Review B*, vol. 72, no. 23, Article ID 235420, pp. 1–9, 2005.

[12] G. Cross, A. Schirmeisen, A. Stalder, P. Grütter, M. Tschudy, and U. Dürig, "Adhesion interaction between atomically defined tip and sample," *Physical Review Letters*, vol. 80, no. 21, pp. 4685–4688, 1998.

[13] T. V. de Bocarmé, T. D. Chau, and N. Kruse, "Imaging and probing catalytic surface reactions on the nanoscale: Field Ion Microscopy and atom-probe studies of O_2–H_2/Rh and NO–H_2/Pt," *Topics in Catalysis*, vol. 39, pp. 111–120, 2006.

[14] K. Motai, T. Hashizume, H. Lu, D. Jeon, T. Sakurai, and H. W. Pickering, "STM of the Cu(111)1 × 1 surface and its exposure to chlorine and sulfur," *Applied Surface Science*, vol. 67, no. 1–4, pp. 246–251, 1993.

[15] F. Rahman, J. Onoda, K. Imaizumi, and S. Mizuno, "Field-assisted oxygen etching for sharp field-emission tip," *Surface Science*, vol. 602, no. 12, pp. 2128–2134, 2008.

[16] H. W. Fink, "Mono-atomic tips for scanning tunneling microscopy," *IBM Journal of Research and Development*, vol. 30, p. 460, 1986.

Research Article

Cell Proliferation Tracking Using Graphene Sensor Arrays

Ronan Daly,[1] Shishir Kumar,[1] Gyongyi Lukacs,[2] Kangho Lee,[1] Anne Weidlich,[1] Martin Hegner,[2] and Georg S. Duesberg[1]

[1] *CRANN and School of Chemistry, Trinity College Dublin, Dublin 2, Ireland*
[2] *CRANN and School of Physics, Trinity College Dublin, Dublin 2, Ireland*

Correspondence should be addressed to Ronan Daly, dalyr1@tcd.ie and
Martin Hegner, martin.hegner@tcd.ie

The development of a novel label-free graphene sensor array is presented. Detection is based on modification of graphene FET devices and specifically monitoring the change in composition of the nutritive components in culturing medium. Micro-dispensing of *Escherichia coli* in medium shows feasibility of accurate positioning over each sensor while still allowing cell proliferation. Graphene FET device fabrication, sample dosing, and initial electrical characterisation have been completed and show a promising approach to reducing the sample size and lead time for diagnostic and drug development protocols through a label-free and reusable sensor array fabricated with standard and scalable microfabrication technologies.

1. Introduction

Controlled monitoring of bacterial growth has long been essential both as a diagnostic tool and as a standard drug development testing procedure. Common laboratory techniques involve bacterial proliferation on a Petri dish or in solution, providing an excess supply of nutrition and a controlled environment while sampling regularly for parallel tests by optical techniques. The need for higher throughput testing, more rapid diagnoses, and a more efficient use of samples has led to the implementation of miniaturised well-plate techniques. However, the drive for continuous improvement along with the concurrent growth in nanotechnology has led to a paradigm shift in sensing of biological activity. Significant advances in the coupling of proliferation to microcantilever [1–3] or quartz crystal microbalance (QCM) [4, 5] measurements have shown the potential for sensitivity to ultrasmall quantities of cells. In this work we are focused on the incorporation of graphene into label-free field effect transistor (FET) sensors to offer an alternative path to monitoring cell growth. In the approaches mentioned, it is the bacterium, the least abundant component, that acts as the analyte. Here we present initial results for the development of a novel label-free sensor for biological activity and specifically cell proliferation that relies upon measuring the change in the components of the bulk nutritive liquid. We propose the use of a scalable graphene FET microfabrication technology to (i) grow graphene films by chemical vapour deposition, (ii) transfer them to functional substrates and (iii) microstructure and contact graphene devices. These graphene FETs are functionalised by direct microdispensing of biological materials. We show initial evidence for cell proliferation on the microfabricated devices and the change in graphene charge transport responses with concentration changes of the lysogeny broth (LB) medium. This provides the basis for a scalable system allowing *in situ* tracking over the culture lifecycles in a range of parallel devices without the need for repeated sampling.

For diagnostics and drug development, one of the key drivers in sensor development is the reduction of the required sample volume. In a similar way that Moore's law drives the trend in decreasing transistor size for optimised device speed, there is a consistent decrease in sensor dimensions used for detecting proliferating bacteria. It has been noted in the literature that with a decrease in sample volumes there is an expected decrease in testing time. This is due to a number of factors, including the more rapid diffusion of nutrients because of the exponentially smaller system dimensions and the increased sensitivity requiring fewer lifecycles before detection occurs. This has been exploited
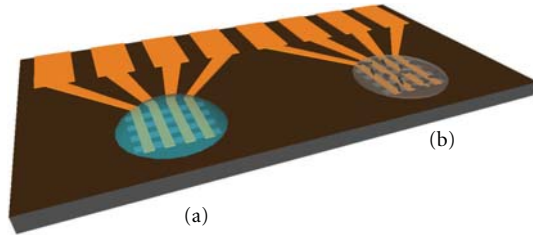
FIGURE 1: Metal electrodes contacting an underlying graphene layer acting as a sensor device with (a) bacteria proliferation occurring within a dosed volume of LB medium and (b) bacteria proliferation occurring on a thin agar layer, filled with a nutritive medium.

previously using micromechanical approaches, for example, by Gfeller et al. [1] where bacteria grew on an agar layer of a microcantilever array. However, these methods still have some drawbacks, namely, multistep fabrication techniques with limited device reusability and intricate surrounding measurement apparatus. For the devices proposed in this work, as shown in Figure 1, the sensor area is in complete contact with the sample and, through rapid diffusion and convection in such small sample volumes, is expected to be highly sensitive to changes. Large arrays of these sensors enable multiple parallel testing and improvement of the statistical confidence while still decreasing the batch time and conserving the low sample volume requirements. The robust nature of the graphene FETs allows repeated cleaning and reuse while the output is a simple electrical resistance measurement in the kΩ range. In standard laboratory techniques and the microfabricated devices shown in Figure 1, LB is used as a feedstock to promote the binary fission process and bacterial growth on an agar layer or in solution. The nutrition contained within the aqueous broth includes vitamins, minerals, and organic compounds such as amino acids all of which are essential to the proliferation and growth of *Escherichia coli (E. coli)*, the bacteria examined in this report.

The growth of cells is most often monitored by optical density (OD) measurements, where light absorption is used to identify the presence of bacteria in suspension. There are bulk-scale techniques to monitor the change in the LB content as a means to understanding the growth rate of bacteria. These track solution conductivity, pH, or fluorescence [6], but there are to-date limited attempts to scale this approach down to microscale arrays and to our knowledge no attempts to incorporate two-dimensional carbon sensors for this purpose. The unique electrical and mechanical properties of graphene lend themselves to incorporation into FET devices in this case. The relative freedom from catalytic impurities, the low levels of noise, flexibility, robustness, and ease of microstructuring have all been noted [7] as benefits to using this material as an ultrasensitive recognition element in biosensor devices. Such devices have proven effective in air and liquids for the sensing of individual gas molecules [8], proteins [9], and bacteria [10] when direct graphene-analyte interactions occur. The direct contact is believed to lead to charge transfer and hence a change in the electrical response of the graphene sheet.

2. Experimental Details

2.1. Sensor Fabrication. Sensor devices are manufactured on 15×15 mm pieces of p-doped (Boron) silicon (100) with a 300 nm layer of SiO_2 from Si-Mat Silicon Materials, Germany, and cut using the Disco DAD 3220 wafer dicer. Samples are cleaned prior to microfabrication using ultrasonication in HPLC grade acetone, ultrasonication and rinse in HPLC grade propan-2-ol and subsequent drying in a rapid flow of filtered, dry nitrogen. An oxygen plasma treatment is also carried out to remove organic contamination using the Diener PICO barrel asher. Masks for UV lithography were designed in-house and created using the Heidelberg DWL 66FS direct writing system. UV lithography was carried out with the OAI Mask Aligner using Microposit S1813 positive photo resist and MF319 developer (both from Rohm and Haas Electronic Materials). Metal sputter deposition was carried out using the Gatan 682 Precision Etching Coating System at a rate of $0.1 \, \text{Å s}^{-1}$. After standard polymer lift-off procedures, residual polymer was removed by oxygen plasma treatment except when graphene was present, when solvent cleaning alone was used.

2.2. Graphene Transfer and Etching. Graphene, produced by chemical vapour deposition (CVD) as described in Results, is transferred from metal foil to the substrate as follows. A layer of poly(methyl methacrylate) (PMMA), (Mr-I 35 K PMMA from Microresist Technology GmBH) was spin coated on top of graphene film/copper foil pieces. Thermal-release tape was adhered on top of this PMMA support film, and the copper was then etched by floating the sample in etchant ($0.25 \, \text{M FeCl}_3 + 0.2 \, \text{M HCl}$). The resulting layered film of thermal-release tape/PMMA/graphene was cleaned with DI water, dried, and placed onto the substrate (as shown in Figure 3(b)). Because the graphene follows the contours of the PMMA/thermal-release tape layer, a uniform pressure was applied to the film to ensure close contact and conformation to the substrate. A range of pressures were used successfully ranging from 10 to 25 bar approximately. Heating the substrate from below promoted release of the upper tape layer. The remaining PMMA layer was removed by an initial soak in HPLC-grade acetone followed by an overnight soak in HPLC grade chloroform. The process can be carried out without thermal-release tape to avoid some contamination. In this case, PMMA-supported graphene is dredged from DI water onto the substrate. After the sample dries, PMMA can be removed as before.

2.3. Chemicals and Bacterial Culture. Chemicals and culturing medium were purchased from Sigma Aldrich (Arklow, Ireland) unless otherwise stated. *E. coli* CIP 53.126 was obtained from Collection de l'Institut Pasteur (Paris, France). Overnight cultures were prepared (200 rpm, 35°C, 15–18 h) in LB (1% NaCl, 1% tryptone, 0.5% yeast extract) from single colonies of *E. coli*. 1 mL of the overnight cultures were transferred into 30 mL of 50% LB, and 25% glycerol, 25% DI water and cultured (200 rpm, 35°C) for 110 min in order to reach a logarithmic growth rate. Glycerol was added
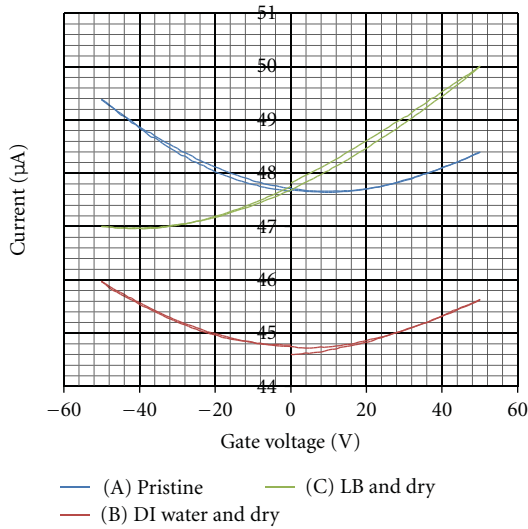
	Pristine	DI water	LB 1%$_{w/w}$	LB 10%$_{w/w}$	LB
Dirac point	+10 V	+4 V	−17 V	−34 V	−43 V

Figure 2: Performing gate sweep using back-gated graphene FET device shows that with exposure to LB medium there is a shift in the Dirac curve towards the negative bias voltage.

to ensure droplets did not evaporate prior to measurement. Observations confirmed evaporation was inhibited. Two additional diluted solutions were prepared from the LB stock. The first solution consisted of 500 μL LB, 250 μL glycerol, and 250 μL DI water. The second, more dilute solution consisted of 31 μL LB, 250 μL glycerol, and 469 μL deionised water (twice dilution and thirty-two times dilution, resp.). These are referred to as 2LB and 32LB in the text.

2.4. Microdispensing and Electrical Measurement. LB medium both with and without cells was dosed during this work using an Autodrop microdispensing system from Microdrop Technologies and a nozzle with a diameter of 50 μm. Subsequent electrical measurements on the graphene FET devices were carried out using a Keithley 2400 Sourcemeter attached to a Karl Suss probe station. Substrates were transferred between the dosing and measurement devices within a Petri dish containing a pad saturated with water to maintain humidity and inhibit evaporation of the dosed droplets during transport.

2.5. Additional Analysis. Raman spectroscopy was carried out using a Horriba Jobin Yvon LabRam HR system and a line of 632.8 nm. Scanning electron microscopy (SEM) was carried out using the Zeiss ULTRA Plus in the Advanced Microscopy Laboratory, CRANN, Trinity College Dublin. Prior to SEM imaging, bacteria were fixed by soaking in 5% v/v glutaraldehyde solution in 0.05 M phosphate buffer (pH7) and incubated at room conditions with gentle agitation for 3-4 h. Glutaraldehyde was then removed by 6 successive washes in fresh 0.05 M phosphate buffer, each of 10 minutes duration. Samples were subsequently dehydrated with a sequence of 10-minute rinses in 10, 30, 50, 70, 90, 100, and 100% v/v ethanol.

3. Results and Discussion

The fundamental premise of LB components affecting the conductance of graphene was confirmed using high-quality graphene flakes grown on Ni by chemical vapour deposition (CVD) and contacted with e-beam lithography. The graphene preparation and contacting process is described elsewhere [11]. The crucial step in this case is that the graphene has been cleaved by the Scotch tape to leave a clean surface. By dosing (i) 18 MΩ deionised water and (ii) LB medium onto a graphene FET device and comparing the electrical response of the sensor upon solvent evaporation, we see the precipitated materials from the LB medium lead to a slight increase in the measured resistance of the graphene strips and a clear shift in the Dirac point, as indicated in Figure 2. Graphene has linear dispersion in both valence and conduction bands. The degenerate point where these bands meet is known as the Dirac point. The Fermi level of graphene can move across the Dirac point under a bias, changing the concentration of charge carriers and therefore the resistance of samples. Thus, the minimum conductance (or maximum resistance) point observed in I–V characteristics displayed in Figure 2 corresponds to the Dirac point. A negative shift, as is observed for the samples exposed to LB, is equivalent to n-doping of the graphene.

With the development of a bulk graphene manufacturing technique, namely CVD, the incorporation of this remarkable material into scalable production of devices is now feasible [12]. The graphene used in this sensing application was grown by CVD, and all patterning was carried out by another scalable production technique, that of optical lithography. The CVD growth was carried out on 15 $\times$ 15 mm samples of copper foil in a tube furnace, as indicated in Figure 3(a) and described in detail in a separate publication [13]. For this work two techniques are detailed in the experimental section
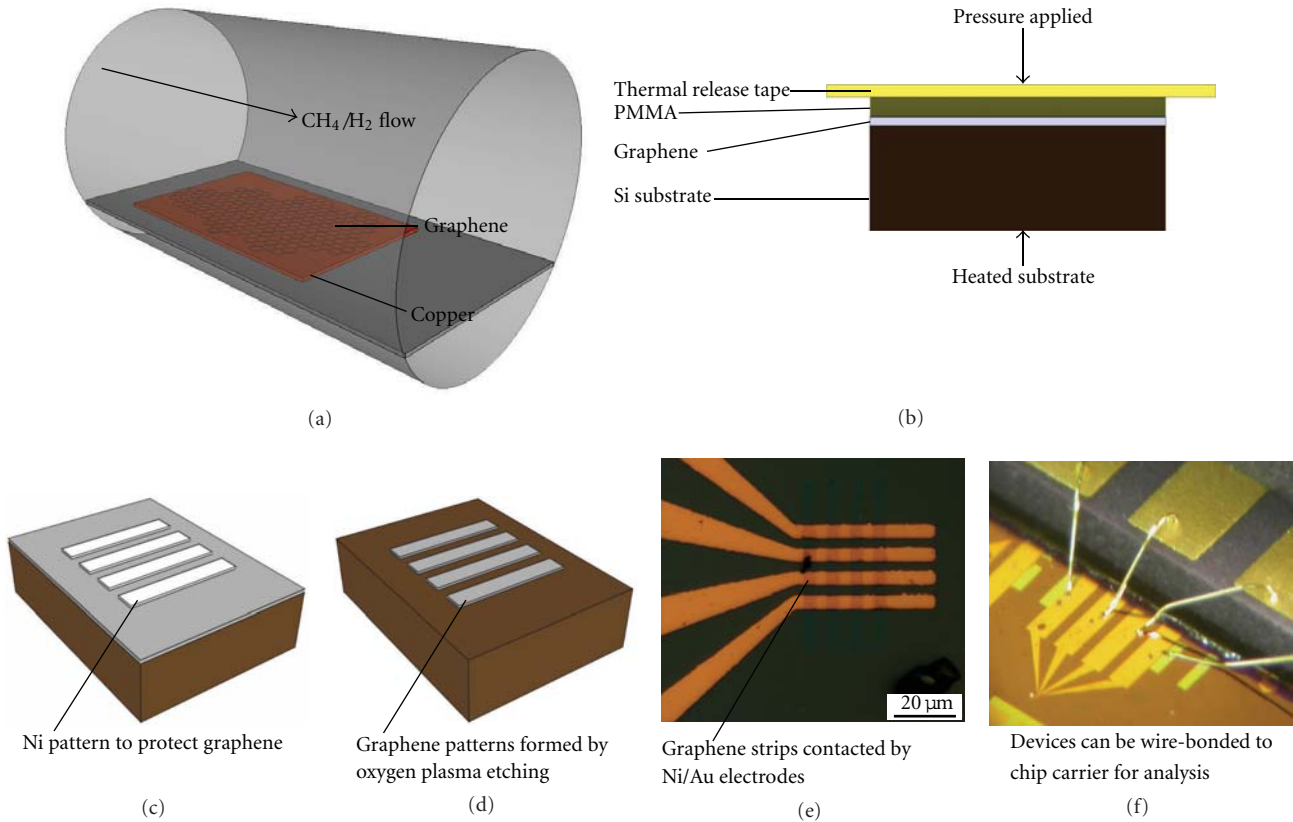
(a)

(b)

Ni pattern to protect graphene

(c)

Graphene patterns formed by
oxygen plasma etching

(d)

Graphene strips contacted by
Ni/Au electrodes

(e)

Devices can be wire-bonded to
chip carrier for analysis

(f)

FIGURE 3: Production and microfabrication of graphene. (a) CVD growth of graphene on copper foil in a tube furnace, (b) graphene is attached to SiO$_2$/Si by attaching to a support layer of PMMA and thermal-release tape and transferring by a combination of heat and pressure, (c) after transfer to SiO$_2$/Si substrate, a Ni protection layer is patterned on the graphene, (d) oxygen plasma removes the unprotected graphene and the Nickel is subsequently removed by HCl etching. (e) shows the contacted graphene strips and (f) shows integration of the sensor into a chip carrier.

attempting to optimise the transfer of approximately 15×15 mm films of graphene to the SiO$_2$/Si substrates. In summary, after coating the graphene film/copper foil pieces with a PMMA support layer and a further layer of thermal release tape, the copper can be removed by etching with FeCl$_3$. Transfer of graphene to SiO$_2$/Si substrates is completed by applying pressure through the tape and PMMA support layers, pressing the graphene surface onto the substrate as indicated in Figure 3(b). Heat applied through the substrate allows easy release of the thermal-release tape leaving behind the PMMA/graphene layers with the graphene adhering to the substrate very strongly by the van der Waals forces [14]. The PMMA can be removed with solvent cleaning. Due to concerns regarding contamination from the thermal-release tape and the fracturing effects of the mechanical transfer method, a second approach was developed. The PMMA support layer is still applied to the graphene film/copper foil pieces and the etching occurs as before at the liquid-air interface, leaving a graphene/PMMA layer floating on the surface. This is carefully transferred to the substrate surface through dip coating, and the same solvent cleaning steps occur to remove PMMA. The substrates have been prestructured by UV lithography with distinct, chromium alignment marks. These were included to enable a sequence

of UV lithography patterning steps to occur that lead to metal-contacted graphene strips with good adhesion to the substrate, using a technique described by Kumar et al., [13]. As shown in Figures 3(c)–3(f), a sacrificial masking pattern of nickel is formed to protect the areas required for the devices and the uncovered graphene is removed by an oxygen plasma. The nickel protection layers are then completely removed by an acid etch with 1 M HCl, and the remaining graphene strips are contacted by four Ni/Au electrodes ($4\,\mu$m/$48\,\mu$m) using a final UV lithography step. The contacted samples can then be probed directly using a needle prober or wire-bonded to a chip carrier for electrical measurements. This technique was modified from previous work to include a range of alignment marks for accurate positioning of all layers and a design that can be directly incorporated into an inkjet dosing system.

It is observed that the gate voltage behaviour and the scale of resistances recorded for graphene prepared with this technique have changed. This is partly due to the known issue of contamination during the incorporation of graphene into functional devices using multistep lithography processes. Graphene is notoriously difficult to maintain free of contamination and defects, and novel cleaning techniques will become essential for large-scale manufacture of graphene

(a)

(b)

(c)

- (A) Pristine
- (B) 3% v/v LB
- (C) 21% v/v LB
- (D) 29% v/v LB
- (E) 33% v/v LB
- (F) 36% v/v LB
- (G) 38% v/v LB

(d)
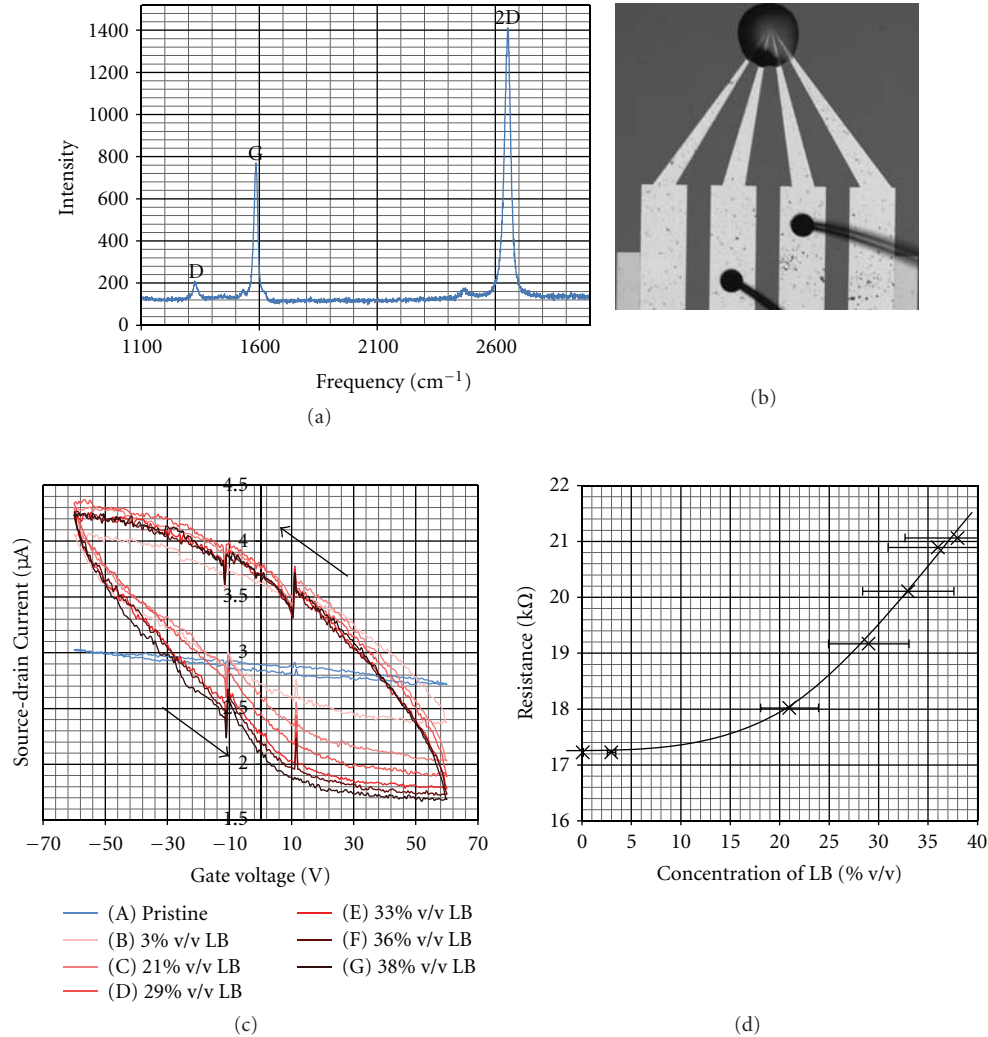
FIGURE 4: (a) Example of the Raman spectrum of CVD-grown graphene after transfer. (b) Controlled deposition of small volumes of LB/glycerol medium is shown to be accurate by optical microscopy. (c) The p-type behaviour of the pristine graphene is observed, and a clear increase in hysteresis is noted upon measurement of LB. A shift in gate dependency with LB concentration is also noted. The glycerol is added to reduce droplet evaporation and is maintained at the same concentration in each case. (d) A change in resistance with LB concentration is noted using two-probe measurements on the graphene FET. Error bars are calculated based on droplet repeatability findings by Lukacs et al. [19].

[15]. An example of the Raman spectrum of CVD growth of graphene on copper that was transferred to SiO$_2$ is shown in Figure 4(a). The G and 2D bands are clearly visible. The small bandwidth and the high 2D/G ratio are indicative of single-layer graphene [16]. A small D-band is also observed around 1350 cm^{-1} indicating some defects/disorder present in our samples. Also, the unintentional doping of graphene due to the local environment or the substrate is a known phenomenon [17] and an observed p-type gate dependence of graphene is often attributed to this environmental factor [18]. This p-type behaviour is indicated in our results for pristine graphene shown in Figure 4(c), while no distinct Dirac point is found in the given gate voltage range. To understand how this modified graphene behaviour translates to a liquid sensing environment, a 32 times diluted LB medium (as described in Section 2) was dosed onto

a sensor device using a microdispensing inkjet tool, as shown in Figure 4(b). To increase the LB concentration in this environment, additional drops were subsequently added containing a more concentrated solution (twice diluted LB). After each step change in concentration, the samples were transported to a probe station for electrical measurement as noted in Section 2.

A set of results using this method is presented in Figure 4(d). The increase in resistance with LB concentration is again noted. While intuitively, the inclusion of ions in solution would lead to a decrease in solution resistance, the observed increase in resistance with solution concentration is tentatively assigned to a charge transfer of negative charge from the LB solution to the graphene, counterbalancing its pristine p-type behaviour. This is consistent with the behaviour noted earlier for the dried LB scenario where there

(a)

(b)

FIGURE 5: Microdispensing of 50% LB/25% glycerol medium containing *E. coli* shows it is feasible to guide proliferation to the graphene sensor region. (a) An SEM image shows the graphene sensor and contacts at 80° tilt with a dense circular pattern of adhered bacteria fixed using a dehydration protocol and shown in (b) at a higher magnification.

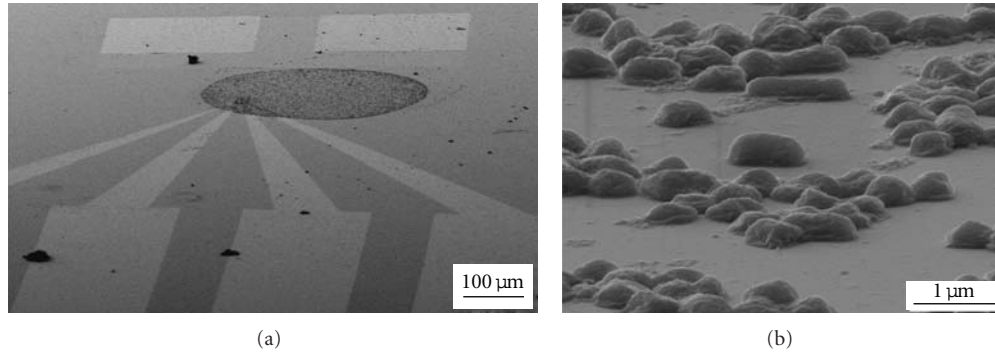is a shift in the Dirac point towards a negative gate voltage (Figure 2). As the result of this balance of charges, the system moves closer to neutrality and exhibits lower conductivity. Unlike single-molecule detection studies, the complexity of the medium does not allow a detailed interpretation. Each salt and biomolecule will contribute to the charge transfer in a different way, as will the balance struck between molecules converted to bacterial biomass and those excreted during proliferation. However, this initial approach allows insight into the potential sensitivity to changes in medium concentration.

With this proven ability to sense changes in a complex liquid system on top of graphene FET arrays, it was essential to show the capability to deliver *in situ* and localised bacteria proliferation. Through experiments microdispensing *E. coli* to sensor devices and comparing a device in an ambient atmosphere where the droplet is allowed to dry and a device maintained in an incubator for 1 day we show (i) survival of the *E. coli* through the dispensing protocol, (ii) no obvious ill effects of the substrate or possible contaminants from fabrication processes, and (iii) bacteria proliferation around the sensor area. Figure 5(a) shows an SEM image showing the dense drying pattern surrounding a graphene FET device made up of the *E. coli* shown in more detail by the second SEM image, see Figure 5(b). Imaging of the control and incubated samples shows an increase in cells/unit area by a factor of 8.6 over the course of 1 day. Fixation and drying steps, described in Methods, have been introduced to allow high-resolution images of cells in incubated samples.

4. Future Work and Conclusions

An optimised system for *in situ* electrical measurements is currently being developed. This has led to a system where both control and bioactive samples are dispensed within a single array and electrically analysed over the course of the experiment. Ongoing work is focusing on minimising background signals, optimising the device fabrication for high humidity environments and defining necessary sample concentrations to ensure a change within the detectable limits. As noted earlier, the rapid diffusion through such

small volumes and the sensitivity of graphene-based sensors are expected to ensure short batch times. Future work will include cell growth on a nanoscale agar-coating layer directly over the graphene device. This will reduce the sample volume significantly and is expected to ensure a rapid measurement of bacteria proliferation. More fundamental work is required to isolate the influences of each component in the LB medium to quantify the contributing factors to the measurements as the nutrition is converted to biomass. During the initial rapid-growth stage of the bacterial proliferation process that we are targeting, the cells grow at the maximum rate for a given medium using the nutrition to form bacterial biomass. While in this initial work we assume this to be the main influence on changes to the solution properties, it is known that a range of metabolites are also produced and excreted in this stage. It is well understood from the fermentation industry that once the proliferation slows, the production of metabolites also changes leading to a variation in pH [20]. In fact the biomass can be estimated by the progressive change in pH this process causes [21]. Planned work also includes examination of additional influences from biomolecules excreted from the proliferating bacteria.

We have shown the feasibility of a label-free micronscale graphene sensor array, fabricated with standard and scalable technologies, for monitoring the change in concentration of the nutritive medium used to promote bacteria proliferation. The introduction of different concentrations of nutritive medium could immediately be analysed with this novel electrochemical sensing method, and clear shifts in conductivity were detected in the liquid environment. The device has been tested in liquid and a surrounding humid environment and shows minimal drift that can in future be accounted for with additional control sensors. It is believed that the ability to microfabricate the sensors towards the length scale of individual bacteria will in future allow the targeting of just a few of the organisms, thus providing very specific and quantitative data. We have developed a fabrication, microdispensing, and analysis protocol for this novel sensing approach and demonstrated that the indirect measurement technique will be suitable for inexpensive, reusable, and rapid diagnostic tools.

Acknowledgments

References

[1] K. Y. Gfeller, N. Nugaeva, and M. Hegner, "Rapid biosensor for detection of antibiotic-selective growth of Escherichia coli," *Applied and Environmental Microbiology*, vol. 71, no. 5, pp. 2626–2631, 2005.

[2] D. Ramos, J. Tamayo, J. Mertens, M. Calleja, and A. Zaballos, "Origin of the response of nanomechanical resonators to bacteria adsorption," *Journal of Applied Physics*, vol. 100, no. 10, Article ID 106105, pp. 106105-1–106105-3, 2006.

[3] N. Nugaeva, K. Y. Gfeller, N. Backmann, H. P. Lang, H. J. Güntherodt, and M. Hegner, "An antibody-sensitized microfabricated cantilever for the growth detection of Aspergillus niger spores," *Microscopy and Microanalysis*, vol. 13, no. 1, pp. 13–17, 2007.

[4] N. Kim and I. S. Park, "Application of a flow-type antibody sensor to the detection of Escherichia coli in various foods," *Biosensors and Bioelectronics*, vol. 18, no. 9, pp. 1101–1107, 2003.

[5] X. L. Su and Y. Li, "A QCM immunosensor for Salmonella detection with simultaneous measurements of resonant frequency and motional resistance," *Biosensors and Bioelectronics*, vol. 21, no. 6, pp. 840–848, 2005.

[6] C. Faber, "Assessment of the inhibitory potency by MRI," in *NMR Spectroscopy in Pharmaceutical Analysis*, U. Holzgrabe et al., Ed., Elsevier, 2008.

[7] W. Yang, K. R. Ratinac, S. R. Ringer, P. Thordarson, J. J. Gooding, and F. Braet, "Carbon nanomaterials in biosensors: Should you use nanotubes or graphene," *Angewandte Chemie—International Edition*, vol. 49, no. 12, pp. 2114–2138, 2010.

[8] F. Schedin, A. K. Geim, S. V. Morozov et al., "Detection of individual gas molecules adsorbed on graphene," *Nature Materials*, vol. 6, no. 9, pp. 652–655, 2007.

[9] Y. Ohno, K. Maehashi, Y. Yamashiro, and K. Matsumoto, "Electrolyte-gated graphene field-effect transistors for detecting ph and protein adsorption," *Nano Letters*, vol. 9, no. 9, pp. 3318–3322, 2009.

[10] N. Mohanty and V. Berry, "Graphene-based single-bacterium resolution biodevice and DNA transistor: Interfacing graphene derivatives with nanoscale and microscale biocomponents," *Nano Letters*, vol. 8, no. 12, pp. 4469–4476, 2008.

[11] P. N. Nirmalraj, T. Lutz, S. Kumar, G. S. Duesberg, and J. J. Boland, "Nanoscale mapping of electrical resistivity and connectivity in graphene strips and networks," *NanoLetters*, vol. 11, pp. 16–22, 2011.

[12] X. Li, W. Cai, J. An et al., "Large-area synthesis of high-quality and uniform graphene films on copper foils," *Science*, vol. 324, no. 5932, pp. 1312–1314, 2009.

[13] S. Kumar, N. Peltekis, K. Lee, H. Kim, and G. S. Duesberg, "Reliable processing of graphene using metal etchmasks," *Nanoscale Research Letters*, vol. 6, no. 1, p. 390, 2011.

[14] J. S. Bunch, S. S. Verbridge, J. S. Alden et al., "Impermeable atomic membranes from graphene sheets," *Nano Letters*, vol. 8, no. 8, pp. 2458–2462, 2008.

[15] N. Peltekis, S. Kumar, N. McEvoy, K. Lee, A. Weidlich, and G. S. Duesberg, "The effect of downstream plasma treatments on graphene surfaces," *Carbon*, vol. 50, no. 2, pp. 395–403, 2012.

[16] A. C. Ferrari, J. C. Meyer, V. Scardaci et al., "Raman spectrum of graphene and graphene layers," *Physical Review Letters*, vol. 97, no. 18, Article ID 187401, 2006.

[17] Y. H. Wu, T. Yu, and Z. X. Shen, "Two-dimensional carbon nanostructures: fundamental properties, synthesis, characterization, and potential applications," *Journal of Applied Physics*, vol. 108, no. 7, Article ID 071301, 2010.

[18] H. E. Romero, N. Shen, P. Joshi et al., "n-type behavior of graphene supported on Si/SiO2 substrates," *ACS Nano*, vol. 2, no. 10, pp. 2037–2044, 2008.

[19] G. Lukacs, N. Maloney, and M. Hegner, "Ink-jet printing: perfect tool for cantilever array sensor preparation for microbial growth detection," *Journal of Sensors*. In press.

[20] M. Scheidle, B. Dittrich, J. Klinger, H. Ikeda, D. Klee, and J. Buchs, "Controlling pH in shake flasks using polymer-based controlled-release discs with pre-determined release kinetics," *BMC Biotechnology*, vol. 11, p. 25, 2011.

[21] M. L. Christensen and N. T. Eriksen, "Growth and proton exchange in recombinant Escherichia coli BL21," *Enzyme and Microbial Technology*, vol. 31, no. 4, pp. 566–574, 2002.

Research Article

Ink-Jet Printing: Perfect Tool for Cantilever Array Sensor Preparation for Microbial Growth Detection

G. Lukacs, N. Maloney, and M. Hegner

CRANN School of Physics, Trinity College Dublin, Dublin, Ireland

Correspondence should be addressed to G. Lukacs, lukacsg@tcd.ie

The use of microcantilever arrays for microbial growth detection provides a rapid and reliable technique for monitoring growth in industrial and clinical applications. Improving the reproducibility and sensitivity of this technique is of great importance. Ink-jet printing has been successfully used in microfabrication and biofabrication due to its high precision; however, only a few microbe-based applications have been reported. Here we demonstrate the advantages of its use for microcantilever based-growth sensing. Four microbial strains *Escherichia coli*, *Staphylococcus aureus* subsp. *aureus*, *Pseudomonas aeruginosa*, and *Candida albicans* were deposited and successfully grown on agarose-coated cantilevers by ink-jet printing. When compared to the capillary-coating method, ink-jet printing demonstrated more controlled cell deposition on cantilevers. The effect of various conditions on cell morphology was also investigated.

1. Introduction

The bioengineering fields of genomics, drug screening, tissue engineering, regenerative medicine, and various biosensor applications rely on biofabrication techniques which combine living and nonliving components deposited in a controlled manner. Bioprinting provides a rapid and reliable alternative to traditional methods giving the required spatial resolution for these applications [1]. Although biological structures are considered fragile, many studies have proven that ink-jet printing is feasible for a broad spectrum of biological material [2–6], and even more complex living systems such as cells can be deposited by this technique [7, 8]. Drop-on-demand bioprinters use different mechanisms to force the "bio-ink" through a microfluidic chamber to the output orifice [1]. Thermal ink-jet printheads use a heating element to raise the temperature in the reservoir creating a bubble which then forces a small amount of ink through the output orifice. In a piezoelectric printhead, a piezo actuator is supplied with short electrical pulses which are converted into short pressure pulses. These pulses propagate through the liquid. Due to inertia forces and supported by surface tension, a small volume of liquid breaks off the liquid

column to form a droplet. The droplet then flies freely with a velocity of 2-3 m/s. A pressure-driven printhead uses a pressure source behind the reservoir to produce a force on the liquid. A gate opens to allow ink to flow through the orifice [1]. It is clear that each of these approaches could damage the biomaterial by heat, electric field gradient, or pressure shock, and therefore, the range of working parameters must be optimised. Depending on the application, other issues such as nozzle clogging by cells or particles, aseptic printing, and aerosol formation have to be taken into account. Despite these problems, the spatial precision of the printed biomaterial renders these techniques highly advantageous for biosensing applications. Computer-controlled deposition offers a rapid functionalisation technique for micron-sized sensors such as cantilevers, quartz crystal microbalance (QCM), or surface plasmon resonance- (SPR) based sensing.

In this paper, we focus on microcantilever array functionalisation for cell-based sensor applications. Cantilever arrays operated in dynamic mode allow microbial growth analysis of various microbial cultures faster than conventional culturing techniques [9, 10]. This biological sensor is based on oscillating cantilevers, where additional mass loading onto the cantilever surface results in a change of its
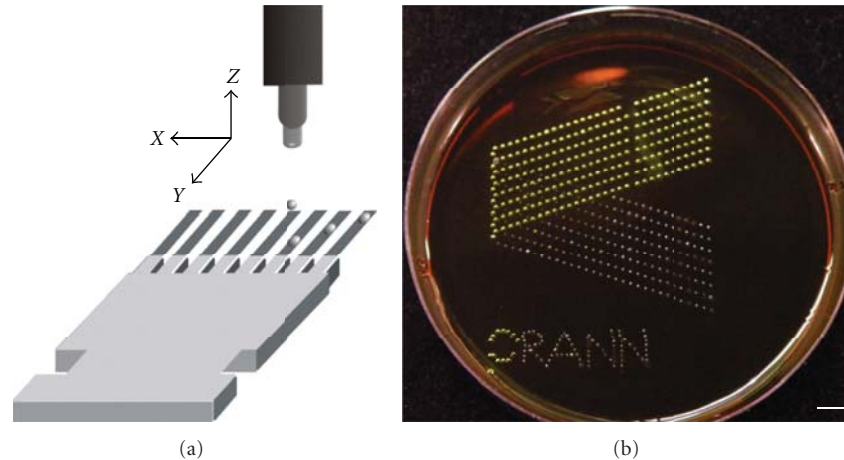
(a)   (b)

FIGURE 1: (a) Illustration of autodrop ink-jet spotting system for cantilever array functionalisation. Piezo-driven micropipette is mounted on a positioning system which has a positional accuracy of 1 μm in all directions. (b) Viable *E. coli* cells are able to be inoculated by spotting on an agar plate in a controlled manner. The developing colonies form the CRANN Logo after an incubation of 18 hours at 35°C. Scale bar 5 mm. The different optical appearance of the individual *E. coli* colonies spotted is a result of different rates of metabolism which lead to different colouring.

resonance frequency. Ramos et al. demonstrated [11] that the response of nanomechanical resonators depends on both the position and the stiffness of adsorbed biological material on the cantilever surface. This is important for the achievable sensitivity of the technique. Here we introduce the use of ink-jet printing for the functionalisation of cantilevers with industry-relevant microbial species for growth detection.

2. Materials and Methods

2.1. Chemicals, Cultures. Chemicals and culturing media were purchased from Sigma Aldrich (Arklow, Ireland) unless otherwise stated. The following microbial strains were obtained from Collection de l'Institut Pasteur (Paris, France): *Escherichia coli* CIP 53.126 (*E. coli*), *Pseudomonas aeruginosa* CIP 82.118 (*P. aeruginosa*), *Staphylococcus aureus* subsp. *aureus* CIP 4.83 (*S. aureus*), and *Candida albicans* CIP 48.72 (*C. albicans*). Bacterial and *C. albicans* strains were maintained on LB (0.5% NaCl, 0.5% yeast extract, 1% tryptone) or potato dextrose agar (PDA) slants, respectively, and stored at 4°C. Overnight cultures were prepared (200 rpm, 35°C, 15–18 h) from single colonies of each organism. The following day, 1 mL of the overnight cultures was transferred into 30 mL of LB or malt extract broth (ME) for bacterial or fungal cultures respectively, and cultured (200 rpm, 35°C) for 110 min in order to reach a logarithmic growth rate. One mL of each culture was precipitated by centrifugation (10 000 rpm, 5 min, Genofuge 16 M, Techne) and resuspended in 0.5 mL of the tested medium (LB, 10% LB, ME, 10% ME, or deionised water). Cell concentrations of the cultures were determined using cell counting chambers and optical microscopy.

2.2. Cantilever Preparation. Cantilever arrays were obtained from the IBM Zurich Research Laboratory (Zurich, Switzerland). Each array has 8 cantilevers with a length of 500 μm,

width of 100 μm, and thickness of 2–7 μm with a pitch of 250 μm. In preparation for microbial coating, the arrays were cleaned using O_2 plasma (0.3 mbar, 3 min, PICO Barrel Asher: Diener electronic GmbH and Co. KG, Ebhausen, Germany) and silanised for 45 min (1% (3-glycidyloxypropyl)-trimethoxysilane, 1% N-ethyldiisopropylamine in water-free toluene). The epoxy-silanised arrays were washed in water-free toluene (2 × 15 min) and dried in N_2 and subsequently coated with 1% (wt/vol) agarose-water solution (SeaKem Gold Agarose, Bioconcept; NH, USA) by using preheated (>100°C) glass microcapillaries (King Precision Glass Inc., Calif, USA). The pH of the melted agarose was adjusted to pH 11.9 by adding 2 M NaOH to the solution. The cantilevers were incubated in the agarose-filled capillaries for 5 seconds. Using this method a thin agarose layer is formed on the cantilever surface. The boundary of this gel layer is visible on the images of each cantilever.

2.3. Capillary Coating. As a control experiment, cantilevers were functionalised with microbes using glass microcapillaries. Agarose-coated cantilevers were immersed to full, half and 1/5 of their lengths for 6, 4, and 2 minutes, respectively, (Figure 2(a)). Capillary tubes were loaded with *E. coli* suspension (10% LB, 2.49 × 10^8 cells/mL).

2.4. Ink-Jet Spotting. The MD-P-801 autodrop dispensing system (Microdrop, Norderstedt, Germany) is comprised of a piezo-driven pipette (AD-K-501) and is mounted on a three axis micropositioning system which has an accuracy of 1 μm in all directions (Figure 1). The nozzle diameter used was 50 μm. The volume of liquid deposited is not only dependant on its viscosity but also on the voltage and the pulse length applied on the piezo actuator. In order to deposit one droplet per pulse, these parameter settings have to be adjusted for each individual suspension prior to

(a)   (b)   (c)
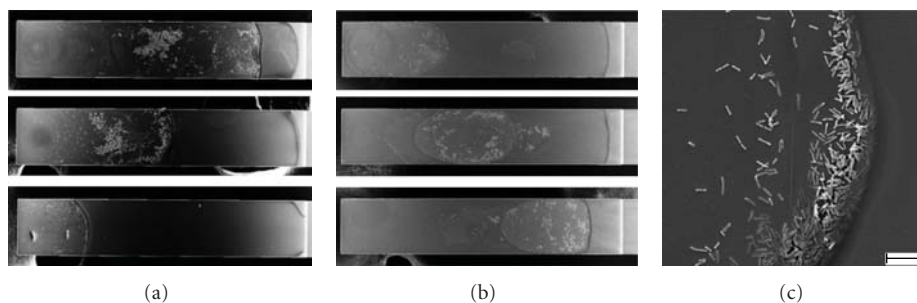
FIGURE 2: (a) SEM images of capillary-coated cantilevers for full (top), half (medium), and 1/5 (bottom) immersion in *E. coli* suspension. (b) Ten drops of *E. coli* suspension were deposited at different positions along the cantilevers' longitudinal axis. Cantilever arrays in images (a) and (b) were incubated for 24 h at optimal growth conditions before SEM imaging. The width of the cantilevers is 100 μm. The used suspension (2.49×10^8 cells/mL) was prepared in 10% LB. (c) SEM image showing accumulation of *E. coli* cells at the front end of capillary tube after functionalisation. Scale bar 10 μm.

(a)

(b)

(c)

(d)
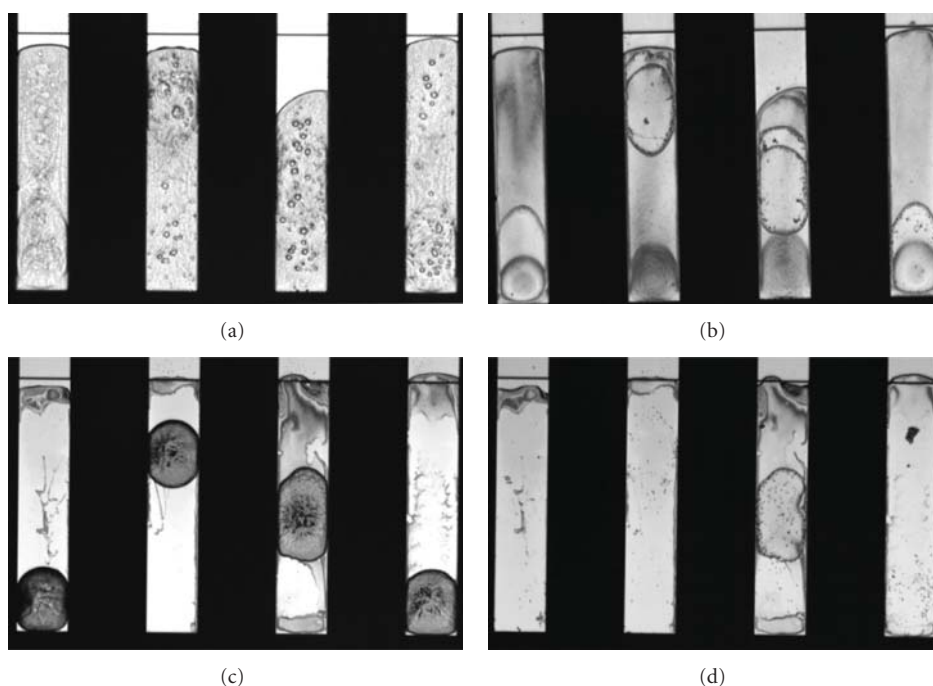
FIGURE 3: Optical microscope images of cantilevers with widths of 100 μm. Ten drops of *E. coli* suspension (2.49×10^8 cells/mL) were deposited at different positions on the cantilevers. (a) Cantilever array was incubated at growth conditions before image was taken. (b) Array was incubated at growth conditions then glutaraldehyde fixation (see Materials and Methods section) of the sample was carried out. (c) Array was dried at room conditions after deposition of cells (nongrowth control) (d) Array was prepared as a nongrowth control, then glutaraldehyde fixation was carried out.

deposition. The final spot diameter depends on the surface tension of the printed material and on the surface on which it is deposited. By using a low pulse frequency in our experiments we allowed each droplet to soak into the agarose surface before the next droplet landed on the surface. With this method, aerosol formation could be prevented, and; therefore, no cross-contamination between the cantilevers is expected. The micropipette was cleaned 3 times with 70% ethanol solution and twice with 96% ethanol solution before use. These cleaning steps were sufficient to avoid nozzle clogging or cross-contamination. Cell suspensions prepared as mentioned previously were loaded into 96-well microtiter plates (Sterilin Ltd., Norwick, UK). Prior to filling the micropipette, solutions in the microtiter plate reservoirs were mixed in order to provide an even cell concentration in the nozzle. Droplets of the different suspensions were spotted on each cantilever independently. To avoid cross-contamination of the lever surfaces the nozzle was cleaned with ethanol between each tested suspension.

2.5. Scanning Electron Microscopy (SEM) Sample Preparation. The cell-functionalised cantilever arrays were exposed to relatively dry room conditions (20–40% RH) for less than 30 minutes. For growth testing, they were placed in high

TABLE 1: Calculation of drop volume after deposition of 180 droplets of microbe suspensions.

Cells/mL	Total cell number/180 drops	Drop volume (L)	Average cell number/drop
6.3×10^6	226	1.99×10^{-10}	1.25
1.175×10^6	45	2.13×10^{-10}	0.25
$\sim 6.3 \times 10^5$	18	1.59×10^{-10}	0.1

humidity (>95% RH) at 35°C. For nongrowth controls, they were left to dry completely at room conditions. High humidity during growth testing was provided by a small water reservoir placed closed to the arrays in a closed Petri dish.

Prior to SEM imaging, cantilever arrays were dried at 24°C and 35% RH for at least 24 hrs. Cantilever arrays were immersed in 5% glutaraldehyde solution (0.05 M phosphate buffer, pH 7) and incubated at room conditions with gentle shaking for 3-4 h. After fixation, excess glutaraldehyde was removed by washing in phosphate buffer (0.05 M, pH 7) for 10 min. This step was repeated 6 times. Samples were subsequently dehydrated using 10-30-50-70-90-100-100% ethanol solution (10 minutes for each step). After drying, 10 nm Pd was deposited on the samples (Cressington Sputter Coater 208 HR Watford, United Kingdom). SEM images (SEM-ULTRA, Carl Zeiss, Germany) were taken at 5 kV, with an aperture size of 30,000 μm using the lens detector.

3. Results and Discussion

Microcantilever arrays were previously used to detect the viable growth of *E. coli* [10, 12] and *Aspergillus niger* (*A. niger*) [9, 13]. In these studies individual glass microcapillaries were used to seed cells on individual agarose-functionalised cantilevers. The deposition of *A. niger* spores was performed by functionalising the cantilever surface with a uniform distribution of *Aspergillus*-specific antibodies. The seeded microbial species were mixed with a culture medium which provided essential nutrition for microbial growth. After immersion of the levers in the suspension, nutrition is stored in the porous agarose layer. During growth microbes assimilate nutrition and water from the nutritive layer and humid air. In order to compare the coating efficiency of ink-jet printing to that of the previously used capillary coating method, two cantilever arrays were prepared for growth testing (Figure 2). Agarose-coated cantilevers were immersed to full, half, and 1/5 of their lengths in glass capillaries filled with *E. coli* suspension for 6, 4, and 2 minutes, respectively, (Figure 2(a)). On a second agarose-coated array the same *E. coli* suspension was deposited by spotting at different points along the cantilever. At each position, 10 drops of cell suspension were dispensed with high accuracy (Figure 2(b)). SEM images of *E. coli* colonies were taken after 24 h growth. As a control, a second set of arrays were prepared as described above; however, they were not incubated at optimal growth conditions (non growth controls). Capillary coating with these relatively large

(a)

(b)

(c)

(d)
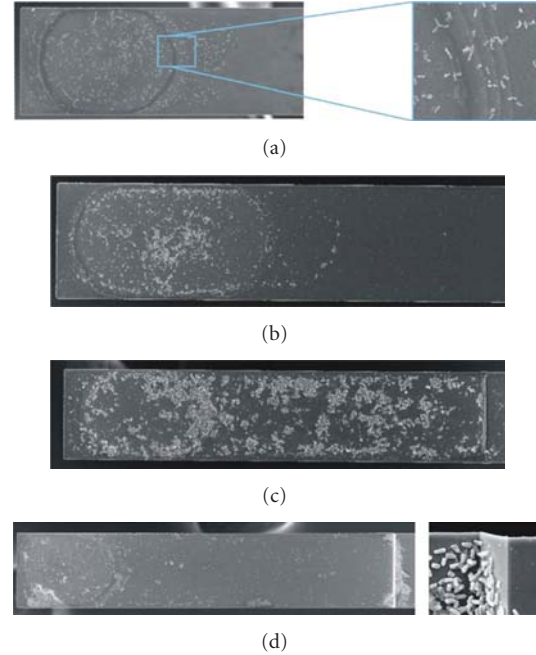
FIGURE 4: SEM images of cantilevers demonstrating accuracy of drop positioning and cell distribution after 24 h incubation at growth conditions. The width of cantilevers is 100 μm in each case. Ten drops of cell suspension were deposited at the front end of the cantilevers. (a) Imprints of series of droplets on agarose-coated cantilever, after growth of *P. aeruginosa*. (b) Ten perfectly spotted drops of *S. aureus* (2.92×10^8 cells/mL, 10% LB) cells on an agarose-coated cantilever. One spot was deliberately deposited off-position. (c) *S. aureus* (3.28×10^8 cells/mL, LB) growth on cantilever surface. (d) *P. aeruginosa* (1.84×10^8 cells/mL, 10% LB) growth on cantilever surface. Cells are growing over the clamping point of the cantilever.

structures (2 μm) results in the accumulation of cells at the capillary open end. This can be explained by the flow of cells with the liquid and evaporation at the front of the tube (Figure 2(c)). Compared to capillary functionalisation, the localised deposition of cells can be easily controlled by ink-jet printing. The sharp edge of the drop boundary visible on the SEM image (Figure 2(b)) shows that the positional accuracy of the delivered droplet is highly reproducible. Deposition of 180 droplets with 3 different dilutions of microbe suspension shows that the average droplet size and the average cell number per droplet correlate with the dilution of the samples (Table 1). There was no increase in the cell number per drop which indicates that cells are not sedimenting in the nozzle during deposition. The optimal cell number to avoid nozzle clogging in the case of bacteria is under 5-6 $\times 10^8$ cfu and under 1.2–1.4 $\times 10^6$ cfu in the case of *C. albicans*. It is important to mention that before glutaraldehyde fixation of samples, salt and medium residues covered the cantilevers indicating good diffusion of the nutrition along the full length of the lever. The washing and dehydration steps after glutaraldehyde fixation were sufficient to remove these residues without the removal of the deposited cells (Figure 3). We postulate that the thin liquid layer present at >90% relative humidity may act to keep the nutrition

(a)

(b)

(c)

(d)
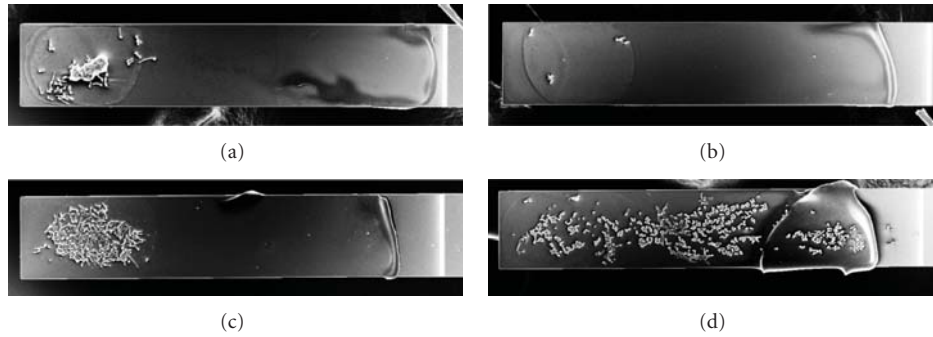
FIGURE 5: SEM images of cantilevers showing *C. albicans* propagation on the surface after 24 h incubation at growth conditions. The width of cantilevers is $100\,\mu$m in each case. Ten drops of cell suspensions were deposited at the front end of the cantilevers. (a, c) *C. albicans* (1.36×10^6 cells/mL, 10% ME) before growth (a) after growth (c). (b, d): *C. albicans* (10^6 cells/mL, ME) before growth (b) after growth (d).

Candida albicans

Nongrowth control   Growth test

(a)

Escherichia coli

Nongrowth control   Growth test

(b)

Pseudomonas aeruginosa

Nongrowth control   Growth test

(c)

Staphylococcus aureus

Nongrowth control   Growth test

(d)
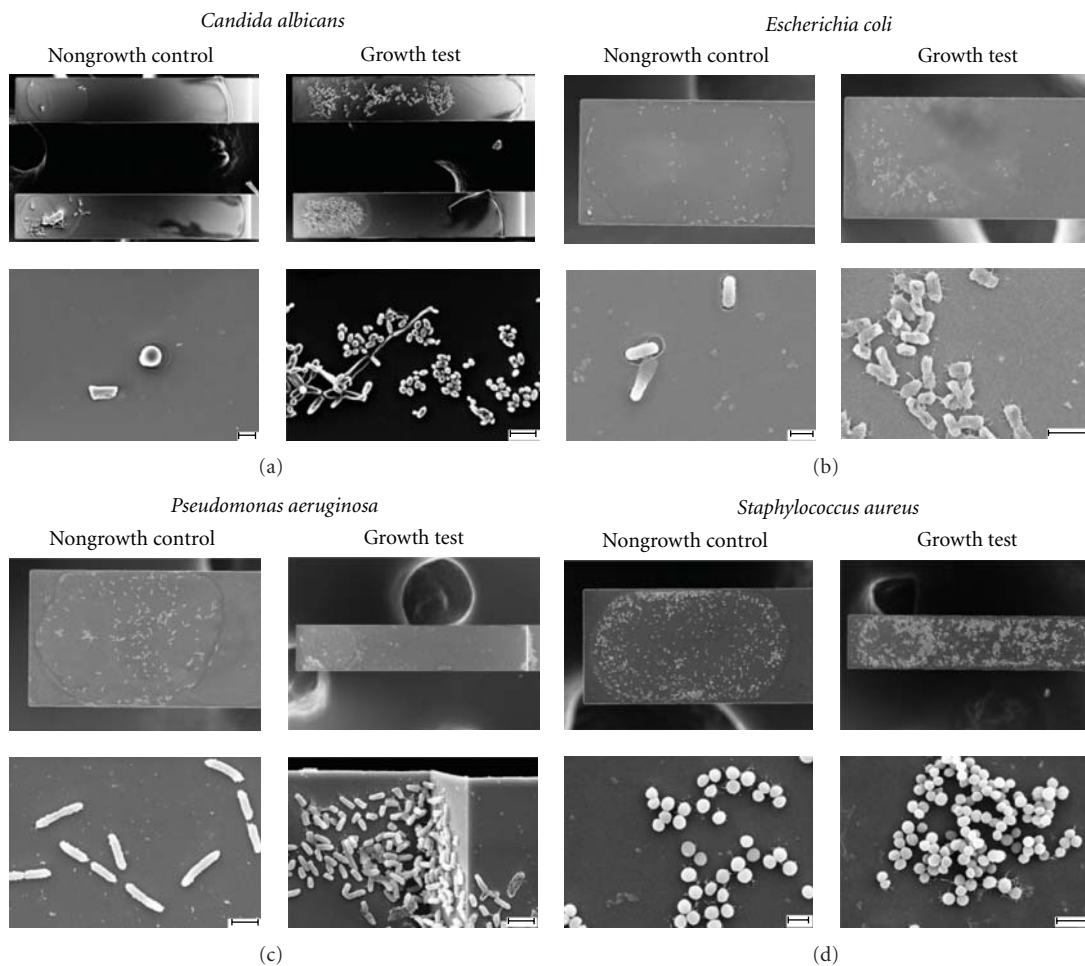
FIGURE 6: SEM images of growing microbe cultures on agarose-coated cantilevers. The width of cantilevers is $100\,\mu$m. In each section, the pictures on the left show the surface of the cantilevers dried at room conditions after ink-jet spotting. The pictures on the right show cantilevers after 24 h incubation at growth conditions. Ten droplets were deposited on the front end of each cantilever. (a) *C. albicans* suspensions deposited on the front end of two cantilevers (top: 1.36×10^6 cells/mL, 10% ME, bottom: 10^6 cells/mL, ME). Scale bars $10\,\mu$m. *C. albicans* grow pseudohypha on the surface (bottom right) (b) *E. coli* suspension (3.96×10^8 cells/mL, 10% LB). Scale bars: bottom left $1\,\mu$m, bottom right $2\,\mu$m. (c) *P. aeruginosa* (1.84×10^8 cells/mL, 10% LB). Scale bars $2\,\mu$m; (d) *S. aureus* suspension (2.92×10^8 cells/mL, 10% LB). Scale bars: bottom left $1\,\mu$m, bottom right $2\,\mu$m.

(a)

(b)
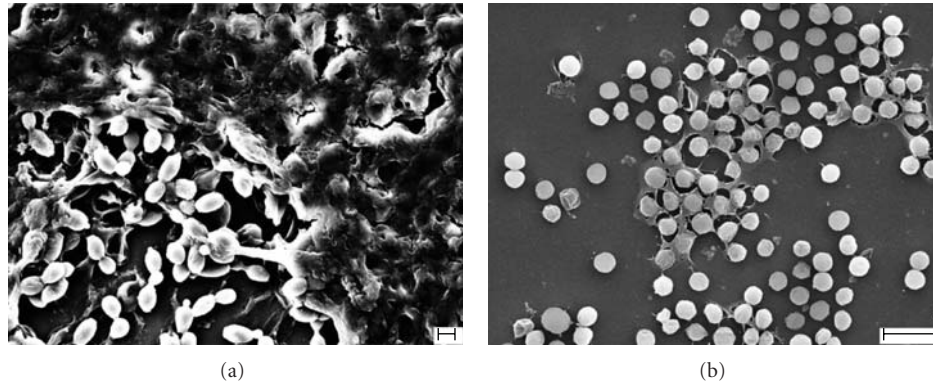
FIGURE 7: SEM images of biofilm-like structures of *C. albicans* (a) and *S. aureus* (b) on a cantilever surface. *C. albicans* cells were deposited in 10% ME medium (10^6 cells/mL) and incubated at growth conditions for 24 h. *S. aureus* cells were deposited in 10% LB medium (2.92×10^8 cells/mL) and incubated at growth conditions for 24 h.

in solution on the cantilever surface which aids in this distribution. Therefore, in an actual growth measurement, at high humidity, no salt-carbohydrate-protein crystal layer is formed which would have an effect on the mechanical properties of these sensors and the growth characteristics of the seeded microorganisms. This provides an opportunity for initial cells to spread along the surface even if nutrition is originally available only at the spotting site at the beginning of the experiment. A similar distribution of nutrition is not seen on the non-growth control cantilever which was not incubated at elevated humidity levels. In some experiments Figures 4(c) and 4(d), cells were observed outside the spotting area after growth of the culture which cannot be explained by an off-position droplet deposited during ink-jet printing (Figure 4(b)). Concentric imprints caused by individual droplets on the agarose layer are often visible on SEM images showing an accurate centre position of the droplets (Figure 4(a)). The tested *C. albicans* (Figure 5) or *S. aureus* (Figure 4(c)) cannot actively move away from their original position while *E. coli* or *P. aeruginosa* (Figure 4(d)) are motile bacteria enabling cell propagation especially if a thin liquid layer is available. This propagation is more likely if 100% culturing medium is used for microbe deposition instead of with diluted medium (10% LB or 10% ME). Dilution of the growth medium decreased the growth rate of microbes. In the case of *C. albicans*, the use of less cells per droplet (5–10 cells/droplet) in full medium still resulted in the complete coverage of the cantilever surface with cells (Figure 5(d)) when compared to the non-growth control (Figure 5(b)). Spotting 50–100 cells in diluted medium (Figures 5(a), 5(c)) did not allow the organism to grow out of their initial spotted position. In several experiments, four microbial strains were tested in terms of viability after ink-jet printing and grown on the surfaces of microcantilevers. Each array was prepared twice, and one of each was used as a non-growth control. SEM images of these experiments show the viability and multiplication of the tested organisms (Figure 6). In each case, elevated cell numbers can be observed on the arrays exposed to growth conditions (high

humidity and elevated temperature). *Candida albicans* is a yeast form microfungi with typical cell dimensions of 4-5 μm in diameter. At certain conditions, mostly related to limited nutrition, they are able to grow pseudohypha where the cells have not separated after cell division. This morphological switch is often studied as it has a major role in *C. albicans* pathogenicity [14]. In our tests, *C. albicans* cells were seeded in the budding-yeast form in 100% ME suspension and also 10% ME suspension. Figure 6(a) shows that in the suspension with full medium some cells are developing filamentous structures (pseudohyphae) but also budding-yeast form can also be observed. It is likely that in this special microenvironment the pseudohyphae play a part in the spread of *Candida* along the cantilevers. All these processes resulting in the colonisation of the surface might cause changes in the cantilevers mechanical properties, and; hence, influence growth detection measurements which are originally based on the detection of a mass increase on the cantilever surface. For some biosensing techniques, high salt or sugar content of microbial culturing medium can disturb the measurement although decreasing the available nutrients in the environment can cause changes in growth rate or morphology of the cells. In other experiments *C. albicans* (Figure 7(a)) and *S. aureus* (Figure 7(b)) cells were deposited on agarose-coated cantilevers with diluted medium. We found that decreasing nutrition in the used suspension results in a decrease in viability and also altered the morphology of the cells. Cells started to accumulate extracellular biomaterial which resembled biofilm formation (Figure 7). Bacteria and *Candida* colonies usually form biofilms on various surfaces including silicon in order to help the bacterial population to survive in certain environments. However, further investigation has to be done to understand this process in the case of microcantilevers. It is expected that biofilm formation will influence the spring constant (k) of a cantilever. It is also important to mention that the use of deionised water for cell deposition resulted in the centering of bacterial cells with respect to droplet positions, while the use of more viscous suspensions, such as culture medium, resulted in the accumulation of cells around

the rim of the liquid droplet, thus, allowing for high accuracy when positioning microorganisms within a droplet (data not shown).

4. Conclusion

It was successfully proved in our experiments that different types of microbial cells are able to be deposited on microcantilever surfaces while retaining their viability. Ink-jet spotting was used for cantilever functionalisation with viable cells, thus, revealing its potential as a superior alternative for sensor applications and real-time growth measurements. There is no need for specific antibodies facilitating tight binding during deposition of cells. In the case of motile microorganisms the fluid film allows cells to be freely distributed, and, in these cases the introduction of antibodies could keep the species in place. Compared to the previously reported capillary-coating technique ink-jet printing has been shown to be a more accurate way to position cells, and hence, to optimise the detection of mass changes during microcantilever-based growth detection.

Acknowledgments

References

[1] K. W. Binder, A. J. Allen, J. J. Yoo, and A. Atala, "Drop-on-demand inkjet bioprinting: a primer," *Gene Therapy and Regulation*, vol. 6, no. 1, pp. 33–49, 2011.

[2] T. Braun, N. Backmann, A. Bietsch et al., "Conformational change of bacteriorhodopsin quantitatively monitored by microcantilever sensors," *Biophysical Journal*, vol. 90, no. 8, pp. 2970–2977, 2006.

[3] T. Braun, M. K. Ghatkesar, N. Backmann et al., "Quantitative time-resolved measurement of membrane protein-ligand interactions using microcantilever array sensors," *Nature Nanotechnology*, vol. 4, no. 3, pp. 179–185, 2009.

[4] T. Okamoto, T. Suzuki, and N. Yamamoto, "Microarray fabrication with covalent attachment of DNA using Bubble Jet technology," *Nature Biotechnology*, vol. 18, no. 4, pp. 438–441, 2000.

[5] A. Roda, M. Guardigli, C. Russo, P. Pasini, and M. Baraldini, "Protein microdeposition using a conventional ink-jet printer," *BioTechniques*, vol. 28, no. 3, pp. 492–496, 2000.

[6] A. Bietsch, J. Zhang, M. Hegner, H. P. Lang, and C. Gerber, "Rapid functionalization of cantilever array sensors by inkjet printing," *Nanotechnology*, vol. 15, no. 8, pp. 873–880, 2004.

[7] T. Xu, S. Petridou, E. H. Lee et al., "Construction of high-density bacterial colony arrays and patterns by the ink-jet method," *Biotechnology and Bioengineering*, vol. 85, no. 1, pp. 29–33, 2003.

[8] T. Xu, J. Jin, C. Gregory, J. J. Hickman, and T. Boland, "Inkjet printing of viable mammalian cells," *Biomaterials*, vol. 26, no. 1, pp. 93–99, 2005.

[9] N. Nugaeva, K. Y. Gfeller, N. Backmann et al., "An antibody-sensitized microfabricated cantilever for the growth detection of *Aspergillus niger* spores," *Microscopy and Microanalysis*, vol. 13, no. 1, pp. 13–17, 2007.

[10] K. Y. Gfeller, N. Nugaeva, and M. Hegner, "Rapid biosensor for detection of antibiotic-selective growth of *Escherichia coli*," *Applied and Environmental Microbiology*, vol. 71, no. 5, pp. 2626–2631, 2005.

[11] D. Ramos, J. Tamayo, J. Mertens, M. Calleja, and A. Zaballos, "Origin of the response of nanomechanical resonators to bacteria adsorption," *Journal of Applied Physics*, vol. 100, no. 10, Article ID 106105, 2006.

[12] K. Y. Gfeller, N. Nugaeva, and M. Hegner, "Micromechanical oscillators as rapid biosensor for the detection of active growth of *Escherichia coli*," *Biosensors and Bioelectronics*, vol. 21, no. 3, pp. 528–533, 2005.

[13] N. Nugaeva, K. Y. Gfeller, N. Backmann, H. P. Lang, M. Düggelin, and M. Hegner, "Nanomechanical cantilever array sensors for selective fungal immobilization and real-time growth detection," *Biosensors and Bioelectronics*, vol. 21, pp. 849–856, 2005.

[14] I. A. Cleary, P. Mulabagal, S. M. Reinhard et al., "Pseudohyphal regulation by the transcription factor Rfg1p in Candida albicans," *Eukaryotic Cell*, vol. 9, no. 9, pp. 1363–1373, 2010.

Research Article

The Microcantilever: A Versatile Tool for Measuring the Rheological Properties of Complex Fluids

I. Dufour,[1] A. Maali,[2] Y. Amarouchene,[2] C. Ayela,[1] B. Caillard,[1] A. Darwiche,[2] M. Guirardel,[3] H. Kellay,[2] E. Lemaire,[1] F. Mathieu,[4] C. Pellet,[1] D. Saya,[4] M. Youssry,[3] L. Nicu,[4] and A. Colin[3]

[1] *Université de Bordeaux, IMS, 33 400 Talence, France*
[2] *Université de Bordeaux, LOMA, 33 400 Talence, France*
[3] *Rhodia Laboratoire de Futur, Unité mixte Rhodia-CNRS, Université de Bordeaux, 33608 Pessac, France*
[4] *Université de Toulouse, LAAS CNRS, 31077 Toulouse, France*

Correspondence should be addressed to I. Dufour, isabelle.dufour@ims-bordeaux.fr

Silicon microcantilevers can be used to measure the rheological properties of complex fluids. In this paper, two different methods will be presented. In the first method, the microcantilever is used to measure the hydrodynamic force exerted by a confined fluid on a sphere that is attached to the microcantilever. In the second method, the measurement of the microcantilever's dynamic spectrum is used to extract the hydrodynamic force exerted by the surrounding fluid on the microcantilever. The originality of the proposed methods lies in the fact that not only may the viscosity of the fluid be measured, but also the fluid's viscoelasticity, that is, both viscous and elastic properties, which are key parameters in the case of complex fluids. In both methods, the use of analytical equations permits the fluid's complex shear modulus to be extracted and expressed as a function of shear stress and/or frequency.

1. Introduction

Paints, shampoos, gels, and foams are examples of complex fluids we encounter every day. A mesoscopic scale comprised between the molecular scale and the scale of the sample characterized these materials. In the case of foams, it is the size of the gas bubbles. These materials exhibit complex behavior under shear stress, showing both solid and liquid characteristics.

To fully characterize the mechanical behavior of complex fluids, let us consider a small cube of material of section S, and let us apply a tangential force F on its top surface. This material is submitted to a shear stress $\tau = F/S$. Under the action of the force F, the cube changes its shape. The deformation, which is the ratio of the modified size of the cube minus its initial size divided by its initial size, has two components: an elastic component and a viscous one. In general, the elastic nature of a material is associated with the characteristic equilibrium microstructure in the material. For example, polymeric liquids have a microstructure that is like an assembly of springs representing the linear

chains. When this microstructure is disturbed (deformed), thermodynamic forces tend to restore the equilibrium. The energy associated with this restoration process is the elastic energy. Restoration of these springs to their equilibrium state occurs via the release of the elastic energy that was stored during the deformation process. But polymeric fluids are not ideal elastic materials, because they also exhibit viscous dissipation (energy loss) during deformation. When the force is removed, the deformed material undergoes a partial recovery of shape as the elastic energy is recovered; however, the deformation due to the viscous part is permanent. In steady flow, the deformation due to the viscous component increases continuously. Sinusoidal time-varying forces are thus required to probe both components. To this end, the rheological properties of the material are characterized either by a complex viscosity η^* or a complex shear modulus G^* defined by

$$
\eta^* = \frac{\tau}{\dot{\gamma}} = \eta' - j\eta'',
$$
$$
G^* = \frac{\tau}{\gamma} = G' + jG'' = j\omega\eta^* = j\omega(\eta' - j\eta''),
$$

$$(1)$$

with τ being the shear stress, γ the shear strain, and $\dot{\gamma}$ the shear rate. Properties η', η'', G', and G'' are, respectively, the real and imaginary parts of the viscosity, the elastic shear modulus (real part of G^*), and the viscous shear modulus (imaginary part of G^*). The "standard" unit of viscosity is Pa.s, but usually, the centiPoise (cP) is used, which corresponds to 0.001 Pa.s (the viscosity of water). The unit of the shear modulus is Pa.

This complex notation reveals the possible phase shift between shear stress and shear strain or shear rate. A perfect liquid has a zero elastic modulus G', whereas a perfect solid has a zero viscous modulus G''.

The value of the complex viscosity depends on the amplitude of the oscillation. For small deformations, the response of the system is linear, meaning that the response is additive: the effect of the sum of two small deformations is equal to the sum of the two individual responses. Linear viscoelastic properties are associated with near equilibrium measurements of the fluid. This means that the configurations of the fluids are not removed far away from their equilibrium structures. In this regime, the deformation is proportional to the shear stress, and the shear modulus does not depend upon the amplitude of the applied force. At the opposite end of the spectrum, large applied forces may modify the structure of the sample. In this case, the values of G^* depend not only on the frequency of the oscillation, but also upon the amplitude of the applied force. If the excitation frequency is greater than the inverse of the characteristic time of the material, then its structure is frozen, and the material behaves as a solid. Otherwise, if the applied frequency is lower than the inverse of the characteristic time, the structure of the fluid relaxes under shear stress and the material behaves as a liquid.

The classical way to measure the rheological properties of fluids is either to use a viscometer (involving a falling or rollingball) or a rheometer (utilizing the rotational motion of a cone/plate or Couette flow) [1]. Whereas viscometers can only characterize the viscous component of the deformation, rheometers can characterize both elastic and viscous responses. However, the latter have also several drawbacks: the measurement cannot be made in situ (a fluid sample is needed), the amount of fluid necessary to make the measurement is quite large (a few milliliters), and the measurement is limited to low frequency (less than 200 Hz due to inertial issues).

To overcome the frequency range limitation, some alternative methods have been developed over the two last decades, giving raise to the field of "microrheology," which involves the measurement of the movement of monodispersed beads (microspheres) immersed in the fluid [2–8]. The motion of the beads can be active (optical or magnetic tweezers) or passive (thermal noise) and the acquisition of the motion is performed optically (video particle tracking, laser particle tracking, quasielastic light scattering, and diffusing wave spectroscopy). The major advantage of such methods is the wide frequency range spanned (from 10^{-2} Hz to 100 kHz). Unfortunately, as explained in [8], these methods are computationally intensive. In 2007, a particle tracking experiment would require up to 10 minutes of video recording and the analysis of the data would take about 10 hours on a dedicated PC [8]. Even though this limitation becomes less restrictive each year due to increasing computational power, these methods still necessitate time-consuming procedures. Moreover, for highly viscous fluids, it is challenging to observe the very small motions of the probe particle. Another limitation comes from the fact that if the particle size is less than the mesoscopic scale of the fluid (polymer chains, mesh size, etc.), the measurement yields a local measurement that can be nonrepresentative for the real properties of the bulk fluid.

In order to cover higher frequencies (from 1 MHz to a few 100s of MHz), acoustic shear-polarized devices, such as QCM or Love wave devices, have been used [9–14]. These high-frequency devices are very compact, but they also show adverse properties: (i) the penetration depth of the shear wave in the liquid is very low so that only a very thin film viscoelasticity is measured; (ii) the displacement amplitudes are small so that nonlinear effects requiring a certain minimum stimulation in terms of spatial displacements may not become activated and thus are not being sensed. The first item also leads to issues when samples having microstructures extending beyond the penetration depth are investigated, such as may be the case for suspensions and emulsions [15].

In the current paper, we present two alternative methods based on the use of silicon microcantilevers. Both methods are based on the measurement of the hydrodynamic force exerted on a solid body moving in a fluid, which depends on the fluid's rheological properties. In the first method, the moving solid body is a sphere attached to the microcantilever and the force measurement is made using the microcantilever, similar to what is done in AFM systems. In the second method the microcantilever has a dual role: it is used to actuate the fluid flow as well as to measure the hydrodynamic force. Thus, both methods are based on the ability to relate the free-end cantilever deflection to the fluid's rheological properties through analytical equations. Both principles have already been used by the authors [16–20] or other teams [21–33] to measure the viscosity of Newtonian fluids (fluids with constant real part of viscosity and no imaginary part of viscosity). The originality of the presented work comes from the fact that thanks to analytical modeling these methods have been extended to the measurement of the complex viscosity or of the complex shear modulus which characterize both the elastic and viscous behavior of complex fluids.

2. Method 1: Measurement of the Hydrodynamic Force on a Confined Sphere Using AFM

2.1. Principle. For this method a glass sphere is glued at the free-end of a silicon microcantilever. In order to have a high hydrodynamic force due to confinement of the fluid (as in a classical rheometer), the sphere is placed near a substrate surface (like the tip of an AFM cantilever) and immersed in the fluid during testing. This setup provides two modes of measurement.
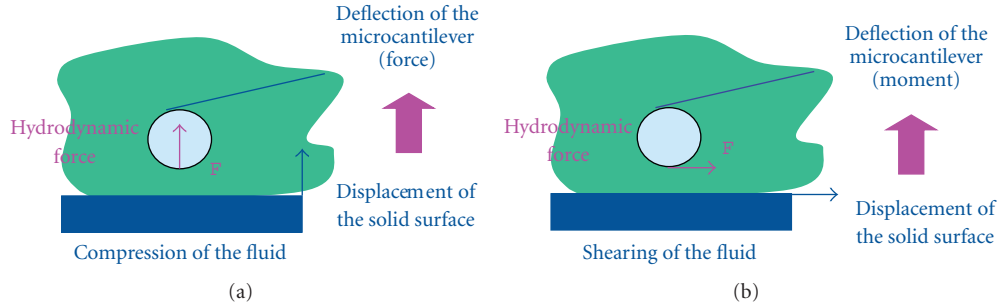
FIGURE 1: Principle of the first method. (a) Vertical displacement of the substrate surface and compression of the fluid. (b) Horizontal displacement of the substrate surface and shearing of the fluid.
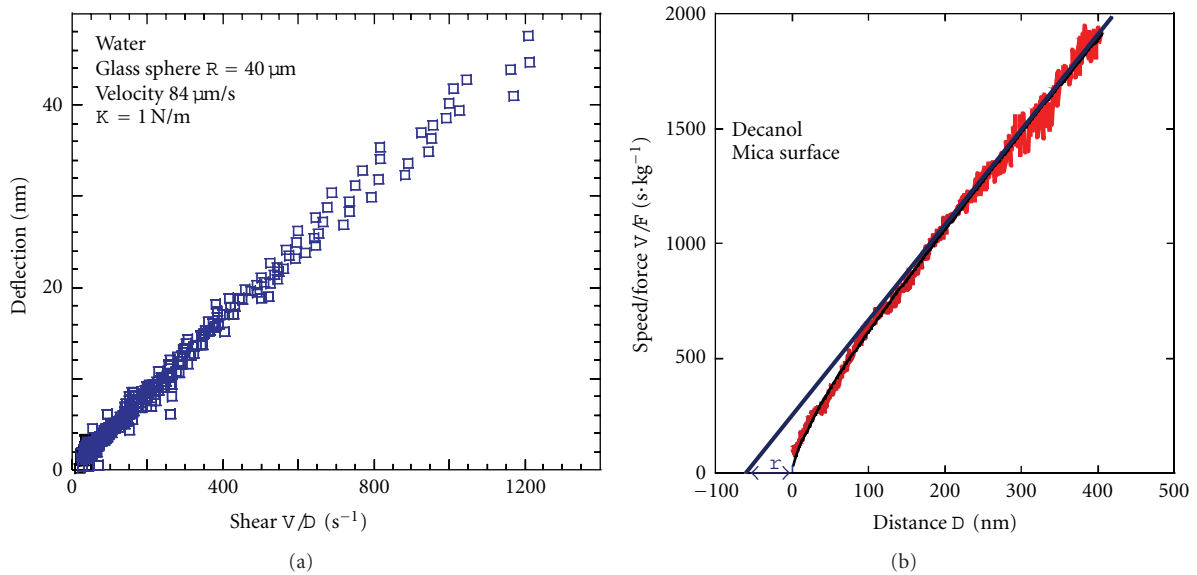

FIGURE 2: Examples of measurement with Method 1 in configuration of fluid compression. (a) Case of Newtonian fluid, water, without slip (blue squares: measurements). (b) Case of Newtonian fluid, decanol, with slip (red curve: measurements, blue line: fit of the measurement by a line for high distance measurements).

(i) The plane surface is approached towards the sphere (vertical velocity of the plane surface) and the compression of the fluid exerts a hydrodynamic force on the sphere which can be estimated by the measurement of the microcantilever deflection [25, 26] (Figure 1(a)).

(ii) The horizontal displacement of the substrate surface shears the fluid (Figure 1(b)). It induces a horizontal hydrodynamic force at the bottom of the sphere [27] which exerts a moment at the free end of the cantilever which results in the cantilever deflection.

In both cases, modeling the fluid-structure interaction allows for the extraction of both the real and imaginary parts of the fluid's viscosity.

To measure hydrodynamic forces, we have used the dimension Veeco AFM in the contact mode. The hydrodynamic force is related to the deflection of the cantilever, which is measured and stored using a 32-bit data acquisition card. Spherical borosilicate particles (GL0186B/106-125, MO-Sci corporation) of $110\,\mu$m diameter were glued to the

free end of a silicon nitride rectangular cantilever ORC8 (Veeco) using epoxy (Araldite, Bostik, Coubert). The vertical displacement of the substrate was induced by a piezoelectric ceramic (Nano-T225, Mad City Labs Inc., Madison, USA).

2.2. Compression Mode. In the case of the compression of the fluid (Figure 1(a)) the hydrodynamic force F can be expressed in the lubrication approximation ($D \ll R$) by [20, 28–33]

$$F = \frac{6\pi\eta R^2}{D} V f^*(D), \qquad (2)$$

with R denoting the sphere radius, D the distance between the substrate surface and the bottom of the sphere, V the vertical velocity of the substrate surface, and $f^*(D)$ a function that takes into account the slip of the fluid at the surfaces. For the nonslip boundary condition, $f^*(D) = 1$, so that (2) shows that the microcantilever deflection, as a function of the shear rate, V/D, is a line that passes through the origin. The slope of this line depends on the viscosity of the fluid. An example of a measurement is presented in Figure 2(a).
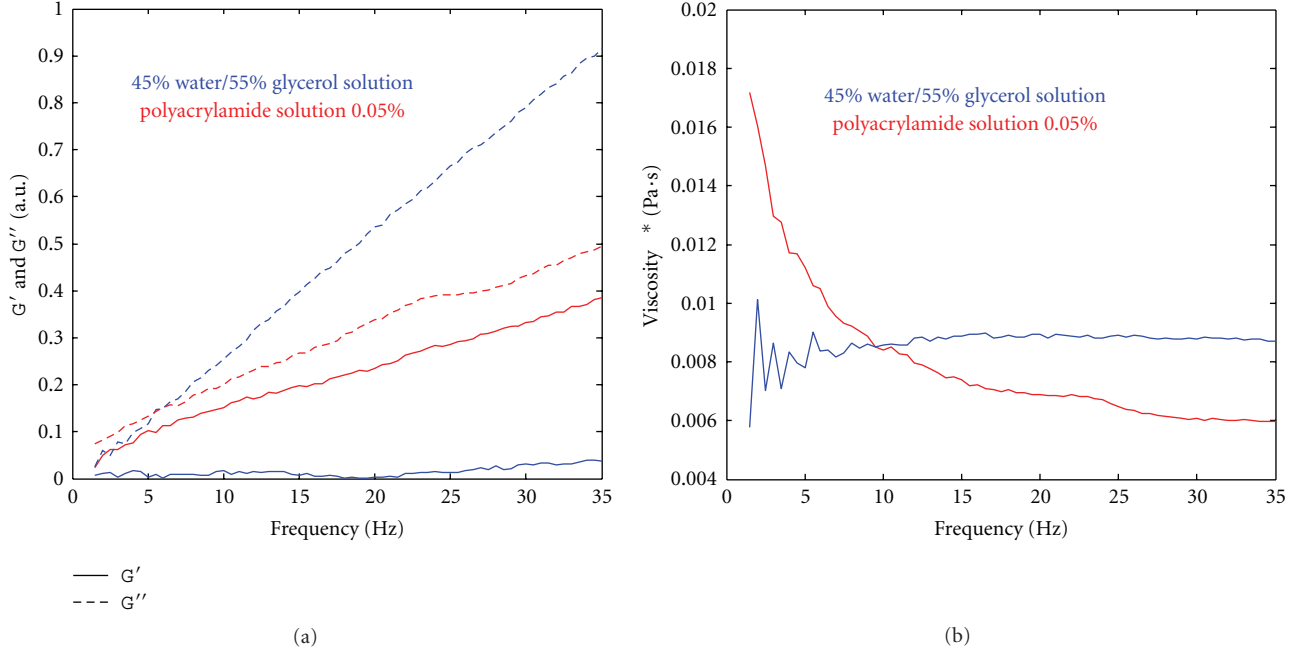
(a)

(b)

FIGURE 3: Example of measurements with Method 1 in shear mode on glycerol/water solution (45wt%/65wt%, blue curves) and poly-acrylamide solution in water (0.05wt%/99.95wt%, red curves). The distance D is $2\,\mu$m. Shown are the dependencies on frequency for (a) elastic G' and viscous G'' shear moduli and (b) modulus of the dynamic viscosity $|\eta^*|$.

If slip exists at the solid surfaces (substrate and/or sphere), (2) can be simplified for the case where the slip length r is very small compared to the distance D ($r \ll D$)

$$\frac{V}{F} \approx \frac{D+r}{6\pi\eta R^2},\qquad(3)$$

where r is the sum of the slip-length of the fluid on the two solid surfaces. An example of a measurement utilizing (3) is shown in Figure 2(b): the slip length r corresponds to the distance where the V/F ratio intercepts the abscissa axis.

2.3. Shear Mode. The shear mode (Figure 1(b)) can be achieved by using a piezoelectric ceramic Nano-T225, Mad City Labs Inc., Madison, USA which causes horizontal oscillation of the substrate surface of the form $Y_{\text{piezo}} = Y_0 \cos(\omega t)$. In this case, both the amplitude Z_0 and the phase Φ_z of the free-end microcantilever deflection are measured using a lock-in-amplifier (model DSP 7280, AMETEK Inc. Oak Ridge, TN). The free-end deflection is then of the form $Z_0 \cos(\omega t + \Phi_z)$. Then, the complex viscosity or complex shear modulus can be expressed by

$$\eta^* = \eta' - j\eta'' \begin{cases} \eta' = \dfrac{G''}{\omega} = \dfrac{Z_0 \sin \Phi_z L_{\text{eff}}}{18\pi R^2 Y_0 \omega \Gamma(D/R)}, \\[2mm] \eta'' = \dfrac{G'}{\omega} = \dfrac{Z_0 \cos \Phi_z L_{\text{eff}}}{18\pi R^2 Y_0 \omega \Gamma(D/R)}, \end{cases} \qquad(4)$$

where L_{eff} is the effective length of the cantilever, R the radius of the sphere, Z_0 the amplitude of the transverse deflection of the microcantilever, Y_0 the amplitude of the

horizontal oscillation of the piezoelectric ceramic, Φ_z the phase between microcantilever deflection and piezoelectric oscillation, ω the radial frequency of the oscillation, and $\Gamma(D/R)$ a hydrodynamic function calculated by Brenner [27] for the case $D \ll R$

$$\Gamma\left(\frac{D}{R}\right) \approx \frac{8}{15} \ln\left(\frac{D}{R}\right) - 0.9588.\qquad(5)$$

Examples of measurements made with a Newtonian fluid (solution of 45 wt% water/55 wt% glycerol) and with a viscoelastic fluid (0.5 wt% polyacrylamide solution) on mica substrate are presented in Figure 3.

These measurements confirm the fact that for the considered frequency range (1 Hz–35 Hz) and shear rate, the glycerol solution is Newtonian whereas the polyacrylamide solution is viscoelastic.

3. Method 2: Measurement of the Hydrodynamic Force on a Microcantilever Using Deflection Spectrum

The idea of using the deflection spectrum of a microcantilever immersed in a fluid in order to extract properties of the fluids has been proposed by different authors [21–24]. The method is based on the measurement of both the resonant frequency and the quality factor which depend on both the mass density and the viscosity. Depending on the case, the fluid mass density and viscosity are determined either after calibration or by using semianalytical methods. The major drawbacks of such approaches stem from the fact that when using only *one* microcantilever the viscosity

is determined at only *one* frequency, and the elasticity of the fluid is neither taken into account nor estimated. Moreover, a resonant phenomenon is needed in order to measure the resonant frequency and the associated quality factor. Therefore, these approaches cannot be used for highly viscous fluids for which a resonant peak may not exist.

3.1. Basic Principle and Equations for Method 2. When a vibrating cantilever is immersed in a fluid, the fluid exerts a hydrodynamic force on the cantilever due to both the pressure force on the surfaces perpendicular to the cantilever displacement and the shear force on the surfaces parallel to the cantilever displacement. The total hydrodynamic force is composed of two terms: one inertial term proportional to microcantilever acceleration and one viscous term proportional to microcantilever velocity. The microcantilever deflection in the Fourier-space is governed by the Euler Bernoulli equation [34–36]

$$EI\frac{\partial^4 w(\omega, x)}{\partial x^4} - m_L \omega^2 w(\omega, x) = F(\omega, x) + F_{\text{fluid}}(\omega, x), \quad (6)$$

where x is the coordinate along the cantilever length, y along the cantilever width and z along the cantilever thickness, $w(\omega, x)$ is the deflection in the z direction at coordinate x and at radial frequency ω, E is the Young's modulus of the cantilever material, I is the moment of inertia of the cross section at coordinate x with respect to the y axis, $F(\omega, x)$ is the actuation force per unit length at coordinate x. In the case of a concentrated force at the free end: $F(\omega, x) = F_0(\omega)\delta(x - L)$, δ being the Dirac function, $F_{\text{fluid}}(\omega, x)$ is the force per unit length exerted by the fluid on the cantilever at coordinate x, m_L is the mass per unit length of the microcantilever.

The hydrodynamic force can be expressed [37, 38]

$$F_{\text{fluid}}(\omega, x) = (-g_1 - j\omega g_2) j\omega w(\omega, x), \quad (7)$$

with the terms g_1 and g_2 representing the viscous and inertial effects, respectively.

According to [39] the following simple expressions may be used to quantify the hydrodynamic force [36]:

$$g_1 = \frac{\pi}{4}\rho b^2 \omega \left(b_1 \frac{\delta}{b} + b_2 \left(\frac{\delta}{b}\right)^2 \right),$$

$$g_2 = \frac{\pi}{4}\rho b^2 \left(a_1 + a_2 \frac{\delta}{b} \right), \quad (8)$$

with $\delta = \sqrt{2\eta/\rho_f \omega}$ (fluid layer thickness over which the imposed (cantilever) velocity decays by a factor of e : 2.72); $a_1 : 1.0553$, $a_2 : 3.7997$, $b_1 : 3.8018$ and $b_2 : 2.7364$.

The solution of (6) depends on the hydrodynamic force which, according to (7) and (8), depends on the fluid density and fluid viscosity.

3.2. Silicon Devices and Examples of Measurements. In order to measure the spectrum of microcantilevers in different fluids, silicon chips have been designed and fabricated (Figure 4). The silicon chips are composed of one cantilever for the measurement and another one as a reference. The

(a)

CNRS-LAAS 30.0 kV 8.0 mm ×45 SE(M)   1.00 mm
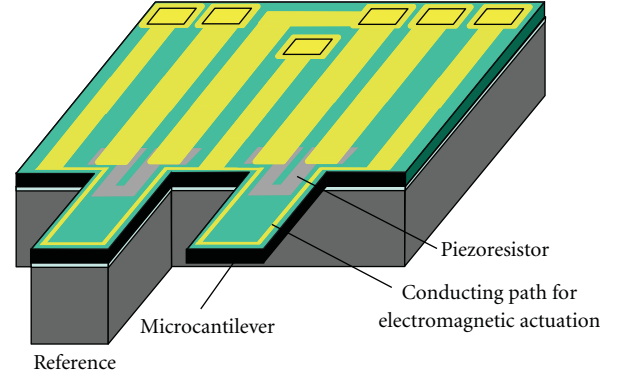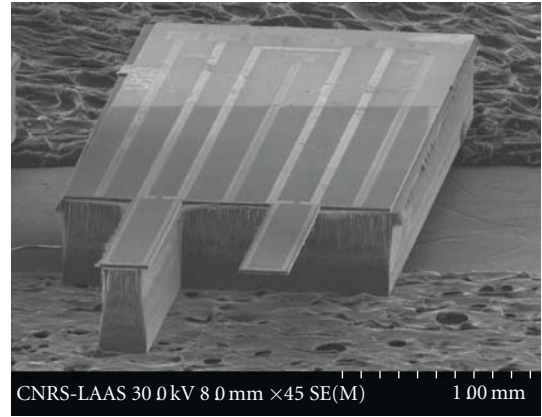
(b)

FIGURE 4: Silicon chips with integrated actuation and measurement designed for measurement of the complex shear modulus as a function of frequency.

TABLE 1: Geometry of the three microcantilevers.

Geometry	LL	LH	A
Length (μm)	2810	1440	500
Width (μm)	100	285	100
Thickness (μm)	20	20	20

reference cantilever has the same fluidic and electrical environment as the measurement cantilever, but because of its larger thickness (wafer thickness), it does not vibrate. In order to measure the spectrum, actuation and vibration measurement have been integrated. The actuation is an electromagnetic actuation (Laplace force obtained using a sinusoidal current in a conducting path placed on the microcantilever and a static magnetic field created by a magnet placed near the microcantilever). The electrical measurement of the vibration is performed by piezoresistors placed at the clamped-end of the two microcantilevers (the fabrication process is detailed elsewhere [40]).

Three different geometries have been used for the measurements (specimens "LL", "LH", and "A"). They all have the same thickness (SOI wafer) but different lengths and widths (Table 1).

Vibration measurements have been made with the different microcantilevers in different liquids: water and silicone oils with different viscosities. Examples of spectra measurements obtained using an optical vibrometer (MSA 500, Polytec: the out-of-plane detection mode is based on the Doppler Effect analysis of a laser beam reflection on the cantilever surface) are presented in Figure 5, due to the fact that unsolved electrical coupling issues between the magnetic actuation and the piezoresistive detection have required us to postpone the use of integrated sensing. The measured resonant frequency and quality factor are the same in both measurement systems, but the nonresonant portions of the spectra are quite different. The suppression of the electrical coupling is now under investigation.

As can be seen in Figure 5, the microcantilever spectrum depends on the properties of the surrounding fluid. Moreover, the frequency range for which the spectrum is modified depends on the geometry of the cantilever. It shows that each microcantilever can be used for a specific frequency range: the LL cantilever is for the lowest frequency, the LH cantilever for a low-mid frequency range and the A cantilever (not shown in Figure 5) for a higher frequency range.

3.3. Estimation of the Rheological Properties Using the Microcantilever Spectrum.

Using the spectra of the three microcantilevers and (6)–(8) three methods to extract the fluid properties have been developed. They have been called the fitting method (FM), the frequency dependent method (FDM), and the frequency dependent fixed density method (FD^{2}M). The general principles of these methods and some examples of results are presented hereafter.

3.3.1. Fitting Method (FM).

For this method, either the amplitude or the phase deflection spectrum measurement is used. The spectrum measurement is then fitted to a classical second-order low-pass filter response (9) in order to extract the numerical values of both the eigenfrequency, f_0, and the damping ratio ξ

$$w(\omega, L) = \frac{W_0}{1 - (f/f_0)^2 + 2\xi(f/f_0)j}, \tag{9}$$

where f is the actuation frequency ($\omega = 2\pi f$) and W_0 the static cantilever free-end deflection.

Then, using analytical equations based on the simplification of the solution of (6) in order to obtain (9), it is possible to calculate the values of the terms g_1 and g_2 at the eigenfrequency f_0. Then, based on (8), two analytical equations can be used to obtain the numerical values of both the fluid viscosity η and mass density ρ_f from the numerical values of both g_1 and g_2 at the eigenfrequency f_0. The equations for this method can be found in [16].

As an example of the spectra of the LH microcantilever in silicone oils presented in Figure 5, we obtain viscosity values of 11.2 cP and 27.3 cP and mass density values of 790 kg/m^3 and 951 kg/m^3, respectively, for the 10 cP and 20 cP silicone oils. In fact, the viscosity of these silicone oils is temperature dependent. They have been measured at the temperature 19.5°C (temperature of the measurement with

microcantilever made in a clean room at fixed temperature) using a classical cone/plane rheometer and 10.6 cP and 22.3 cP have been measured.

The advantage of this method compared to the one based on the measurement of the resonant frequency and quality factor [21–24] is that no resonant phenomenon is needed, because the eigenfrequency and damping ratio exist even for high damping and even if there is no resonance. Thus, the fitting method can be used for a higher viscosity range. Moreover, the only required calibration is the measurement of the resonant frequency in air, and all the estimations are based on the use of analytical equations involving no iteration.

The major limitation of this method is that only the fluid viscosity at one frequency per device (i.e., the eigenfrequency of the device in the fluid) is measured. In other words, this method mainly addresses Newtonian fluids.

3.3.2. Frequency Dependent Method (FDM).

For this method, both the amplitude and the phase deflection spectrum measurements are needed. Using analytical equations based on the simplification of the solution of (6), it is possible to calculate the values of the terms g_1 and g_2 at each frequency of measurement. Using (8), two analytical equations can be used to obtain the numerical values of both the fluid viscosity η and mass density ρ_f from the numerical values of both g_1 and g_2 at each frequency of measurement. The equations for this method can be found in [17, 18].

Without calibration and using only the estimated resonant frequencies in air for three cantilevers, the variations of both viscosity and density of 20 cP silicone oil over a wide frequency bandwidth have been calculated as shown in Figure 6. We can see that the viscosity is almost constant over a large frequency range (from 1 kHz to 50 kHz). The discontinuity between LL and LH results may come from the fact that the method requires an accurate value of the static deflection which is not trivial to be obtained due to low-frequency noise. It can be seen that for higher frequencies (>50 kHz), the viscosity seems to decrease with the frequency, implying shear-thinning behavior, that is, the sample is likely non-Newtonian.

The advantage of this method compared to the FM is that for each device the viscosity is measured over a frequency range and not only for one frequency. The limitation of this method is that the elasticity of the fluid is not taken into account.

3.3.3. Frequency Dependent Fixed Density Method (FD^{2}M).

For this method, the first step is exactly the same as for the frequency dependent method: using the amplitude deflection spectrum measurement, the phase deflection spectrum measurement and analytical equations based on the simplification of the solution of (6), the values of the terms g_1 and g_2 at each frequency of measurement are calculated. Then, by modifying (8) for the case of a viscoelastic fluid (the viscosity term is replaced by the term $G^*/(j\omega)$), two analytical equations can be used to obtain at each frequency of measurement the numerical values of
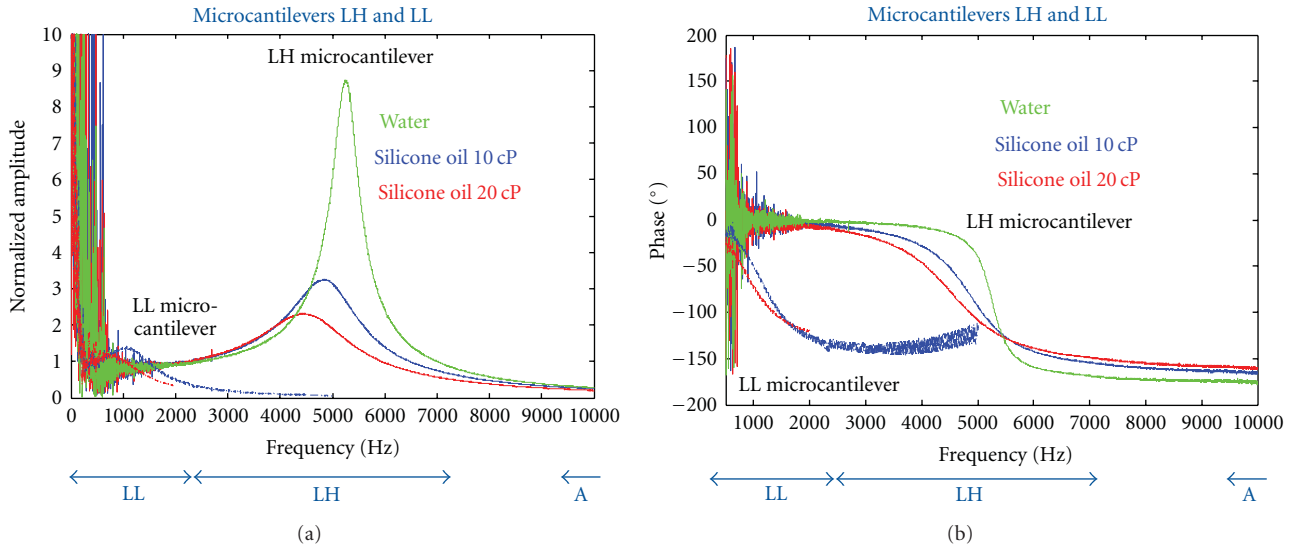
FIGURE 5: Examples of measurements of the displacement spectrum of microcantilevers LH and LL in different fluids (water, silicone oils of 10 cP and 20 cP viscosity) at 19.5°C.
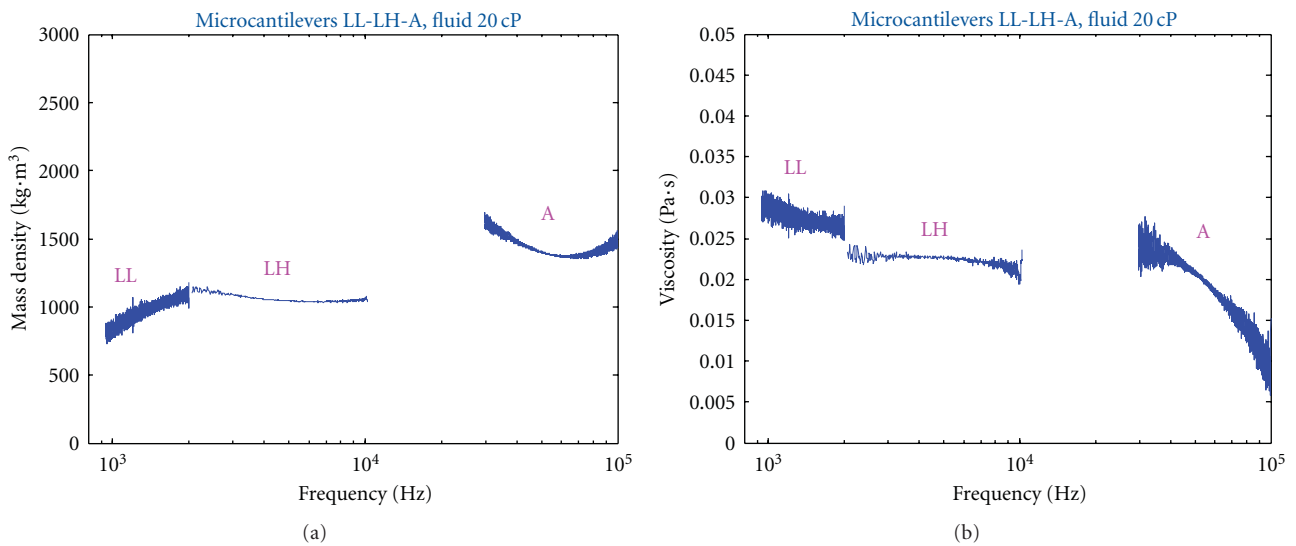

FIGURE 6: Variation of the mass density and viscosity of the 20 cP silicone oil with frequency using three microcantilevers (LL, LH, and A) applying the frequency dependent method (FDM).

g_1 and g_2, from which the real (G') and imaginary (G'') parts of the fluid's shear modulus may be obtained at each frequency. The equations for this method are given in [19].

Figure 7 shows the variation of viscoelastic parameters of the 20 cP silicone oil over a large frequency range. The low-frequency data were estimated using a classical rheometer of cone-plate geometry. The higher-frequency viscoelastic data could be calculated from the microcantilever deflection spectra (Figure 5) by applying the FD^{2}M Method. As can be seen in Figure 7, a feasible continuity between the macro- and microrheological data has been achieved over a large frequency bandwidth although the presence of some missing data arises from the lack of cantilevers of appropriate dimension to cover the missing parts. In general, the viscous G'' and the elastic G' moduli are linearly increasing with frequency and G'' is always higher than G', indicating the viscous nature of the sample up until 50 kHz, at which point the moduli display a crossover and G' becomes larger than G''. The Newtonian nature of the sample is well presented by the independence of the complex viscosity of the frequency until 50 kHz beyond which the viscosity exhibits shear-thinning implying the transition to non-Newtonian behavior.

The advantage of this method compared to the FDM is that for each device, both the real G' and imaginary G'' parts of the shear modulus are measured over a frequency range. The limitation of this method comes from the fact that the fluid mass density should be known and that an accurate value of the static deflection has to be extracted from the spectrum measurement.
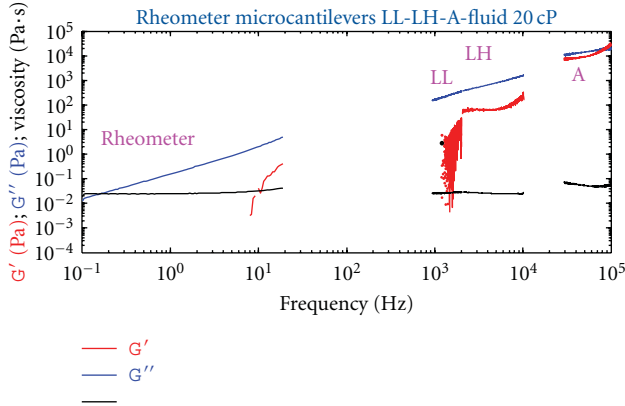
FIGURE 7: Estimation of the rheological properties (G', G'' and $|\eta^*|$) of the silicon oil 20 cP with the three microcantilevers (LL, LH and A) using the frequency dependent fixed density method (FD^{2}M).

4. Conclusion and Future Work

Different in situ rheological measurements using microcantilevers have been demonstrated in this paper. With the new extended methods presented herein, only a small amount of fluid is needed to determine the viscoelastic moduli (G' and G'') of the complex fluids. Depending on the methods, the measurement can be carried out at different frequencies or at different shear rates.

Improvements to the methods are planned for the future with the ultimate goal being to utilize microcantilevers to reliably answer the fundamental question of rheology: "how does matter flow?" For method 1, measurements using textured solid surfaces will be made and the elastic behavior of complex fluids will also be studied by a method using the measurement of the second harmonic of the cantilever deflection which depends on the normal hydrodynamic force exerted on the sphere. For method 2, in order to have measurements at different stress levels as in classical rheometry, measurements under flow conditions will be carried out. Also, many optimizations can be achieved for method 2 as follows:

(i) optimization of the geometry of the cantilevers in order to (i) maximize their sensitivity and (ii) span the 0.5–100 kHz frequency range with no discontinuity,

(ii) investigation of the use of in-plane vibrations instead of out-of-plane vibrations,

(iii) obtain a better understanding and control of the temperature effects [41]; this issue is important due to the very high sensitivity of the calculated values of G' and G'' to any variation of the deflection spectra.

Lastly, in order to deliver easy-to-use microrheometers to rheologists, a complete integrated actuation and detection system must be finalized for all methods.

References

[1] F. A. Morrison, *Understanding Rheology*, Oxford University Press, New York, NY, USA, 2001.

[2] V. Breedveld and D. J. Pine, "Microrheology as a tool for high-throughput screening," *Journal of Materials Science*, vol. 38, no. 22, pp. 4461–4470, 2003.

[3] F. C. MacKintosh and C. F. Schmidt, "Microrheology," *Current Opinion in Colloid and Interface Science*, vol. 4, no. 4, pp. 300–307, 1999.

[4] T. A. Waigh, "Microrheology of complex fluids," *Reports on Progress in Physics*, vol. 68, no. 3, pp. 685–742, 2005.

[5] M. L. Gardel, M. T. Valentine, and D. A. Weitz, "Microrheology," in *Microscale Diagnostic Techniques*, K. S. Breuer, Ed., Springer, Berlin Heidelberg, Germany, 2005.

[6] N. Willenbacher and C. Oelschlaeger, "Dynamics and structure of complex fluids from high frequency mechanical and optical rheometry," *Current Opinion in Colloid and Interface Science*, vol. 12, no. 1, pp. 43–49, 2007.

[7] F. Ortega, H. Ritacco, and R. G. Rubio, "Interfacial microrheology: particle tracking and related techniques," *Current Opinion in Colloid and Interface Science*, vol. 15, no. 4, pp. 237–245, 2010.

[8] P. Cicuta and A. M. Donald, "Microrheology: a review of the method and applications," *Soft Matter*, vol. 3, no. 12, pp. 1449–1455, 2007.

[9] B. Jakoby and M. J. Vellekoop, "Viscosity sensing using a love-wave device," *Sensors and Actuators A*, vol. 68, no. 1, pp. 275–281, 1998.

[10] B. Jakoby and M. J. Vellekoop, "Properties of love waves: applications in sensors," *Smart Materials and Structures*, vol. 6, no. 6, pp. 668–679, 1997.

[11] B. Jakoby, M. Scherer, M. Buskies, and H. Eisenschmid, "An automotive engine oil viscosity sensor," *IEEE Sensors Journal*, vol. 3, no. 5, pp. 562–568, 2003.

[12] S. J. Martin, G. C. Frye, and K. O. Wessendorf, "Sensing liquid properties with thickness-shear mode resonators," *Sensors and Actuators A*, vol. 44, no. 3, pp. 209–219, 1994.

[13] S. J. Martin, V. E. Granstaff, and G. C. Frye, "Characterization of a quartz crystal microbalance with simultaneous mass and liquid loading," *Analytical Chemistry*, vol. 63, no. 20, pp. 2272–2281, 1991.

[14] D. C. Ash, M. J. Joyce, C. Barnes, C. J. Booth, and A. C. Jefferies, "Viscosity measurement of industrial oils using the droplet quartz crystal microbalance," *Measurement Science and Technology*, vol. 14, no. 11, pp. 1955–1962, 2003.

[15] B. Jakoby, R. Beigelbeck, F. Keplinger et al., "Miniaturized sensors for the viscosity and density of liquids—performance and issues," *IEEE Transactions on Ultrasonics, Ferroelectrics, and Frequency Control*, vol. 57, no. 1, Article ID 5361530, pp. 111–120, 2010.

[16] M. Youssry, N. Belmiloud, B. Caillard, C. Ayela, C. Pellet, and I. Dufour, "A straightforward determinationof fluid viscosity and density using microcantilevers: from experimental data to analytical expressions," *Sensors and Actuators A*. In press.

[17] N. Belmiloud, I. Dufour, A. Colin, and L. Nicu, "Rheological behavior probed by vibrating microcantilevers," *Applied Physics Letters*, vol. 92, no. 4, Article ID 041907, 3 pages, 2008.

[18] M. Youssry, B. Caillard, C. Ayela, C. Pellet, and I. Dufour, "Microrheology of newtonian fluids using microcantilever," in *Proceedings of the 2nd IASTED International Conference on Nanotechnology and Applications (NANA '10)*, pp. 540–546, Cambridge, Mass, USA, November 2010.

[19] N. Belmiloud, "Microrheomètre sur puce pour chimie haut débit," Ph.D. thesis, Université Bordeaux, 2008.

[20] A. Maali and B. Bhushan, "Nanorheology and boundary slip in confined liquids using atomic force microscopy," *Journal of Physics Condensed Matter*, vol. 20, no. 31, p. 315201, 2008.

[21] C. Bergaud and L. Nicu, "Viscosity measurements based on experimental investigations of composite cantilever beam eigenfrequencies in viscous media," *Review of Scientific Instruments*, vol. 71, no. 6, pp. 2487–2491, 2000.

[22] S. Boskovic, J. W. M. Chon, P. Mulvaney, and J. E. Sader, "Rheological measurements using microcantilevers," *Journal of Rheology*, vol. 46, no. 4, pp. 891–899, 2002.

[23] M. Hennemeyer, S. Burghardt, and R. W. Stark, "Cantilever micro-rheometer for the characterization of sugar solutions," *Sensors*, vol. 8, no. 1, pp. 10–22, 2008.

[24] A. Agoston, F. Keplinger, and B. Jakoby, "Evaluation of a vibrating micromachined cantilever sensor for measuring the viscosity of complex organic liquids," *Sensors and Actuators A*, vol. 123-124, pp. 82–86, 2005.

[25] H.-J. Butt, B. Cappella, and M. Kappl, "Force measurements with the atomic force microscope: technique, interpretation and applications," *Surface Science Reports*, vol. 59, no. 1–6, pp. 1–152, 2005.

[26] C. Neto, D. R. Evans, E. Bonaccurso, H.-J. Butt, and V. S. J. Craig, "Boundary slip in Newtonian liquids: a review of experimental studies," *Reports on Progress in Physics*, vol. 68, no. 12, pp. 2859–2897, 2005.

[27] A. J. Goldman, R. G. Cox, and H. Brenner, "Slow viscous motion of a sphere parallel to a plane wall-I motion through a quiescent fluid," *Chemical Engineering Science*, vol. 22, no. 4, pp. 637–651, 1967.

[28] O. I. Vinogradova, "Drainage of a thin liquid film confined between hydrophobic surfaces," *Langmuir*, vol. 11, no. 6, pp. 2213–2220, 1995.

[29] R. G. Horn, O. I. Vinogradova, M. E. Mackay, and N. Phan-Thien, "Hydrodynamic slippage inferred from thin film drainage measurements in a solution of nonadsorbing polymer," *Journal of Chemical Physics*, vol. 112, no. 14, pp. 6424–6433, 2000.

[30] V. S. J. Craig, C. Neto, and D. R. M. Williams, "Shear-dependent boundary slip in an aqueous Newtonian liquid," *Physical Review Letters*, vol. 87, no. 5, Article ID 054504, pp. 054504/1–054504/4, 2001.

[31] E. Bonaccurso, M. Kappl, and H.-J. Butt, "Hydrodynamic force measurements: boundary slip of water on hydrophilic surfaces and electrokinetic effects," *Physical Review Letters*, vol. 88, no. 7, pp. 761031–761034, 2002.

[32] E. Bonaccurso, H.-J. Butt, and V. S. J. Craig, "Surface roughness and hydrodynamic boundary slip of a Newtonian fluid in a completely wetting system," *Physical Review Letters*, vol. 90, no. 14, pp. 144501/1–144501/4, 2003.

[33] C. D. F. Honig and W. A. Ducker, "No-slip hydrodynamic boundary condition for hydrophilic particles," *Physical Review Letters*, vol. 98, no. 2, Article ID 028305, 2007.

[34] S. Timoshenko, *Theory of Elasticity*, Classic Textbook Reissue Series, McGraw-Hill, 1970.

[35] R. D. Blevins, *Formulas for Natural Frequency and Mode Shape*, Van Nostrand Reinhold, New York, NY, USA, 1979.

[36] J. E. Sader, "Frequency response of cantilever beams immersed in viscous fluids with applications to the atomic force microscope," *Journal of Applied Physics*, vol. 84, no. 1, pp. 64–76, 1998.

[37] F. R. Blom, S. Bouwstra, M. Elwenspoek, and J. H. J. Fluitman, "Dependance of the quality factor of micromachined silicon beam resonators on pressure and geometry," *Journal of Vacuum Science and Technology B*, vol. 10, pp. 19–26, 1992.

[38] L.D. Landau, E. M. Lifshitz, J. B. Sykes, and W. H. Reid, *Fluid Mechanics*, Reed Educational & Professional Publishing Ltd, 2nd edition, 2000.

[39] A. Maali, C. Hurth, R. Boisgard, C. Jai, T. Cohen-Bouhacina, and J. P. Aimé, "Hydrodynamics of oscillating atomic force microscopy cantilevers in viscous fluids," *Journal of Applied Physics*, vol. 97, no. 7, Article ID 074907, pp. 1–6, 2005.

[40] D. Saya, T. Leïchlé, J. B. Pourciel, F. Mathieu, C. Bergaud, and L. Nicu, "Contact force control of piezoresistive cantilevers with in-plane nanotips for femtoliter droplet deposition," *Microelectronic Engineering*, vol. 85, no. 5-6, pp. 1341–1345, 2008.

[41] S. Kim and K. D. Kihm, "Experimental verification of the temperature effects on Sader's model for multilayered cantilevers immersed in an aqueous medium," *Applied Physics Letters*, vol. 89, no. 6, Article ID 061918, 2006.

Research Article

Instrument for Label-Free Detection of Noncoding RNAs

Peter Noy,[1] Roger Steiner,[1] Joerg Voelkle,[1] Martin Hegner,[2] and Christof Fattinger[1]

[1] *F. Hoffmann-La Roche Ltd., Pharma Research and Early Development, Discovery Technologies, 4070 Basel, Switzerland*
[2] *CRANN—The Naughton Institute, School of Physics, Trinity College Dublin, Dublin 2, Ireland*

Correspondence should be addressed to Peter Noy, peter.noy@roche.com

We set up a label-free direct binding assay for the detection of noncoding RNAs. The assay is based on nanomechanical cantilever arrays for the detection of surface stress induced by immobilized biomolecules and their interaction partners. We used various means to significantly reduce the drift of the cantilever readout that was a prominent feature in experiments with readout in stationary fluid before and after sample injection. Major improvements were achieved by focusing on a faster system equilibration (for instance temperature control and diffusion independence). Experimental protocols were improved to provide user-friendly and less time-consuming measurements. Further enhancements were achieved by, for example, using pre-gold-coated cantilever array wafers compared to individually prepared ones and a directly implemented data analysis tool as real-time feature of the measurement software. We have demonstrated picomolar specific biomarker target detection and can easily distinguish modified targets with single-nucleotide mismatches that hybridize with lower affinity.

1. Introduction

Nanomechanical sensing systems based on cantilever arrays are a basic research tool for exploring label-free assays. Investigators have shown several static mode applications for the detection of biological binding partners such as DNA hybridization [1–3] and receptor-ligand binding [4–7]. Our focus lies on the label-free detection of noncoding RNAs for medium throughput assays where half automated processes and less time-consuming protocols play an important role. Therefore our intention was to set up a stable and reliable device for this application in the field of genomics.

The detection of noncoding RNAs is of interest for monitoring miRNA or siRNA levels as biomarkers or for therapeutic approaches [8]. The present state of the art detection method for RNA is the branched DNA assay or DNA ELISA. As in an ELISA assay, an immobilized capture probe binds the target sequence. Afterwards the sandwich structure is completed with a detection probe (annotated as label extender). This label extender then binds the branched DNA with label probe. The labeled branches ensure a strong enough signal for detection [9]. The advantages of the DNA ELISA is that no amplification is necessary and no reverse transcription such as that in qPCR is needed. Measurements

can be done directly on cell lysates. The fact that time-consuming assay protocols are inherent for this ELISA type assay is a disadvantage. Furthermore, there is one major limitation: to attach the label we need a certain amount of nucleotides from the target strand which are not available for recognition and to ensure specificity.

For comparative measurement we refer to a publication where the label-free detection of biomarker transcripts in human RNA with a nanomechanical cantilever setup was shown [10].

As proof of concept for the newly designed setup our goal was to detect a single-stranded 21mer oligonucleotide at 100 pM in a physiological buffer solution.

For the detection of successful hybridization experiments we measured the transduced surface stress which accumulated depending on the amount of specifically bound ssDNA biomolecules. We operated our device in static mode and measured in liquid. The induced bending of the cantilever (which lies in the nanometer range) is measured by reflecting a laser beam on the top of the cantilever and pointing it towards a position sensitive detector (PSD) as described in [11, 12]. Surface stress is induced by the interaction between immobilized biomolecules on the ssDNA biofunctionalized side of the cantilever bar and their interaction partners in

an injected solution. Various forces such as intermolecular interactions, electrostatic forces, and changes in the electronic density of the cantilever surface lead to the resulting surface stress [13].

By subtracting the deflection signal of a nonspecific reference cantilever from the main signal, parasitic effects such as drift due to small temperature changes and nonspecific binding can be eliminated [13, 14].

Since measurable amount of signal drift is present in all known label-free detection methods we focused on its reduction by stabilizing the major external factors which affect drift in our nanomechanical setup. This was achieved by implementing a fast local temperature regulation system and measurement in continuous liquid flow. Our goal was to optimize the system towards semiautomatic device handling, which is essential for industrial applications.

To assist the interpretation of the recorded data we developed a real time analysis software which applies simple operations and plots the results concurrently with the measurement.

2. Instrumentation, Materials, and Methods

The cantilever deflection is measured by tracking a reflected laser spot on a position-sensitive detector (PSD) (1L10-10-A SU15, SiTek Electro Optics, Sweden). As laser source we chose pigtail laser diodes of 635 nm wavelength (HL6320G, Opnext Japan Inc., Japan) and operated them in constant power mode. By arranging eight laser coupled fibers in a linear array we achieved readout of the eight cantilevers through their sequential illumination.

Our setup is divided into three parts. The main part is a temperature-controlled box containing the cantilever instrument and the fluidic system (Figure 1). To keep the temperature at the cantilever array stable, we installed two controlled loops. (i) An external flow cycle thermostat (ministat 125, Peter Huber Kaltemaschinenbau GmbH, Germany) to stabilize the temperature inside the temperature-controlled box. (ii) The second temperature regulation module is a Peltier element mounted inside the measurement chamber at a distance of about 2 mm from the cantilevers. The Peltier element was regulated by a Peltier controller which is normally used for laser temperature stabilization (LDT-5525, ILX LIGHTWAVE, USA).

We performed all measurements in liquid phase. Two syringe pumps (neMESYS system, Cetoni GmbH, Germany) pull the system liquid and samples through the measurement chamber. To compensate for the pressure loss due to pulling we applied 80 mbar (nitrogen) overpressure on all sample vessels and the system buffer reservoir. Halar tubing (Ercat-ech AG, Switzerland) was used to reduce loss of probe molecules in the sample due to adsorption onto the tubing surface.

For measurements the cantilever can be installed either under dry conditions or in a prefilled system where the chamber and tubing are filled with buffer. In both cases we flush the system with CO_2 prior to filling with buffer. CO_2
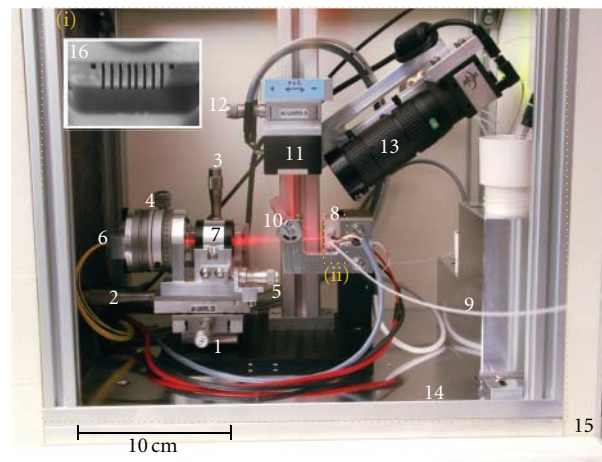

Figure 1: View inside temperature-controlled box containing the cantilever instrument. Laser ray path visible due to slight haze. (1, 2, 3) x, y, z positioning; (4) parallel alignment of fibers to cantilevers; (5) longitudinal focusing on cantilevers; (6) optical fibers (laser sources); (7) lens; (8) flow chamber (holds cantilever array chip); (9) tubing to syringe pump; (10) mirror with tilt function; (11) position-sensitive detector (PSD); (12) PSD alignment; (13) camera module; (14) ground plate connected to flow cycle thermostat; (15) thermal insulated box; (16) inset of cantilever array image mounted in flow chamber (8) taken with the camera module (13); (i) and (ii) illustrate the two temperature-controlled zones.

dissolves 80 times better in water than nitrogen and leads to a gas bubble-free fluidic system.

In addition to the temperature-controlled box the setup comprises a 19″ rack containing the laser controller and power supply for the PSD.

The setup is controlled by LabView (NI PCI-6221 interface and LabView software kit, National Instruments, Switzerland). All measured values are recorded and processed by LabView software. The data analysis is based on algorithms which were tested and previously applied for kinetic microarray signals [15].

We used cantilever arrays with eight cantilever sensors precoated with 2 nm titanium 20 nm gold (IBM Research GmbH, Switzerland). External dimensions of these sensors are as follows: 500 μm length, 100 μm width, and 0.5 μm thickness. To regenerate and clean the gold surface of environmental organics for subsequent ssDNA functionalisation, the arrays were treated with UV ozone for 60 minutes (radiation flux at 185 nm: ~4 W; ambient O_2) prior to use [16]. An oxygen plasma treatment to clean the gold surface is not recommended due to the widely distributed electron energy leading to radiation damages and a poor controllability [16].

All measurements were performed under continuous flow (10 μL/min for equilibration before and after the injections and 150 μL/min for the probe injection and wash step) using the above mentioned syringe pumps. Cantilever arrays were functionalized with thiol-modified ssDNA (Microsynth, Switzerland) for 60 minutes in acetic acid-triethylamine solution buffer in a home-built capillary device. Capillaries allow individual functionalisation of
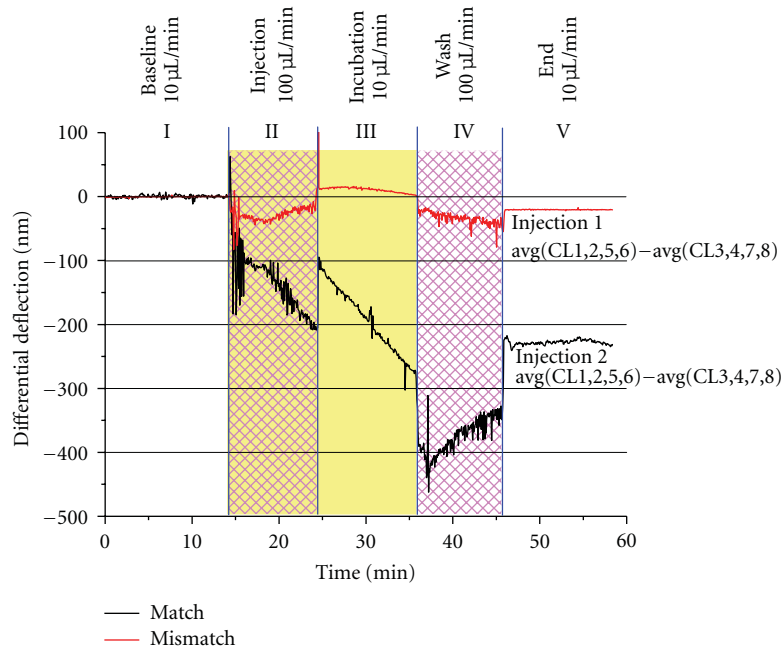
FIGURE 2: Overlay of two consecutive experiments to prove the detection of a 100 pM antisense strand. The graph shows the significant difference between an injection of 100 pM antisense match strand (black curve) and an injection of 100 pM antisense mismatch strand (red curve, the mismatch has two nonmatching base pairs in the centre of the target). Injecting the match sample induces approximately −200 nm differential deflection, where else the injection of the mismatch configuration leads to almost no differential signal. Phase (I) shows the recorded baseline at 10 μL/min buffer flow. (II) 1,000 μL sample injection at 100 μL/min. (III) incubation phase at 10 μL/min. (IV) flushing with buffer 100 μL/min. (V) resulting differential deflection after injection cycle is completed (10 μL/min buffer flow). Curves correspond to the differential deflection signal of positive minus reference cantilever (CL). Therefore the bending of the cantilevers is not absolute but differential deflections. The two injections were performed in series on the same cantilever array chip. A baseline correction, normalization, averaging, and differential signal calculation (probe minus reference) were done according to the literature [15]. Hatched area highlights the increased flow speed during injection and wash phase. Colored area indicates the presence of probe molecules in the flow chamber.

the various sensors. The DNA sequences chosen were AGAATAGGTATTTTTCCACAT for the biomarker target and AGAATAGGTATAATTCCACAT for the mismatch sequence. The chosen sequences do not tend to form hairpins and do not dimerize. In all experiments the following thiolated ssDNA oligonucleotides were used to functionalize the cantilever interface. (Sensor sequence: ATGTGGAAAAAT-ACCTATTCT-C6 linker-SH, Reference sequence: CTTACG-CTGAGTACTTTGA-C6 linker-SH). We used PBS (Invitrogen, Switzerland) as running and hybridization buffer.

3. Results and Discussion

With the described setup, we could detect a 100 pM antisense strand and differentiate between a perfect match and mismatch sequence. Figure 2 shows the overlay of two consecutive experiments. Before each injection a stable baseline was recorded to ensure that all cantilevers were equilibrated (phase (I)). Due to the automated injection program the timing for the following injection steps was the same for each experiment. This allowed the overlay of the two sequential experiments shown in Figure 2. The effect of switching the valve from running buffer reservoir to the probe container and changing the flow speed from 10 μL/min to 100 μL/min is visible at the beginning of the

sample injection in phase (II). It takes about 3 minutes until the sample reaches the chamber with the cantilevers. This explains why the slope did not change significantly until mid phase (II). The heavy fluctuations can be explained by the change in refractive index, flow effects, and the exchange of molecules in the chamber before a new equilibration is set. After 10 min the sample (1,000 μL) is completely injected, the valve switches back to running buffer, and the flow speed is decreased to 10 μL/min (transition to phase (III)). In phase (III) the chamber is still filled with probe solution. A stable equilibrium is not reached during this incubation period. Several reactions leading to a cantilever deflection as described in [13] tend to occur. To remove the remaining probe solution and wash the chamber the buffer flow was increased (phase (IV)) to 100 μL/min. We flushed with 1,000 μL buffer. Here we see again that the delay before the probe solution in the system was fully replaced by buffer (change in slope). The peak at the changing point can be explained by the change in electrostatic conditions of the plain buffer solution compared to the buffer solution with probes. Fast effects such as valve switching and bulk buffer changes cannot be fully recorded due to the comparatively slow data acquisition (0.25 Hz), and therefore sequential injection traces are not completely identical. Finally the program switches back to the standby conditions
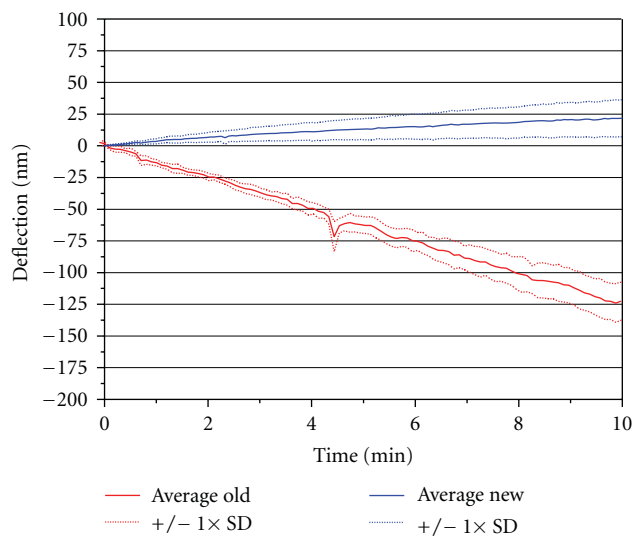
FIGURE 3: Typical drift before (red curve) and after implementation (blue curve) of means for drift reduction (continuous flow, temperature regulation, etc as described in this paper). Curves show the average of the raw data from 8 recorded cantilevers and the corresponding standard deviation. Curves have an offset at zero. Red curve measured under stationary conditions (flow: $0\,\mu$L/min). Blue curve measured in flow ($10\,\mu$L/min).

($10\,\mu$L/min buffer flow), and the resulting deflection values are monitored. Compared to the end point of the deflection in phase (III), the start point of phase (V) is slightly higher ($\sim$50 nm) although we have the same flow speed in phase (III) and (V): $10\,\mu$L/min. A small amount of deflection is lost due to the dissolution of weakly bound strands (not fully hybridized) during the washing step. The two injections shown (red curve and black curve) were recorded sequentially. First, the negative probe (mismatch configuration) was injected and after a new equilibration the match injection was monitored. Finally the two starting points of the baselines were shifted to zero and the graphs plotted in an overlay. The resulting net deflection of $\sim$200 nm for the 100 pM matching probe injection is repeatedly measured in our experiments. The resulting surface stress of about 9 mN m^{-1} is relatively high compared to previous experiments such as [10] (Young's modulus (Si): 130 GPa, Poisson ratio: 0.28). Reasons therefore could be due to longer cantilever functionalization times and due to different buffer properties which affect steric hindrance and ionic repulsion of the molecules.

By means of temperature stabilization and continuous flow measurements drift in the raw deflection signal was reduced from $\sim$12 nm/min to $\sim$2.5 nm/min as shown in Figure 3. The described setup and protocols represent a significant drift reduction by a factor 5 compared to previous experiments with readout in stationary fluid before and after sample injection. The gain in accuracy is especially of importance for the hybridization measurement with reaction times >1 min. The typical drift shown in Figure 3 was observed in all actual measurements.

In terms of electronic parts we used state of the art components. The amplifier has a noise level of approximately

$1\,\mu$V, the PSD $\sim$3 μV (BW = 100 Hz). The analogue digital converter NI PCI-6221 with $\sim$122 μV noise level is therefore the main source of electric disturbance (values from datasheet stated in V$_{RMS}$ to illustrate the critical components). Therefore we adjusted the full range scale to the maximum signal voltage and took the average over several measurement points (1,000 samples in 500 ms). This is possible due to the slow reaction time (>1 Hz) compared with the sampling rate characteristics of the electronic parts. Furthermore we optimized the settling time of the laser controller and adjusted the data processing to let the laser stabilize after switching. Before averaging, we discard the first half of the data points to be sure to have a stable laser signal. The remaining 500 samples are still enough for noise reduction by averaging. Due to the sequential readout a too long sampling time might lead to missing a reaction event.

By placing a temperature-controlling element close to the cantilever array we obtained a controlled loop with very short time constant for temperature equilibration. Time to regulate the temperature in the chamber from 21°C room temperature to 25°C setpoint is approximately 0.5 min. The much slower flow cycle thermostat regulation loop than that of the Peltier element leads to a stable temperature for all probe vessels, the buffer reservoir, and surrounding elements. In addition, a large ($23 \times 35 \times 2.5$ cm) aluminum ground plate provides a good heat exchange. To regulate the temperature from room temperature to setpoint by the flow cycle thermostat it takes $\sim$50 min.

The two pulsation-free syringe pumps were embedded in our LabView control software. With two dosing modules an endless flow could be programmed, even for running measurements overnight. Besides electronic and temperature drifts the main portion of the overall drift visible in the deflection signal is drift due to diffusion effects (e.g., ionic exchanges between the cantilever surface and the surrounding liquid). The continuous flow led to a fast equilibration between the cantilever surface and the surrounding liquid which is diffusion independent. One feature which has to be taken into account when measuring in flow is the effect of the laminar flow on the cantilevers, as we see a deflection due to flow forces. In experiments with readout in stationary fluid before and after sample injection the liquid phase is moving during the injection process as well. This leads to significant flow induced deflections (see for instance in [10]). Depending on the position of the sensors relative to the liquid chamber channel the flow forces will be different for the eight cantilevers, inducing different additional bending that could potentially affect the measured deflection values. By measuring the baseline and the actual hybridization signal at equivalent buffer flow speeds, the comparability is given. The typical flow-induced bending by switching from stationary fluid to $10\,\mu$L/min is up to 7 nm. For the increased injection flow rate the induced bending is up to 400 nm (see, e.g., Figure 2). Stop flow read out with only a short "stop" phase to record the data points (much smaller time period than the drift kinetics) could add additional improvement.

Due to instrument design restrictions (flow path, lack of space, and temperature sensibility) we decided to set

up the flow with a syringe pump in pulling mode. The disadvantage with this pulling method is the risk of sucking air into the flow path. Small air bubbles will stick to the cantilever array and lead to an abortion of the measurement. By compensating the pressure loss with a positive pressure on the probe side we avoided these problems. Additionally, Halar tubing was chosen to avoid gas diffusion into the system. The gas permeability value for oxygen for Halar is similar to PEEK and $\sim$30 times less than Teflon (according to the specification guide from the provider). Moreover, Halar tubing is almost as flexible as Teflon tubing, in contrast to PEEK which would otherwise be a perfect material in terms of gas diffusion and low affinity for biomolecules.

Air bubbles tend to stick in small corners in the fluidic path and require a time-consuming procedure for their removal. CO_2 sparging allows fast fluidic system priming without any bubbles. The buffering characteristics of the solution and closing the CO_2 connection after priming ensure that the effect of the CO_2 on the acidity of the buffer is negligible.

4. Conclusion

Equilibration time and drift were significantly reduced by the fast temperature control system and continuous flow measurement. After installing the cantilever chip, it takes about 1.5 h until the system is ready to measure. The major time-consuming step is the cantilever functionalization although the protocol was simplified by using pre-gold-coated arrays and UV/O_3 activation. With CO_2 sparging, pressure compensation, and Halar tubing the formation of gas bubbles and their time-consuming removal was avoided. Further investigations into the effect of the continuous flow on the cantilevers will be carried out. The gain in drift reduction (approximately 10 nm/min) compared to the flow-induced bending ($\sim$7 nm) leads to the assumption that a measurement under continuous flow is an improvement. State-of-the-art electronic components and investigations into signal stability led to a stable and reliable device (fluctuations <5 nm for functionalized cantilever in liquid with a typical recording timescale of 0.25 Hz). Device control, measurement, and data analysis by LabView lead to a fast and straightforward workflow. The specific detection of a short oligonucleotide strand at 100 pM concentration in physiological buffer conditions demonstrated proof of concept of this setup.

Acknowledgments

References

[1] R. McKendry, J. Zhang, Y. Arntz et al., "Multiple label-free biodetection and quantitative DNA-binding assays on a nanomechanical cantilever array," *Proceedings of the National Academy of Sciences of the United States of America*, vol. 99, no. 15, pp. 9783–9788, 2002.

[2] F. Huber, N. Backmann, W. Grange, M. Hegner, C. Gerber, and H. P. Lang, "Analyzing gene expression using combined nanomechanical cantilever sensors," *Journal of Physics*, vol. 61, no. 1, article 090, pp. 450–453, 2007.

[3] J. Mertens, C. Rogero, M. Calleja et al., "Label-free detection of DNA hybridization based on hydration-induced tension in nucleic acid films," *Nature Nanotechnology*, vol. 3, no. 5, pp. 301–307, 2008.

[4] Y. Arntz, J. D. Seelig, H. P. Lang et al., "Label-free protein assay based on a nanomechanical cantilever array," *Nanotechnology*, vol. 14, no. 1, pp. 86–90, 2003.

[5] T. Braun, M. K. Ghatkesar, N. Backmann et al., "Quantitative time-resolved measurement of membrane protein-ligand interactions using microcantilever array sensors," *Nature Nanotechnology*, vol. 4, no. 3, pp. 179–185, 2009.

[6] T. Braun, N. Backmann, M. Vögtli et al., "Conformational change of bacteriorhodopsin quantitatively monitored by microcantilever sensors," *Biophysical Journal*, vol. 90, no. 8, pp. 2970–2977, 2006.

[7] N. Backmann, C. Zahnd, F. Huber et al., "A label-free immunosensor array using single-chain antibody fragments," *Proceedings of the National Academy of Sciences of the United States of America*, vol. 102, no. 41, pp. 14587–14592, 2005.

[8] R. W. Carthew and E. J. Sontheimer, "Origins and Mechanisms of miRNAs and siRNAs," *Cell*, vol. 136, no. 4, pp. 642–655, 2009.

[9] M. L. Collins, B. Irvine, D. Tyner et al., "A branched DNA signal amplification assay for quantification of nucleic acid targets below 100 molecules/ml," *Nucleic Acids Research*, vol. 25, no. 15, pp. 2979–2984, 1997.

[10] J. Zhang, H. P. Lang, F. Huber et al., "Rapid and label-free nanomechanical detection of biomarker transcripts in human RNA," *Nature Nanotechnology*, vol. 1, no. 3, pp. 214–220, 2006.

[11] H. P. Lang, R. Berger, C. Andreoli et al., "Sequential position readout from arrays of micromechanical cantilever sensors," *Applied Physics Letters*, vol. 72, no. 3, pp. 383–385, 1998.

[12] G. Meyer and N. M. Amer, "Simultaneous measurement of lateral and normal forces with an optical-beam-deflection atomic force microscope," *Applied Physics Letters*, vol. 57, no. 20, pp. 2089–2091, 1990.

[13] M. Godin, V. Tabard-Cossa, Y. Miyahara et al., "Cantilever-based sensing: the origin of surface stress and optimization strategies," *Nanotechnology*, vol. 21, no. 7, Article ID 075501, 2010.

[14] H. P. Lang, M. Hegner, E. Meyer, and C. Gerber, "Nanomechanics from atomic resolution to molecular recognition based on atomic force microscopy technology," *Nanotechnology*, vol. 13, no. 5, pp. R29–R36, 2002.

[15] T. Braun, F. Huber, M. K. Ghatkesar et al., "Processing of kinetic microarray signals," *Sensors and Actuators, B*, vol. 128, no. 1, pp. 75–82, 2007.

[16] W. Kern, *Handbook of Semiconductor Wafer Cleaning Technology—Science, Technology, and Applications*, Noyes Publications, 1993.

Research Article

An Astigmatic Detection System for Polymeric Cantilever-Based Sensors

En-Te Hwu,[1] Hsien-Shun Liao,[1, 2] Filippo G. Bosco,[3] Ching-Hsiu Chen,[1] Stephan Sylvest Keller,[3] Anja Boisen,[3] and Kuang-Yuh Huang[2]

[1] *Institute of Physics, Academia Sinica, Nankang, Taipei 11529, Taiwan*
[2] *Department of Mechanical Engineering, National Taiwan University, Taipei 10617, Taiwan*
[3] *Department of Micro- and Nanotechnology, Technical University of Denmark, 2800 Lyngby, Denmark*

Correspondence should be addressed to En-Te Hwu, whoand@phys.sinica.edu.tw

We demonstrate the use of an astigmatic detection system (ADS) for resonance frequency identification of polymer microcantilever sensors. The ADS technology is based on a DVD optical head combined with an optical microscope (OM). The optical head has a signal bandwidth of 80 MHz, allowing thermal fluctuation measurements on cantilever beams with a subnanometer resolution. Furthermore, an external excitation can intensify the resonance amplitude, enhancing the signal- to-noise ratio. The full width at half maximum (FWHM) of the laser spot is 568 nm, which facilitates read-out on potentially submicrometer-sized cantilevers. The resonant frequency of SU-8 microcantilevers is measured by both thermal fluctuation and excited vibration measurement modes of the ADS.

1. Introduction

Cantilever-based sensors have emerged as a promising label-free detection technique, which have been used for high-precision mass detection and biomolecular recognition. By surface functionalization, the cantilever can be modified specific to certain compounds detection. Molecules adsorbed to one side of the cantilever will deflect the cantilever due to changes in surface stress [1–3]. Alternatively, minute mass changes can be detected by monitoring the resonant frequency change of the cantilever for high-precision mass detections [4]. By monitoring surface stress changes, for example, DNA hybridization [5] and antibiotic-peptide binding [6] have been detected.

For detecting the vibrational amplitude and/or the deflection of a microcantilever, diverse methods such as optical [7], capacitive [8], piezoresistive and piezoelectric [9–11] have been applied. The optical lever technique, typically used in atomic force microscopy (AFM), is the most popular method for detecting deflections of micromechanical structures. A laser beam is focused on a microcantilever which reflects the beam onto a position-sensitive detector (PSD).

The distance between the microcantilever and the PSD magnifies the angular detection sensitivity that subnanometer cantilever deflections can be resolved [12, 13]. The optical lever technique needs a tedious and time-consuming adjustment process before measuring each cantilever own bending angle. Therefore, the optical lever method may not be an optimum solution for new technological tasks such as fast or simultaneous detection on large microcantilever arrays. Moreover, the laser spot size in most commercially available optical lever systems is several micrometers, which is difficult to measure submicrometer-sized structures.

Previously, an astigmatic detection system (ADS) is applied in an AFM system [14] for monitoring the AFM probes. The key component of the ADS is an optical head inside a DVD ROM drive. We have demonstrated that the atomic-scale thermal noise of an AFM probe can be measured by the ADS. In this work, we combine the ADS with an optical microscope (OM) for measuring microcantilever-based sensors made of polymer SU-8 [15].

The detection scheme of the ADS is shown in Figure 1(a). Through a collimator and an objective lens, a laser beam
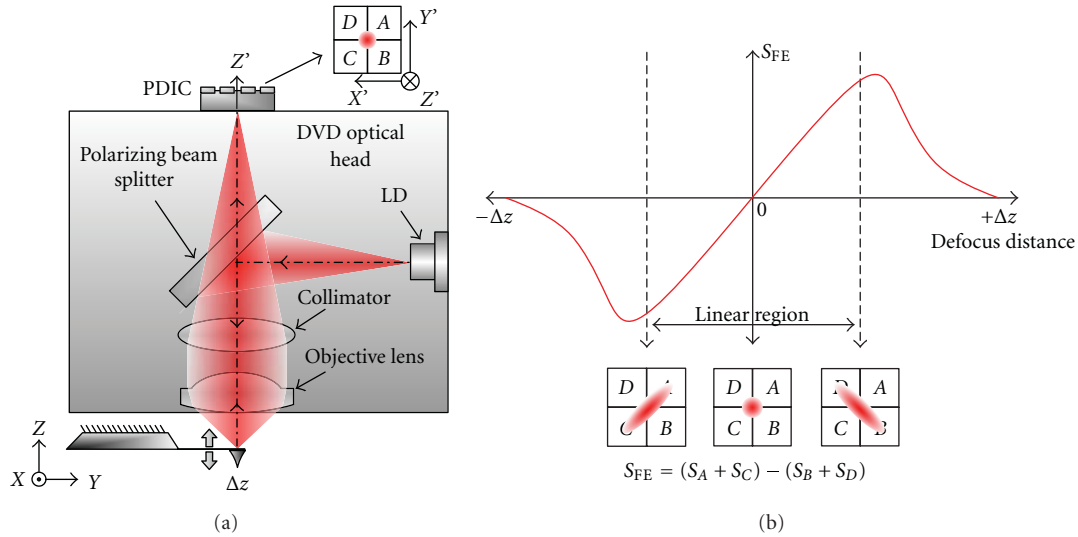
Figure 1: Detection scheme of the astigmatic detection system, (a) optical path configuration, (b) laser spot on PDIC, and the focus error signal; the linear region is about $6\,\mu$m.

generated by a laser diode (LD) is focused onto a cantilever. The cantilever reflects the laser beam back through a beam splitter, which perpendicularly reflects the laser beam onto the photodetector integrated chip (PDIC). The optoelectronic energy transformation is carried out by four independent photosensitive quadrants (A, B, C, D), which generate the signals of S_A, S_B, S_C, and S_D, respectively. When the ADS is focused on the cantilever, the laser spot on PDIC is circular shaped. The defocus distance Δz of the object induces a shape change of the laser spot, as shown in Figure 1(b). A corresponding focus error signal S_{FE} is defined as $S_{FE} = (S_A + S_C) - (S_B + S_D)$. For monitoring and accurate aligning the laser spot on the object, an OM with CMOS sensor, is combined to the optical path of the ADS.

Without angular adjustment, the ADS can still measure resonance frequencies of cantilevers with bending angle from -8- to 8-degree deviation. Compared with the optical lever technique, the large angular tolerance of the ADS makes high-speed measurement possible [16]. One of the main challenges is to be able to measure the resonant peak of the polymer cantilevers without reflective coatings. This would represent a very useful tool for employing the technology to out-of-the-lab applications, drastically reducing the size and cost of the readout setup. Furthermore, the SU-8 microcantilevers without coating can substantially simplify the manufacturing process and reduce the cost of the microcantilever-based biosensor. In this paper, we measure the resonant frequency of the microcantilevers in four conditions: with and without reflective coating and with and without external excitation.

2. SU-8 Microcantilevers Dynamic Analysis

Our developed microcantilevers are made of polymer SU-8, which possesses the advantages of simple processing, low Young's modulus for high force resolution and low sensitivity
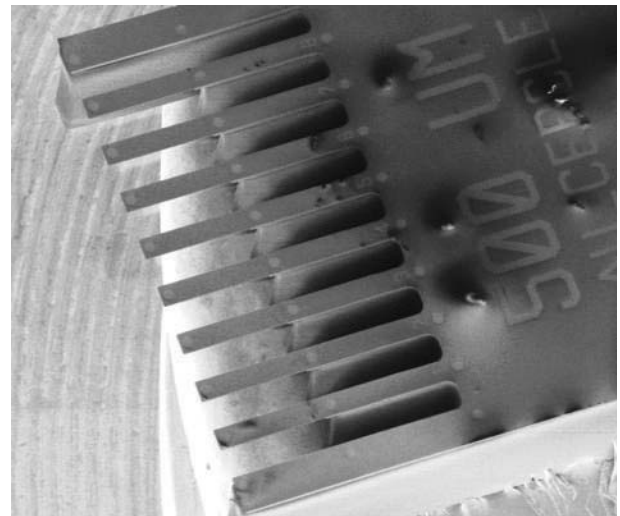
Figure 2: SEM image of eight SU-8 microcantilevers with gold pads.

to the environmental temperature [17]. Figure 2 shows an SEM image of eight SU-8 microcantilevers on one chip. Each microcantilever is $495\,\mu$m long, $100\,\mu$m wide, and $5.3\,\mu$m thick. On the free end of each microcantilever is a circular coated gold pad with a diameter of $50\,\mu$m and a thickness of 20 nm. The gold pads provide well-reflective surfaces for the optical detection.

In order to validate the performance of the ADS, analytical models and finite element methods (FEM-) are used to calculate the resonant frequencies of the SU-8 microcantilevers. Their mechanical properties are mainly influenced by shape, materials, and geometrical sizes. The spring constant and the fundamental resonant frequency of

Table 1: Mechanical properties and dimensions of an SU-8 microcantilever.

E	Young's modulus	4.2 ± 0.5 G N/m^2
ρ	Density	1200 kg/m^3
L	Length	$495\,\mu$m
W	Width	$100\,\mu$m
T	Thickness	$5.3 \pm 0.1\,\mu$m

Table 2: Simulated resonant frequencies by using FEMLAB.

First bending mode f_{1st}	6.59 ± 0.5 kHz
Second bending mode f_{2nd}	41.3 ± 3.3 kHz
Torsional mode f_T	66.2 ± 5.2 kHz

a homogeneous rectangular microcantilever in vacuum can be approximated by (1) and (2), respectively [18]

$$k = \frac{Ewt^3}{4L^3}, \tag{1}$$

$$f_{1st} = 0.162\sqrt{\frac{E}{\rho}}\frac{t}{L^2}. \tag{2}$$

Table 1 lists the mechanical properties and geometrical sizes of the SU-8 microcantilevers [19]. Based on these values, the calculated spring constant k and resonant frequency f_{1st} of the microcantilever are 0.128 ± 0.02 N/m and 6.55 ± 0.4 kHz, respectively.

By using finite element analysis software (FEMLAB), simulated resonant frequencies are listed in Table 2. The first bending mode frequency of the microcantilever is 6.43 kHz, which well-matches the theoretical value 6.55 ± 0.4 kHz calculated by (2).

The resonant frequency of the microcantilever is shifted by its mass change due to absorption of specific target molecules. For realizing a high mass sensitivity, the binding region for the target molecule can be confined to the free end of the microcantilever. The bound mass variation Δm can be associated with f_{1st} and the frequency variation Δf, as shown in

$$\Delta m = \frac{k}{4\pi^2}\left(\frac{1}{(f_{1st} + \Delta f)^2} - \frac{1}{f_{1st}^2}\right). \tag{3}$$

When Δf and the Δm are close to zero, (3) can be simplified as (4), which describes the sensitivity of the mass variation Δm to the frequency variation Δf

$$\frac{\Delta m}{\Delta f} = -\frac{k}{2\pi^2 f_{1st}^3}. \tag{4}$$

From the calculated spring constant $k = 0.128 \pm 0.02$ N/m and resonant frequency f_{1st} 6.55 ± 0.4 kHz, we can derive a sensitivity $\Delta m/\Delta f$ of -23.2 pg/Hz. Higher resonant frequency of the microcantilever can significantly enhance the measurement resolution of the mass. For a constant sampling rate, increasing the number of sampling data can also improve the measurement resolution of frequency, but it will slow down the measurement speed.

3. Experimental Setup

Figure 3 illustrates a block diagram of the ADS combined with an OM. Through an optomechanical adaptor, the ADS can be easily attached to the objective of the OM (Nikon Eclipse E100). The CMOS camera is employed to capture a magnified image of the cantilever and display the image on the PC monitor for controlling the alignment process. A light source from the bottom can illuminate the microcantilevers for enhancing the contrast of the optical image.

The ADS is based on a slim type DVD optical head which has a size of $50 \times 35 \times 6$ mm. The laser diode of the ADS generates a laser beam with a wavelength of 655 nm. The aspheric objective lens of the optical head with a numeric aperture (NA) of 0.6 has a focal length of 2.33 mm. However, the NA 0.6 objective has a working distance of only 1.28 mm, which may limit some measurement application. The working distance can be enlarged by replacing smaller NA objective lens. The NA 0.16 objective lens has a much longer working distance of 12 mm. The linear detection range of the NA 0.6 and NA 0.16 objective lens is $6\,\mu$m and $320\,\mu$m, respectively.

The full width at half-maximum (FWHM) D_w of the focal spot is given by

$$D_w = 0.52\frac{\lambda}{\text{NA}}. \tag{5}$$

The calculated D_w of NA 0.6 and NA 0.16 objective lenses are 568 nm and $2.13\,\mu$m (FWHM), respectively. The NA 0.6 objective lens with submicron laser spot is beneficial to detect deflections of submicrometer-sized cantilevers.

Additionally, the PDIC has a bandwidth of 80 MHz $(-3$ dB$)$ that is suitable to high-frequency detection. The S_{FE} calibration procedure can be done by giving cantilever a known vertical displacement directly. Overall, the ADS with NA 0.6 and NA 0.16 object lenses has a measurement sensitivity of 0.5 nm/mV and 50 nm/mV, respectively. Because of higher measurement resolution, most of the measurements in this paper are carried out by the ADS with NA 0.6 objective lens.

The preamplifier is used to amplify and transform the signals from the PDIC into the focus error signal S_{FE} which is then processed by a high-speed 14-Bit DAQ card (PCI-9820, ADLINK) with a sampling rate up to 130 MHz (ping-pong mode). Through the PCI bus, the digital data is analyzed by a program under a LabVIEW (National Instruments) platform. The acquired vibrational signal is processed by the fast Fourier transformation (FFT). Using the FFT algorithm, the acquired time domain signal is transformed into the frequency domain spectrum, which gives a clear overview of all resonant frequencies.

For improving the signal to noise ratio (SNR), microcantilevers are typically coated with high reflective materials like gold. However, the reflective layer may also cause binding of undesired molecules and might induce unwanted bimorph effects.

Furthermore, pure SU-8 surfaces can be employed for measuring thermodynamic properties of polymer thin films
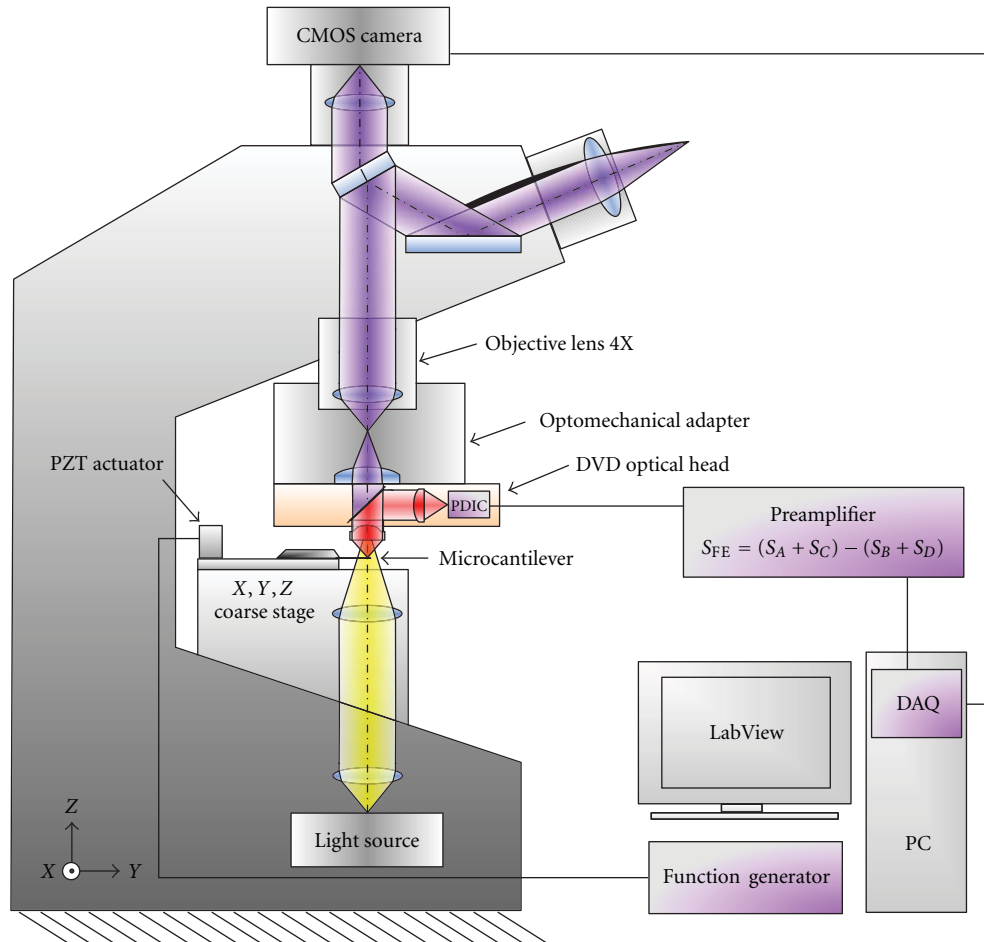
FIGURE 3: Block diagram of the ADS attached to an OM.

(a)   (b)
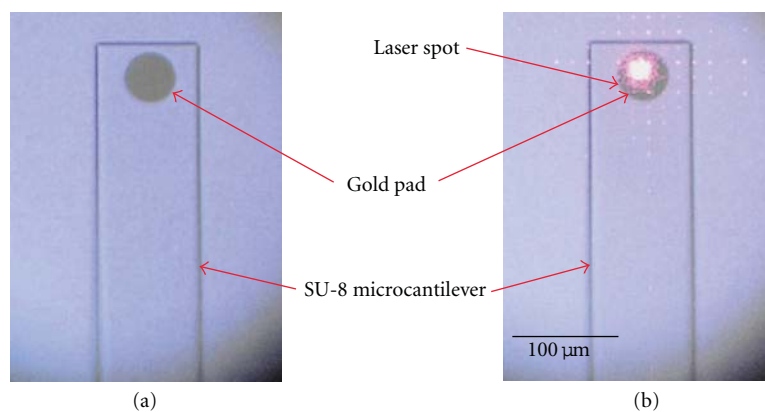
FIGURE 4: Microscopic images of (a) circular gold pad on SU-8 microcantilever and (b) focusing laser spot on gold pad.

deposed on the cantilevers surfaces [20]. Fast screening of the vibrational behavior of pure SU-8 microcantilevers would represent an extremely useful tool for the analysis of mechanical properties of polymeric material and for monitoring of degradation processes of biopolymers under various conditions [21].

The resonant frequencies of the microcantilevers are measured by the ADS in four conditions: with and without reflective coating; with and without external excitation. As expected, the SNR is strongly reduced when neither reflective pads nor external actuation is involved. The vibrational amplitude and the SNR of microcantilevers without reflective coatings can be significantly improved by the external excitation. In our experiments, a PZT actuator which is driven by a function generator is attached to a holder of the microcantilevers.

(a)

Original data
Fitting data

(b)

FIGURE 5: (a) Thermal noise spectrum and (b) SHO fitting curve for an SU-8 cantilever.

Spectrum without excitation
Spectrum with excitation
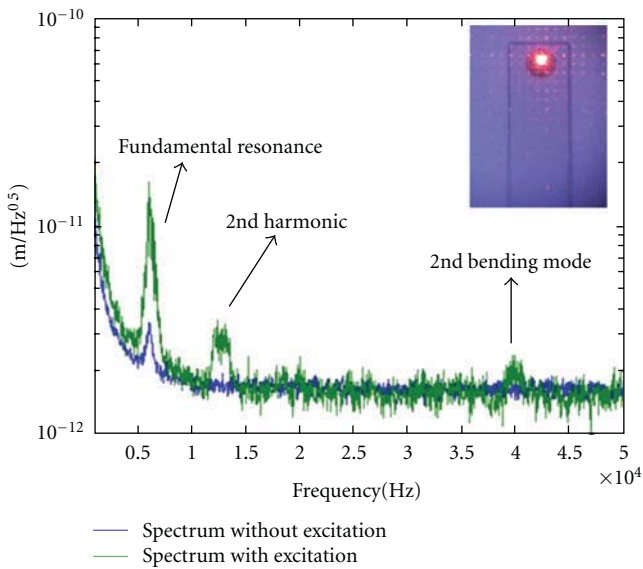
FIGURE 6: Thermal noise spectrum and excited spectrum by laser focused on gold pad.

Spectrum without excitation
Spectrum with excitation
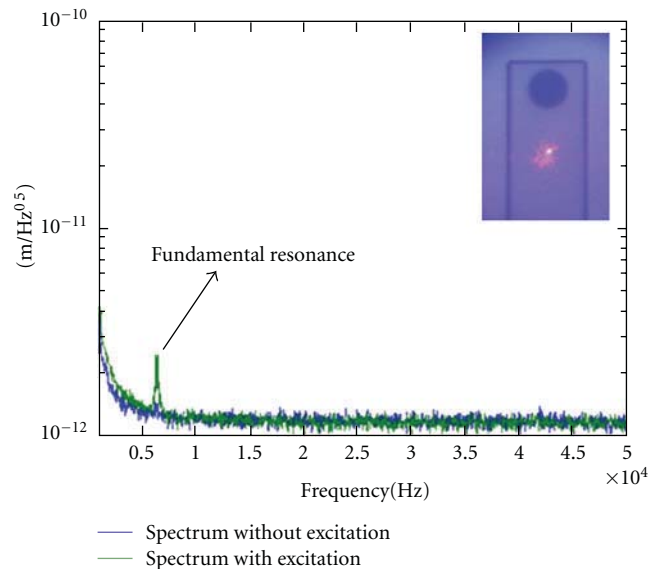
FIGURE 7: Thermal noise spectrum and excited spectrum by laser focused on the transparent part of the cantilever.

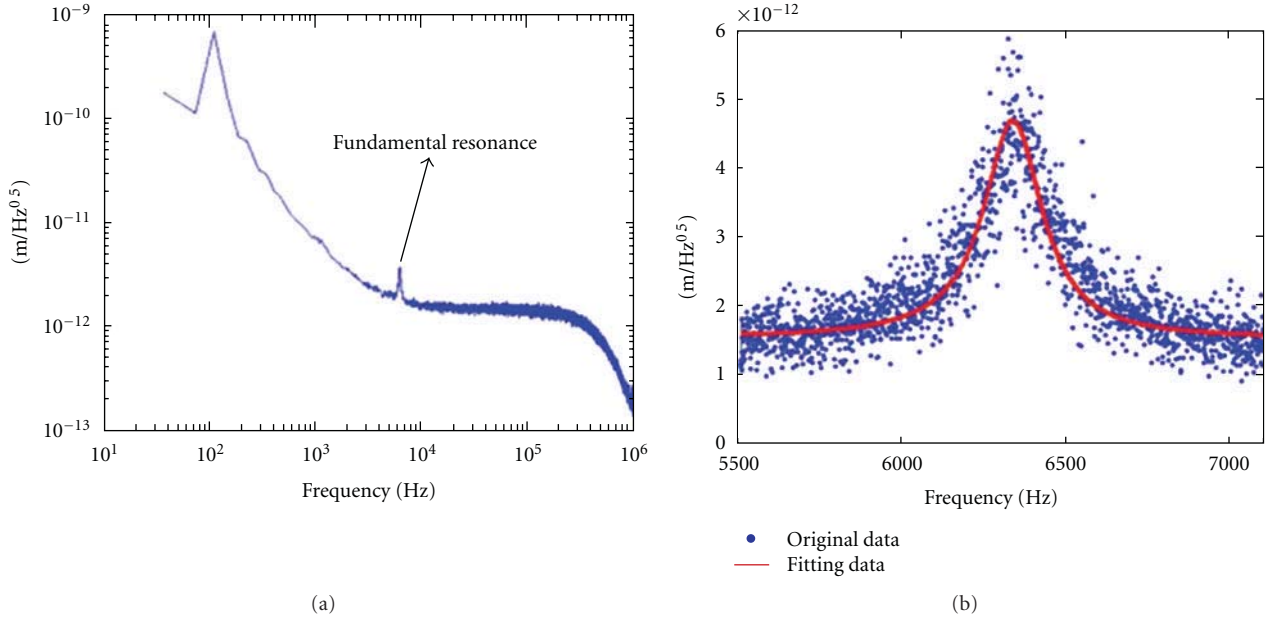Figure 4(a) shows an optical microscope image of the 20 nm thick circular gold pad on the free end of an SU-8 microcantilever. Through the X, Y, Z coarse stages of the OM, the laser beam is positioned and focused at the detected gold pad. And the focusing process can be simultaneously monitored as shown in Figure 4(b). The laser alignment can be adjusted with an x-y resolution of 100 nm.

4. Results and Discussion

Figure 5(a) shows the thermal noise spectrum and the fundamental resonant peak of the microcantilever. For measuring low resonance frequency cantilever, the bandwidth of the preamplifier we used is 1 MHz only, thus the measured signal decayed in the end. For precise identifying the resonant peak, the spectral data are fitted by the simple harmonic oscillator (SHO) function as shown in Figure 5(b). The measured resonant frequency 6.328 kHz is close to the calculated result range of 6.55 ± 0.4 kHz from (2) and the FEA simulated result of 6.59 ± 0.5 kHz. The difference may be attributed to damping effects, which are neglected in the simplified theoretical models. Furthermore, the values for Young's modulus and density of the polymer depend on the SU-8 microfabrication-processing [22, 23] conditions

FIGURE 8: Microscopic images of focusing laser spot on the gold pad by using long working distance ADS.

might be slightly different than the ones presented in Table 1.

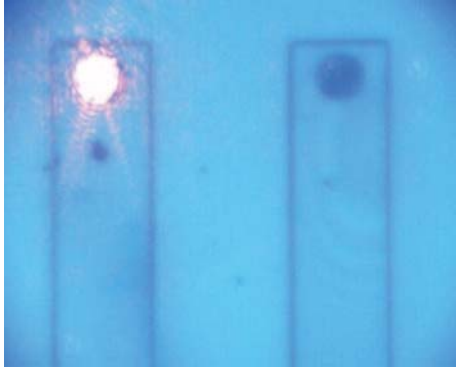For enhancing free response vibration amplitude of the microcantilever, a mechanical excitation generated by the PZT actuator is applied. Figure 6 shows a comparison of the thermal noise spectrum and the excited spectrum when the laser is focused on the gold pad of the microcantilever. Using the external excitation, the first resonant peak becomes 4 times higher than without excitation. Also, the second resonant peak at 40 kHz is intensified. The measured second resonant frequency is slightly smaller than the simulated value of 40.3 kHz. The 2nd harmonic is visible due to the external excitation and can be suppressed by decreasing the driving voltage of the PZT actuator.

Because of the low reflectivity of the SU-8 surface, the SNR of the S_{FE} is lower than that measured on the gold pad. Figure 7 shows the thermal noise spectrum and the spectrum with external excitation when the laser is focused next to the gold pad. The amplitude of the first resonant peaks is almost an order of magnitude lower than the one measured on the gold pad. The laser position is closer to the cantilever base compared to the previous measurements, but the decrease of vibration amplitude at this location is not significant enough to explain the decrease in signal strength. It is believed that the predominant contribution to the lower SNR of the S_{FE} and a lower Q factor compared to the measurements on the gold pads is given by the low reflectivity of the SU-8 cantilever surface.

Nevertheless, the results demonstrate that the vibrational behavior of a homogenous microcantilever can be easily detected by the ADS even without the reflective coating and in presence of additional factors contributing to a reduction of the SNR. It is thus shown that the ADS has high capabilities in successfully characterizing the elastic properties of these polymer structures. Figure 8 shows an optical microscopic image captured by the ADS with NA 0.1 objective lens.

5. Conclusions

The ADS is capable of measuring the resonance frequency of SU-8 microcantilevers with and without reflective coatings.

The measured results coincide well with corresponding calculations and simulations. The ADS integrated with the OM and the CMOS camera makes the cantilever alignment and laser focusing efficient. For low reflective cantilever surface, the external excitation can be used to intensify the SNR.

Compared with the optical lever technique, the ADS has more advantages for high-speed microcantilever deflection measurements, such as compact size, easy adjustment, and high angular tolerance. Furthermore, the ADS with different objective lens is suitable for submicrometer cantilevers and long distance measurement applications. In future work, the ADS will be used to measure surface acoustic waves (SAWs) [24], which are widely applied in wireless devices as well as in chemical/biological sensors.

References

[1] J. Fritz, "Cantilever biosensors," *Analyst*, vol. 133, no. 7, pp. 855–863, 2008.

[2] S. Singamaneni, M. C. LeMieux, H. P. Lang et al., "Bimaterial microcantilevers as a hybrid sensing platform," *Advanced Materials*, vol. 20, no. 4, pp. 653–680, 2008.

[3] P. S. Waggoner and H. G. Craighead, "Micro- and nanomechanical sensors for environmental, chemical, and biological detection," *Lab on a Chip*, vol. 7, no. 10, pp. 1238–1255, 2007.

[4] J. Fritz, M. K. Baller, H. P. Lang et al., "Translating biomolecular recognition into nanomechanics," *Science*, vol. 288, no. 5464, pp. 316–318, 2000.

[5] J. W. Ndieyira, M. Watari, A. D. Barrera et al., "Nanomechanical detection of antibiotic-mucopeptide binding in a model for superbug drug resistance," *Nature Nanotechnology*, vol. 3, no. 11, pp. 691–696, 2008.

[6] N. V. Lavrik, M. J. Sepaniak, and P. G. Datskos, "Cantilever transducers as a platform for chemical and biological sensors," *Review of Scientific Instruments*, vol. 75, no. 7, pp. 2229–2253, 2004.

[7] S. Alexander, L. Hellemans, O. Marti et al., "An atomic-resolution atomic-force microscope implemented using an optical lever," *Journal of Applied Physics*, vol. 65, no. 1, pp. 164–167, 1989.

[8] N. Blanc, J. Brugger, N. F. De Rooij, and U. Dürig, "Scanning force microscopy in the dynamic mode using microfabricated capacitive sensors," *Journal of Vacuum Science and Technology B*, vol. 14, no. 2, pp. 901–905, 1996.

[9] M. Tortonese, R. C. Barrett, and C. F. Quate, "Atomic resolution with an atomic force microscope using piezoresistive detection," *Applied Physics Letters*, vol. 62, no. 8, pp. 834–836, 1993.

[10] T. Itoh and T. Suga, "Development of a force sensor for atomic force microscopy using piezoelectric thin films," *Nanotechnology*, vol. 4, no. 4, article 007, pp. 218–224, 1993.

[11] P. A. Rasmussen, J. Thaysen, O. Hansen, S. C. Eriksen, and A. Boisen, "Optimised cantilever biosensor with piezoresistive read-out," *Ultramicroscopy*, vol. 97, no. 1–4, pp. 371–376, 2003.

[12] R. Raiteri, M. Grattarola, H. J. Butt, and P. Skládal, "Micromechanical cantilever-based biosensors," *Sensors and Actuators, B*, vol. 79, no. 2-3, pp. 115–126, 2001.

[13] M. Alvarez, A. Calle, J. Tamayo, L. M. Lechuga, A. Abad, and A. Montoya, "Development of nanomechanical biosensors for detection of the pesticide DDT," *Biosensors and Bioelectronics*, vol. 18, no. 5-6, pp. 649–653, 2003.

[14] E.-T. Hwu, S.-K. Hung, C.-W. Yang, I.-S. Hwang, and K.-Y. Huang, "Simultaneous detection of translational and angular displacements of micromachined elements," *Applied Physics Letters*, vol. 91, no. 22, Article ID 221908, 2007.

[15] M. Nordström, S. Keller, M. Lillemose et al., "SU-8 cantilevers for bio/chemical sensing; fabrication, characterisation and development of novel read-out methods," *Sensors*, vol. 8, no. 3, pp. 1595–1612, 2008.

[16] F. G. Bosco, E. T. Hwu, C. H. Chen et al., "High throughput label-free platform for statistical bio-molecular sensing," *Lab on a Chip*, vol. 11, no. 14, pp. 2411–2416, 2011.

[17] E.-T. Hwu, S.-K. Hung, C.-W. Yang, K.-Y. Huang, and I.-S. Hwang, "Real-time detection of linear and angular displacements with a modified DVD optical head," *Nanotechnology*, vol. 19, no. 11, Article ID 115501, 2008.

[18] G. A. Matei, E. J. Thoreson, J. R. Pratt, D. B. Newell, and N. A. Burnahm, "Precision and accuracy of thermal calibration of atomic force microscopy cantilevers," *Review of Scientific Instruments*, vol. 77, Article ID 083703, 6 pages, 2006.

[19] S. S. Keller, L. Gammelgaard, M. P. Jensen, S. Schmid, Z. J. Davis, and A. Boisen, "Deposition of biopolymer films on micromechanical sensors," *Microelectronic Engineering*, vol. 88, no. 8, pp. 2297–2299, 2011.

[20] N. Jung, H. Seo, D. Lee, C. Y. Ryu, and S. Jeon, "Nanomechanical thermal analysis of the glass transition of polystyrene using silicon cantilevers," *Macromolecules*, vol. 41, no. 19, pp. 6873–6875, 2008.

[21] K. Yamashita, Y. Kikkawa, K. Kurokawa, and Y. Doi, "Enzymatic degradation of poly(L-lactide) film by proteinase K: quartz crystal microbalance and atomic force microscopy study," *Biomacromolecules*, vol. 6, no. 2, pp. 850–857, 2005.

[22] R. Feng and R. J. Farris, "The characterization of thermal and elastic constants for an epoxy photoresist SU8 coating," *Journal of Materials Science*, vol. 37, no. 22, pp. 4793–4799, 2002.

[23] M. Hopcroft, T. Kramer, G. Kim et al., "Micromechanical testing of SU-8 cantilevers," *Fatigue and Fracture of Engineering Materials and Structures*, vol. 28, no. 8, pp. 735–742, 2005.

[24] K. Länge, G. Blaess, A. Voigt, R. Götzen, and M. Rapp, "Integration of a surface acoustic wave biosensor in a microfluidic polymer chip," *Biosensors and Bioelectronics*, vol. 22, no. 2, pp. 227–232, 2006.

Research Article

Quantitative, Label-Free Detection of the Aggregation of α-Synuclein Using Microcantilever Arrays Operated in a Liquid Environment

Jason Jensen,[1] Margherita Farina,[2] Giampaolo Zuccheri,[2] Wilfried Grange,[3] and Martin Hegner[1]

[1] *Centre for Research on Adaptive Nanostructures and Nanodevices (CRANN) and School of Physics, Trinity College Dublin, Dublin 2, Ireland*
[2] *Department of Biochemistry, University of Bologna, 40126 Bologna, Italy*
[3] *Institut Jacques Monod, CNRS, Université Paris Diderot, 75205 Paris Cedex 13, France*

Correspondence should be addressed to Jason Jensen, jensenja@tcd.ie and Martin Hegner, hegnerm@tcd.ie

Early detection of protein aggregation is of great importance in the field of neurodegenerative diseases. The successful detection of the aggregation of the protein α-synuclein in a quantitative, label-free manner by functionalising a microcantilever with α-synuclein monomers and operating it in dynamic mode in the presence of α-synuclein monomers in solution is reported. A total mass of 6 ng of α-synuclein was detected over 9 hours on the surface of the cantilever. The result is compared to conventional fluorescence measurements of α-synuclein aggregation under similar conditions. It is found that the label-free cantilever detection method requires a concentration of protein 50 times smaller than that of the current method and indicated potential for significantly faster response times.

1. Introduction

Parkinson's disease is a progressive, neurodegenerative disorder which was first described by James Parkinson in 1817 [1]. It is the second most common neurodegenerative disorder and affects 1-2% of the population over the age of 65 years [2]. Parkinson's disease has been associated with mutations of the gene encoding for, and the aggregation of, the protein α-synuclein which is highly expressed in the dopamine containing neurons in the *substantia nigra* [2–6].

The neuropathological feature of Parkinson's disease is the presence of cytoplasmic inclusions called Lewy bodies which are fibrillar aggregates of α-synuclein [7–9]. The amyloid fibrils are 200–600 nm long and 5–10 nm in diameter [2, 3, 6, 10]. α-Synuclein belongs to the group of natively unfolded proteins and contains 140 amino acid residues [11, 12]. Animal models indicate that the accumulation of α-synuclein may play a role in the loss of dopaminergic neurons during Parkinson's disease [13–15].

Thioflavin T is a fluorescent label for α-synuclein which undergoes a shift in emission frequency upon aggregation of the protein [16–18]. By monitoring, the intensity of the shifted emission frequency rates of aggregation of the protein can be determined [16]. However, this technique requires knowledge of the label-fibril binding stoichiometries which can be variable depending on solution conditions or type of protein being investigated. α-Synuclein aggregation rates determined using Thioflavin T show a strong dependence on solution conditions such as pH or salt concentration, with incubation times (at 37°C) for achieving half the final intensity being ∼80 hrs at pH 7 and as short as 70 minutes at pH 4 [16]. Typically large concentrations of the protein are also required to provide sufficient intensity for measurement. Also the presence of another molecule which interacts with the fibril can affect binding kinetics; therefore, label-free detection techniques which do not affect the kinetics are preferable [19].

Nanomechanical cantilever sensors have been widely applied in the field of biology due to their versatility and easy functionalisation with a broad range of chemical and biological molecules. These sensors can be operated in liquid [20] which allows detection of the target molecules and interactions in a physiological environment. Cantilever sensors have found applications in the fields of genomics [21–25], microbiology [26–30], detection of proteins [31], as immunosensors [32] and for the investigation of membrane protein-ligand interactions [33, 34].

Label-free detection of growth of insulin amyloid fibrils by measuring the deflection of a microcantilever has been reported [35]. However, this method only reported the tracking of deflection of the cantilever with time and the surface stress induced on the cantilever by the growth of the fibrils and as such is suitable for determining whether or not growth of the fibril is occurring and is not suitable for determining the kinetics of the interaction in a quantitative manner.

When operated in dynamic mode the cantilever is vibrated at one of its flexural resonance frequencies and acts as a fine microbalance which allows quantitative measurements to be conducted. The dynamics of microcantilevers operating in fluids are well documented in the literature both theoretically [36–43] and experimentally [38, 44, 45] due to the importance of understanding their behaviour for use with atomic force microscopes. Operation of the microcantilever in liquid for the entire experiment avoids any phase changes (e.g., liquid to air) which occur during other experiment designs, such as "dip and dry" measurements [46], which could cause damage to the protein being investigated. "Dip and dry" measurements can also lead to unwanted precipitation of the buffer salts onto the surface of the sensor. This precipitation can lead to additional mass on the surface which can convolute the signal measured by the sensor and lead to uncertainty in the interpretation of results. In order to increase mass sensitivity, high modes of vibration of the cantilever can be used to regain some of the sensitivity which is lost due to damping when operating the cantilever in liquid instead of air or vacuum [47].

Here measurements of aggregation of α-synuclein using the label Thioflavin T and fluorescence measurements are compared with label-free detection using microcantilevers.

2. Materials and Methods

2.1. Cantilever Measurements

2.1.1. Preparation of Cantilever Array. Microcantilevers can respond to virtually any stimulus as is shown by the wide range of sensing applications that they have been applied to. Therefore, careful preparation of the cantilever array is essential to create a sensor that is both sensitive to the mass change due to the aggregation on the surface and also specific to the desired interaction. The use of a reference in sensing applications involving cantilevers is essential if the correct deductions are to be taken from the recorded response of the cantilevers. The cantilevers used in these experiments were Si cantilever arrays (Orientation: 110) with eight cantilevers per

array (IBM Research Laboratory, Rüschlikon, Switzerland). The cantilevers had a pitch of $250\,\mu m$ and were $500\,\mu m$ long, $100\,\mu m$ wide, and $1\,\mu m$ thick (with a 10 nm tolerance of the thickness within an array). The use of an array of cantilevers allows the inclusion of multiple tests and *in situ* references in one experiment. This greatly increases throughput and ensures that unwanted responses of the test cantilevers can be taken into account.

2.1.2. Cleaning. Unless otherwise stated all chemicals are from Sigma-Aldrich (Arklow, Ireland). The cantilever array was cleaned using the following protocol. A precleaning step in 2% RBS detergent solution (Fluka) for 2 minutes was followed by a rinse in 1 M NaCl and a rinse in 18 MΩ nanopure water (30 seconds each). The array was then placed in piranha solution (1 : 1 ratio of $H_2SO_4 : H_2O_2$) for 30 seconds followed by rinses in 1 M NaCl, EtOH and 18 MΩ nanopure water mix (1 : 1 ratio), and 18 MΩ nanopure water for 30 seconds each. The array was then placed in piranha baths for 20 and 10 minute periods with the same rinse procedure as before following each bath. The cantilever array was then placed in an isopropanol bath for 2 minutes before being stored in vacuum until needed.

2.1.3. Ti/Au Coating and Functionalisation. The cantilever array was coated in a monolayer of PEG silane by immersing the array in a solution of $4900\,\mu L$ EtOH, $50\,\mu L$ Hunig's base(N-ethyldiisopropylamine), and $50\,\mu L$ [hydroxy(polyethyleneoxy)propyl]triethoxysilane (8–12 EO) 50% in EtOH (ABCR GmbH & Co., 76187 Karlsruhe, Germany) for 2 hours on a linear shaker at 120 RPM.

The cantilever array was then coated on the top side with a 2 nm Ti adhesion layer followed by a 20 nm Au layer (Birmingham Metals Ltd., Birmingham, B9 4BN, UK). The metal coating was carried out by e-beam evaporation for the Ti and thermal evaporation for the Au (Edwards Auto 500, BOC Edwards, West Sussex, RH10 9LW, UK). The settings used were Ti: pressure 4.3×10^{-7} Torr, 46 mA current, with a deposition rate of 0.4 Å/s; Au: pressure 5.4×10^{-7} Torr, 12 mA current with a deposition rate of 1.5 Å/s. The cantilever array was stored in vacuum until needed for functionalisation.

The cantilever array was functionalised using a custom fabricated capillary functionalisation setup [48]. The capillaries had an outer diameter of $250\,\mu m$ and an inner diameter of $180\,\mu m$ (King Precision Glass Inc, Calif, USA). The cantilevers were inserted into the end of the capillaries, and the capillaries were then back filled with the solution for functionalisation. The test cantilevers were first coated with a monolayer of DSU (dithobis(succinimidyl undecanoate), NBS Biologicals) [49] by immersion in a solution of 0.5 mM DSU in dioxane 1,4 for 30 minutes. The DSU binds to the gold via a thiol group at one end. The reference cantilevers were passivated against protein binding using a hydroxyl-terminated monolayer. The layer was formed by immersing the cantilevers in a solution of 0.5 mM 11-mercapto-1-undecanol in EtOH for 30 minutes. The array was then rinsed in dioxane 1,4 for 5 minutes followed by EtOH for 3 minutes. The test cantilevers were then further functionalised

with wild type α-synuclein protein (r-Peptide, Bogart, Ga, USA), which binds to the DSU, by immersion in 5 μg/mL α-synuclein in sodium phosphate buffer (20 mM, pH 7) for 2 hours. This was followed by a rinse in the same buffer for 5 minutes. Any remaining binding sites on the cantilever array were blocked using BSA (bovine serum albumin) at a concentration of 0.1 mg/mL in phosphate buffer (20 mM, pH 7.0). The BSA solution was sonicated and filtered through a 0.2 μm filter to remove any aggregates prior to immersion of the cantilever array in the solution. A final schematic of the functionalised test and reference cantilevers is shown in Figure 1.

2.1.4. Dynamic Mode Device. The cantilevers are clamped on top of a piezo electric actuator (EBL Products Inc., East Hartford, Conn, USA) inside the fluidic chamber. The cantilevers were excited at various flexural vibrating modes by a linear frequency sweep of a sinusoidal signal which is provided by a frequency generator (NI PCI 5406, National Instruments, Tex, USA) which is controlled by a LabVIEW interface.

As shown in Figure 2, optical beam deflection was used to detect the resonance frequency of the cantilever vibrations. A laser beam (633 nm, Free space power >2.4 mW, SWL 7504-P, Newport, Calif, USA) attenuated by a neutral density filter (OD 1.3 NE513B; Thorlabs Cambridgeshire, CB7 4EX, UK) was deflected from the tip of the cantilever onto a linear position sensitive detector (PSD, Sitek, Partille, Sweden). The output from the PSD is amplified (SR560 Low-Noise Preamplifier, Stanford Research Systems, Calif, USA) and digitised (NI PCI 5112, National Instruments, Tex, USA) before being analysed with the output from the frequency generator in a LabVIEW program resulting in a frequency spectrum. An automated translation stage (M110.1DG, Physik Instrumente, Bedford, MK43 0AN, UK) controlled by the LabVIEW program was used to move the laser and allow sequential readout from each of the cantilevers in the array.

The entire device is housed inside a box which is kept at a constant temperature of 23 ± 0.1°C to avoid any drifts in the measurement due to temperature changes. The temperature is kept constant by a fuzzy logic controller which is implemented using LabVIEW.

Fluid was pumped through the fluidic chamber using a syringe pump (Kent Scientific Corporation, Conn, USA). A 1.8 mL injection loop was used to inject target molecules without breaking the flow through the chamber.

2.1.5. Measurement. The array was loaded into the dynamic mode fluidic chamber and clamped on top of the piezo actuator. Sodium phosphate buffer (20 mM, pH 6.0) was passed through the chamber at a rate of 3.3 μL/min for four hours to allow the α-synuclein on the surface of the cantilevers to equilibrate to the lower pH and also to establish a baseline from which the shift of resonance frequency could be measured.

α-Synuclein lyophilised in Tris was resuspended in 18 MΩ nanopure water to a final concentration of 1 mg/mL α-synuclein in 10 mM Tris, pH 7.4. The α-synuclein was
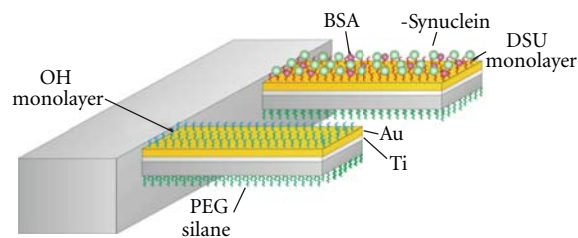

Figure 1: Schematic showing the functionalisation of the cantilever array. The backside of the cantilever is coated with a PEG silane monolayer to prevent nonspecific adsorption of α-synuclein during the experiment. The array is coated with a Ti/Au layer to facilitate functionalisation using thiol chemistry. The reference cantilever is coated with a self-assembled OH monolayer. The test cantilever is coated with α-synuclein bound to a DSU monolayer. All remaining binding sites are blocked with BSA.

rebuffered in 20 mM sodium phosphate buffer, pH 6, using a protein desalting spin column (Pierce Protein Research Products, Fisher Scientific Ireland, Dublin, Ireland). The solution was then diluted down to a final concentration of 10 μg/mL in the same buffer.

The α-synuclein monomers were passed through the fluidic chamber at a rate of 3.3 μL/min. In total, 1.8 mL of the monomer solution was passed over the array. Following the injection of the monomer solution, phosphate buffer was passed through the chamber to check for any unbinding of protein from the surface of the cantilever.

2.1.6. Data Handling. The 14th flexural resonance mode of the cantilever (~640 kHz) was tracked during the experiment. The frequency range of each scan was 200 kHz, with 2000 steps in the range giving a frequency resolution of 100 Hz. Each frequency in the range was excited for 1 ms, and the response from the PSD was sampled at a rate of 10^6 samples per second. The RMS value of the differential signal from the PSD was then calculated for each of the frequencies in the spectrum. The resonance mode was measured every 30 seconds for each cantilever in the array. The bound mass on the surface of the cantilevers was then extracted from the frequency spectra by postprocessing of the data using NOSEtools software [50–52].

2.2. Fluorescence Measurements. The aggregation of the protein α-synuclein in solution was also measured using fluorescence measurements as a further control to be compared with the cantilever array measurement. The fluorescent marker Thioflavin T was used to indicate aggregation of the α-synuclein in solution.

2.2.1. Preparation of α-Synuclein. The α-synuclein lyophilised in Tris was resuspended in 18 MΩ nanopure water to a final concentration of 1 mg/mL α-synuclein in 10 mM Tris, pH 7.4. The protein was resuspended in 10 mM sodium phosphate buffer, pH 7.4, using a dialysis membrane (Slide-A-Lyzer Dialysis Cassette 3,500 MWCO, Pierce Protein Research Products, Fisher Scientific Ireland, Dublin,
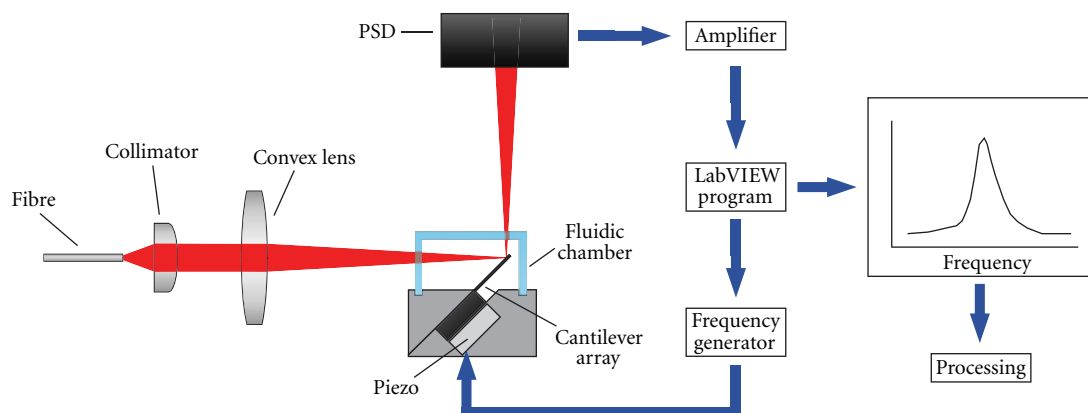
FIGURE 2: Schematic of the experimental device and measurement procedure. A LabVIEW program controls a frequency generator which sends a sinusoidal frequency signal to the piezo actuator. The cantilever is swept through a range of frequencies, and the response of the cantilever is detected using optical beam deflection. The signal from the PSD is then amplified before being processed by the LabVIEW program to create a frequency spectrum. The peaks of the frequency spectrum correspond to the flexural resonance modes of the cantilever. The frequency spectra generated during the experiment are then processed to give a frequency versus time plot, and hence the change in bound mass versus time can be determined.

Ireland). The 1 mL of protein in Tris solution was injected into the membrane and placed in 800 mL of the sodium phosphate buffer for 30 hours and stored at 4°C. The sodium phosphate buffer was replaced three times during the procedure.

2.2.2. Fluorescence Measurements. A 96-well microtiter plate (Sterilin Ltd., Newport, NP11 3EF, UK) was prepared with wells containing $30 \mu L$ of 10 mM sodium phosphate buffer (pH 7.4), $10 \mu L$ of 500 mM NaCl in 10 mM buffer, $50 \mu L$ of α-synuclein 1 mg/mL in 10 mM buffer and $10 \mu L$ of $100 \mu M$ Thioflavin-T in 10 mM buffer for a final volume of $100 \mu L$ in each well. Reference wells for Thioflavin T and blank measurements were also prepared. The reference well for Thioflavin T contained $80 \mu L$ of 10 mM buffer, $10 \mu L$ of 500 mM NaCl in 10 mM buffer and $10 \mu L$ of $100 \mu M$ Thioflavin-T in 10 mM buffer. The blank reference wells contained $90 \mu L$ of 10 mM buffer, and $10 \mu L$ of 500 mM NaCl in 10 mM buffer. Two wells of each of the above were prepared at three time intervals 8 hrs apart to facilitate measurements of the aggregation at equally spaced time intervals.

The plates were incubated at 37°C while shaking continuously at 150 RPM, with a diameter of 20 mm. The plates were removed from the incubator for intensity measurements every 2.5 hours. The plates were covered at all times to avoid photo bleaching of the Thioflavin T. The fluorescence measurements were carried out in a FLUOstar Optima microplate multidetection reader (BMG Labtech, Aylesbury, HP20 2QJ, UK) with excitation at 450 nm and emission intensity recorded at 520 nm.

3. Results and Discussion

3.1. Cantilever Measurements. The frequency spectra resulting from the cantilever measurements were postprocessed using NOSEtools software to determine the shift of the flexural resonance peak and hence the change in mass on the surface of the cantilever (Figure 3). The reference cantilever demonstrated a small decrease in frequency during the experiment (data not shown). The response from the reference cantilever was subtracted from that of the test cantilever to account for any nonspecific adsorption of protein to the either side (PEG back side or OH terminated top side) of the cantilever and to account for any drifts in the response. The only sites available for the α-synuclein monomers in solution to bind to the surface of the cantilever was by aggregating and starting its polymerisation with the protein already attached to the DSU monolayer on the surface. Approximately, 6 ng of protein was aggregated on the surface of the cantilever over a 9-hour period. Following the injection of monomers buffer was passed through the chamber and a small amount of α-synuclein was removed from the surface (~ 1 ng).

Images of the top side of the test and reference cantilevers following the experiment indicate that more protein was bound to the surface of the test cantilever than the reference (data not shown) and support the frequency measurements that indicate that there was a small amount of nonspecific binding of the α-synuclein to the reference cantilever. This highlights the importance of the *in situ* reference when conducting experiments of this kind. The subtraction of the response of the reference cantilever from that of the test cantilever allows any nonspecific binding of the protein to be subtracted from the measurement so that only the response from the protein-protein interactions are examined.

3.2. Fluorescence Measurements. The intensity of the emission from $10 \mu M$ Thioflavin T with 0.5 mg/mL α-synuclein at 520 nm was recorded for 23 hours. The intensities recorded for the fluorescence measurements were scaled by the intensity from the blank wells in order to account for changes
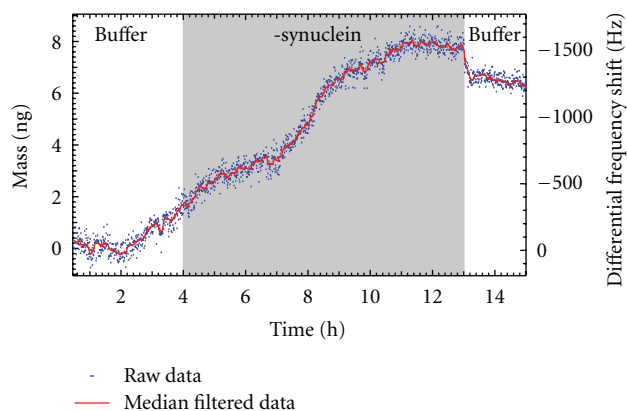
FIGURE 3: Graph of bound mass on the surface of the cantilever versus time. The frequency spectra recorded during the experiment were postprocessed using NOSEtools software to obtain the resulting plot of bound mass versus time. The scatter plot shows the raw data (with the reference cantilever subtracted), and the line shows the median box filter of the raw data (box size 23). The left axis shows the bound mass on the surface of the cantilever, and the right axis shows the corresponding differential frequency shift. The grey area indicates the period that $10\,\mu g/mL$ α-synuclein in 20 mM sodium phosphate buffer was flowing through the fluidic chamber at a rate of $3.3\,\mu L/min$.

FIGURE 4: Scaled Intensity versus time for thioflavin T intensity measurements. The intensity of the emission from $10\,\mu M$ Thioflavin T with 0.5 mg/mL α-synuclein at 520 nm was recorded for 23 hours. The intensity was scaled by the blank measurement, and the Thioflavin T reference was subtracted from the test intensity measurement. The data shown is the average of the intensity from the two wells.

in the input power of the laser in the microplate reader. The intensity from the reference wells was then subtracted from the test wells to show the change in intensity due to the aggregation of the α-synuclein. The experiment was carried out in duplicate, and the data from each time point was averaged (Figure 4). The error bars correspond to the result of the propagation of the standard error of the mean of the intensities through the analysis outlined above. After an initial lag phase of 7 hours, there is a steady increase of the average intensity recorded. This indicates that there is aggregation of the α-synuclein during this time.

3.3. Discussion. These experiments show that it is possible to detect the aggregation of the protein α-synuclein in a label-free manner using functionalised microcantilevers operating in dynamic mode in a physiological liquid environment. The concentration of protein required to detect the aggregation using the label-free method is a factor 50 smaller than that used for the fluorescent method presented here. The total mass of protein required was also smaller despite the continuous flow method used for the cantilever measurements, with $50\,\mu g$ of protein being required per test well, while only $18\,\mu g$ of protein was passed through the cantilever fluidic chamber. In addition, no lag phase was observed during the cantilever measurements, whereas there was a seven hour lag phase observed in the fluorescence measurements.

The aggregation of the α-synuclein on the surface of the cantilever was reproducible; however, the total mass of protein aggregated was heavily dependent on the conformation and density of the initial seeded monomers on the surface of the cantilever (data not shown).

It should be noted that approximately 6 ng of the protein that was passed through the fluidic chamber was polymerised
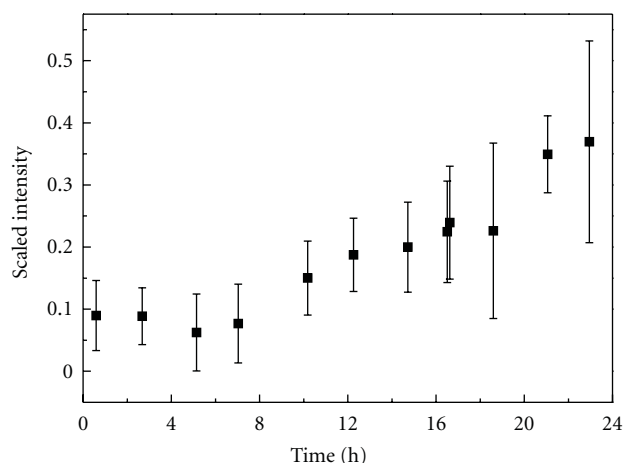
on the surface indicating that the continuous flow method is very wasteful. Employing a method where a smaller amount of α-synuclein is used and the flow is stopped when the protein is in the fluidic chamber (which has a volume of $\sim 6\,\mu L$), a more efficient detection of the aggregation could be possible. However, if the aim is to determine the binding kinetics of the aggregation then such a stop flow situation could lead to incorrect conclusions as the rate that is obtained can heavily depend on the diffusion rate of the protein towards the surface of the cantilever within the fluidic chamber.

The sensitivity of a microcantilever for mass sensing allows detection of a very small mass of protein from the liquid flowed through the chamber (the current sensitivity of our device lies in the subnanogram regime in liquids). This can be advantageous when working with particularly expensive molecules or when the aim of the experiment is to detect molecules which are in very low concentrations in a natural, physiological environment.

The method and results presented here show a quantitative measurement of aggregation of the protein α-synuclein on the surface of a microcantilever with an *in situ* reference in a physiological environment. This represents an improvement over other measurements of protein aggregation using microcantilevers reported in the literature [35]. As discussed in the Introduction, the static method is not suitable for determining the kinetics of the aggregation process. Further work will focus on determining the aggregation rates on the surface of the cantilever for a range of solution conditions and protein concentrations.

Acknowledgements

References

[1] J. Parkinson, "An essay on the shaking palsy (reprinted)," *The Journal of Neuropsychiatry and Clinical Neurosciences*, vol. 14, no. 2, pp. 223–222, 2002.

[2] M. Goedert, "α-synuclein and neurodegenerative diseases," *Nature Reviews Neuroscience*, vol. 2, no. 7, pp. 492–501, 2001.

[3] J. Lotharius and P. Brundin, "Pathogenesis of Parkinson's disease: dopamine, vesicles and α-synuclein," *Nature Reviews Neuroscience*, vol. 3, no. 12, pp. 932–942, 2002.

[4] L. I. Golbe, G. Di Iorio, V. Bonavita, D. C. Miller, and R. C. Duvoisin, "A large kindred with autosomal dominant Parkinson's disease," *Annals of Neurology*, vol. 27, no. 3, pp. 276–282, 1990.

[5] R. Krüger, W. Kuhn, T. Müller et al., "Ala30Pro mutation in the gene encoding α-synuclein in Parkinson's disease," *Nature Genetics*, vol. 18, no. 2, pp. 106–108, 1998.

[6] K. Wakabayashi, K. Tanji, F. Mori, and H. Takahashi, "The Lewy body in Parkinson's disease: molecules implicated in the formation and degradation of α-synuclein aggregates," *Neuropathology*, vol. 27, no. 5, pp. 494–506, 2007.

[7] M. G. Spillantini, M. L. Schmidt, V. M. Y. Lee, J. Q. Trojanowski, R. Jakes, and M. Goedert, "α-synuclein in Lewy bodies," *Nature*, vol. 388, no. 6645, pp. 839–840, 1997.

[8] M. G. Spillantini, R. A. Crowther, R. Jakes, M. Hasegawa, and M. Goedert, "α-synuclein in filamentous inclusions of Lewy bodies from Parkinson's disease and dementia with Lewy bodies," *Proceedings of the National Academy of Sciences of the United States of America*, vol. 95, no. 11, pp. 6469–6473, 1998.

[9] M. Baba, S. Nakajo, P. H. Tu et al., "Aggregation of α-synuclein in Lewy bodies of sporadic Parkinson's disease and dementia with Lewy bodies," *American Journal of Pathology*, vol. 152, no. 4, pp. 879–884, 1998.

[10] R. A. Crowther, S. E. Daniel, and M. Goedert, "Characterisation of isolated α-synuclein filaments from substantia nigra of Parkinson's disease brain," *Neuroscience Letters*, vol. 292, no. 2, pp. 128–130, 2000.

[11] P. H. Weinreb, W. Zhen, A. W. Poon, K. A. Conway, and P. T. Lansbury, "NACP, a protein implicated in Alzheimer's disease and learning, is natively unfolded," *Biochemistry*, vol. 35, no. 43, pp. 13709–13715, 1996.

[12] D. Eliezer, E. Kutluay, R. Bussell, and G. Browne, "Conformational properties of α-synuclein in its free and lipid-associated states," *Journal of Molecular Biology*, vol. 307, no. 4, pp. 1061–1073, 2001.

[13] E. Masliah, E. Rockenstein, I. Veinbergs et al., "Dopaminergic loss and inclusion body formation in α-synuclein mice: implications for neurodegenerative disorders," *Science*, vol. 287, no. 5456, pp. 1265–1269, 2000.

[14] E. Maries, B. Dass, T. J. Collier, J. H. Kordower, and K. Steece-Collier, "The role of α-synuclein in Parkinson's disease: insights from animal models," *Nature Reviews Neuroscience*, vol. 4, no. 9, pp. 727–738, 2003.

[15] M. B. Feany and W. W. Bender, "A Drosophila model of Parkinson's disease," *Nature*, vol. 404, no. 6776, pp. 394–398, 2000.

[16] W. Hoyer, T. Antony, D. Cherny, G. Heim, T. M. Jovin, and V. Subramaniam, "Dependence of α-synuclein aggregate morphology on solution conditions," *Journal of Molecular Biology*, vol. 322, no. 2, pp. 383–393, 2002.

[17] H. Naiki, K. Higuchi, M. Hosokawa, and T. Takeda, "Fluorometric determination of amyloid fibrils in vitro using the fluorescent dye, thioflavine T," *Analytical Biochemistry*, vol. 177, no. 2, pp. 244–249, 1989.

[18] H. LeVine, "Quantification of β-sheet amyloid fibril structures with thioflavin T," *Methods in Enzymology*, vol. 309, pp. 274–284, 1999.

[19] R. Demaimay, J. Harper, H. Gordon, D. Weaver, B. Chesebro, and B. Caughey, "Structural aspects of congo red as an inhibitor of protease-resistant prion protein formation," *Journal of Neurochemistry*, vol. 71, no. 6, pp. 2534–2541, 1998.

[20] M. K. Ghatkesar, T. Braun, V. Barwich et al., "Resonating modes of vibrating microcantilevers in liquid," *Applied Physics Letters*, vol. 92, no. 4, Article ID 043106, 2008.

[21] R. McKendry, J. Zhang, Y. Arntz et al., "Multiple label-free biodetection and quantitative DNA-binding assays on a nanomechanical cantilever array," *Proceedings of the National Academy of Sciences of the United States of America*, vol. 99, no. 15, pp. 9783–9788, 2002.

[22] F. Huber, M. Hegner, C. Gerber, H. J. Güntherodt, and H. P. Lang, "Label free analysis of transcription factors using microcantilever arrays," *Biosensors and Bioelectronics*, vol. 21, no. 8, pp. 1599–1605, 2006.

[23] L. M. Lechuga, J. Tamayo, M. Álvarez et al., "A highly sensitive microsystem based on nanomechanical biosensors for genomics applications," *Sensors and Actuators B*, vol. 118, no. 1-2, pp. 2–10, 2006.

[24] J. Mertens, C. Rogero, M. Calleja et al., "Label-free detection of DNA hybridization based on hydration-induced tension in nucleic acid films," *Nature Nanotechnology*, vol. 3, no. 5, pp. 301–307, 2008.

[25] D. Ramos, M. Arroyo-Hernández, E. Gil-Santos et al., "Arrays of dual nanomechanical resonators for selective biological detection," *Analytical Chemistry*, vol. 81, no. 6, pp. 2274–2279, 2009.

[26] B. Ilic, Y. Yang, and H. G. Craighead, "Virus detection using nanoelectromechanical devices," *Applied Physics Letters*, vol. 85, no. 13, pp. 2604–2606, 2004.

[27] N. Nugaeva, K. Y. Gfeller, N. Backmann, H. P. Lang, M. Düggelin, and M. Hegner, "Micromechanical cantilever array sensors for selective fungal immobilization and fast growth detection," *Biosensors and Bioelectronics*, vol. 21, no. 6, pp. 849–856, 2005.

[28] K. Y. Gfeller, N. Nugaeva, and M. Hegner, "Rapid biosensor for detection of antibiotic-selective growth of *Escherichia coli*," *Applied and Environmental Microbiology*, vol. 71, no. 5, pp. 2626–2631, 2005.

[29] K. Y. Gfeller, N. Nugaeva, and M. Hegner, "Micromechanical oscillators as rapid biosensor for the detection of active growth of *Escherichia coli*," *Biosensors and Bioelectronics*, vol. 21, no. 3, pp. 528–533, 2005.

[30] D. Ramos, J. Tamayo, J. Mertens, M. Calleja, L. G. Villanueva, and A. Zaballos, "Detection of bacteria based on the thermomechanical noise of a nanomechanical resonator: origin of the response and detection limits," *Nanotechnology*, vol. 19, no. 3, Article ID 035503, 2008.

[31] P. S. Waggoner, M. Varshney, and H. G. Craighead, "Detection of prostate specific antigen with nanomechanical resonators," *Lab on a Chip*, vol. 9, no. 21, pp. 3095–3099, 2009.

[32] N. Backmann, C. Zahnd, F. Huber et al., "A label-free immunosensor array using single-chain antibody fragments,"

Proceedings of the National Academy of Sciences of the United States of America, vol. 102, no. 41, pp. 14587–14592, 2005.

[33] T. Braun, M. K. Ghatkesar, N. Backmann et al., "Quantitative time-resolved measurement of membrane protein-ligand interactions using microcantilever array sensors," *Nature Nanotechnology*, vol. 4, no. 3, pp. 179–185, 2009.

[34] T. Braun, N. Backmann, M. Vögtli et al., "Conformational change of bacteriorhodopsin quantitatively monitored by microcantilever sensors," *Biophysical Journal*, vol. 90, no. 8, pp. 2970–2977, 2006.

[35] T. P. J. Knowles, W. Shu, F. Huber et al., "Label-free detection of amyloid growth with microcantilever sensors," *Nanotechnology*, vol. 19, no. 38, Article ID 384007, 2008.

[36] F. J. Elmer and M. Dreier, "Eigenfrequencies of a rectangular atomic force microscope cantilever in a medium," *Journal of Applied Physics*, vol. 81, no. 12, pp. 7709–7714, 1997.

[37] J. E. Sader, "Frequency response of cantilever beams immersed in viscous fluids with applications to the atomic force microscope," *Journal of Applied Physics*, vol. 84, no. 1, pp. 64–76, 1998.

[38] T. Braun, V. Barwich, M. K. Ghatkesar et al., "Micromechanical mass sensors for biomolecular detection in a physiological environment," *Physical Review E*, vol. 72, no. 3, Article ID 031907, 9 pages, 2005.

[39] C. A. Van Eysden and J. E. Sader, "Resonant frequencies of a rectangular cantilever beam immersed in a fluid," *Journal of Applied Physics*, vol. 100, no. 11, Article ID 114916, 2006.

[40] C. A. Van Eysden and J. E. Sader, "Small amplitude oscillations of a flexible thin blade in a viscous fluid: exact analytical solution," *Physics of Fluids*, vol. 18, no. 12, Article ID 123102, 2006.

[41] C. A. Van Eysden and J. E. Sader, "Frequency response of cantilever beams immersed in viscous fluids with applications to the atomic force microscope: arbitrary mode order," *Journal of Applied Physics*, vol. 101, no. 4, Article ID 044908, 2007.

[42] C. A. Van Eysden and J. E. Sader, "Frequency response of cantilever beams immersed in compressible fluids with applications to the atomic force microscope," *Journal of Applied Physics*, vol. 106, no. 9, Article ID 094904, 2009.

[43] C. A. Van Eysden and J. E. Sader, "Compressible viscous flows generated by oscillating flexible cylinders," *Physics of Fluids*, vol. 21, no. 1, Article ID 013104, 2009.

[44] M. K. Ghatkesar, E. Rakhmatullina, H. P. Lang, C. Gerber, M. Hegner, and T. Braun, "Multi-parameter microcantilever sensor for comprehensive characterization of Newtonian fluids," *Sensors and Actuators B*, vol. 135, no. 1, pp. 133–138, 2008.

[45] S. Kim and K. D. Kihm, "Experimental verification of the temperature effects on Sader's model for multilayered cantilevers immersed in an aqueous medium," *Applied Physics Letters*, vol. 89, no. 6, Article ID 061918, 2006.

[46] L. Nicu, M. Guirardel, F. Chambosse et al., "Resonating piezoelectric membranes for microelectromechanically based bioassay: detection of streptavidin-gold nanoparticles interaction with biotinylated DNA," *Sensors and Actuators B*, vol. 110, no. 1, pp. 125–136, 2005.

[47] M. K. Ghatkesar, V. Barwich, T. Braun et al., "Higher modes of vibration increase mass sensitivity in nanomechanical microcantilevers," *Nanotechnology*, vol. 18, no. 44, Article ID 445502, 2007.

[48] A. Bietsch, J. Zhang, M. Hegner, H. P. Lang, and C. Gerber, "Rapid functionalization of cantilever array sensors by inkjet printing," *Nanotechnology*, vol. 15, no. 8, pp. 873–880, 2004.

[49] P. Wagner, M. Hegner, P. Kernen, F. Zaugg, and G. Semenza, "Covalent immobilization of native biomolecules onto Au(111) via N-hydroxysuccinimide ester functionalized self-assembled monolayers for scanning probe microscopy," *Biophysical Journal*, vol. 70, no. 5, pp. 2052–2066, 1996.

[50] T. Braun, M. K. Ghatkesar, V. Barwich et al., "Digital processing of multi-mode nano-mechanical cantilever data," *Journal of Physics*, vol. 61, no. 1, pp. 341–345, 2007.

[51] T. Braun, *NOSEtools Software Homepage*, http://web.me.com/brunobraun/NOSEtools/Home.html.

[52] T. Braun, F. Huber, M. K. Ghatkesar et al., "Processing of kinetic microarray signals," *Sensors and Actuators B*, vol. 128, no. 1, pp. 75–82, 2007.

Research Article

Rapid and Reliable Calibration of Laser Beam Deflection System for Microcantilever-Based Sensor Setups

Rohit Mishra,[1] Wilfried Grange,[2] and Martin Hegner[1]

[1] *Centre for Research on Adaptive Nanostructures and Nanodevices and School of Physics, Trinity College Dublin, Dublin 2, Ireland*
[2] *Institut Jacques Monod, CNRS, Université Paris Diderot, 75205 Paris Cedex 13, France*

Correspondence should be addressed to Rohit Mishra, mishrar@tcd.ie and Martin Hegner, hegnerm@tcd.ie

Cantilever array-based sensor devices widely utilise the laser-based optical deflection method for measuring static cantilever deflections mostly with home-built devices with individual geometries. In contrast to scanning probe microscopes, cantilever array devices have no additional positioning device like a piezo stage. As the cantilevers are used in more and more sensitive measurements, it is important to have a simple, rapid, and reliable calibration relating the deflection of the cantilever to the change in position measured by the position-sensitive detector. We present here a simple method for calibrating such systems utilising commercially available AFM cantilevers and the equipartition theorem.

1. Introduction

Cantilever-based sensor devices have extensively developed from the atomic force microscope (AFM) operating in the static mode [1–3] (surface stress based; qualitative method) and the dynamic mode [4–6] (frequency based; quantitative method) depending on the application. The most frequently used method of signal transduction where cantilevers are employed is change in surface stress being converted into mechanical signal through cantilever bending [7]. This deflection is an indication of the chemical [8], physical [9], or biophysical [10] process that occurs on the cantilever interface.

The laser beam-based deflection system [11] has been used most widely to measure the cantilever bending in the static mode because of the ease of use, robustness of the read-out technique, and availability of high-sensitivity position-sensitive detectors (PSDs) which allow subangstrom resolution [12, 13]. Subsequently, several studies have been made to determine the limitations of this technique along with its resolution and sensitivity [14–17]. One also comes across various techniques for determining the relation between the cantilever bending and the change in spot position observed by the PSD [18–21]. The simple geometric calculation of this factor safely presumes that the bending of the cantilever

is very small such that it can be assumed to be half that of the deflection angle of the laser beam [20]. Most other methods are tedious and require specialised methods [18] for determining this factor and may additionally require precise measurement of the angles [22] (azimuthal and incidence), distance between the cantilever surface and the PSD, and so forth, which gets more complicated for beam directing methods with complex geometries using mirrors. We present here a simple plug and measure system for determining this deflection factor (G) using commercially available AFM cantilevers and applying the equipartition theorem for small cantilever deflections.

The displacement of the laser spot on the PSD (Δd) can be related to the cantilever bending (Δx) (Figure 1) using geometrical methods as [20]

$$\Delta x = \frac{\Delta d L}{4s},\tag{1}$$

where s is the distance from cantilever to the PSD, and L is the length of the cantilever. Hence, the value of Δx can be calculated based on the geometry of the setup. The absolute relationship used for relating Δx (nm) using a PSD, however, needs to include the geometrical factor needed
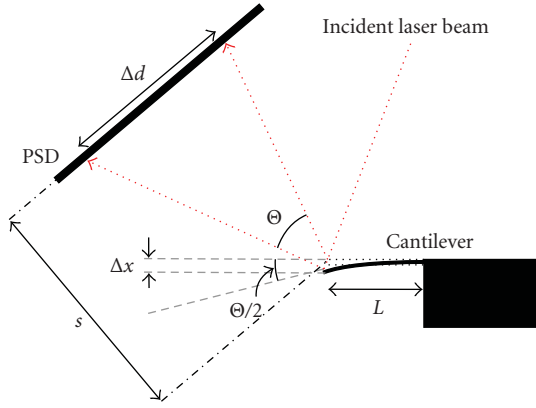
FIGURE 1: Schematic representation of the geometry of the laser deflection setup. The bending of the cantilever represented by Δx is measured by the PSD as Δd. The active length of the PSD is l_{psd}.

for a particular setup which when incorporated gives the relationship as below:

$$\Delta x = G\frac{I_1 - I_2}{I_1 + I_2}\frac{l_{psd}}{2}, \tag{2}$$

where $I_1 - I_2$ is the difference signal, and $I_1 + I_2$ is the sum signal obtained from the PSD, and l_{psd} is the active PSD length in mm. It is important to note that Δd (nm) for a PSD is generally defined as (when l_{psd} is defined in mm)

$$\Delta d = \frac{I_1 - I_2}{I_1 + I_2}\frac{l_{psd}}{2}10^6. \tag{3}$$

Equation (1) gives purely a geometrically calculated value with the aforesaid assumption that if the deflection angle of the laser is Θ, the cantilever bending angle is $\Theta/2$; it includes errors arising from differences in design and actual geometry such as the position and angle of the laser, the angle of the cantilever holder and the reflecting mirror, and the placement of the PSD. A more rigorous approach is needed to take into account not just the theoretical factors but also practical constraints of the setup.

The equipartition theorem relates the thermal energy of a system to its temperature in classical thermodynamics. Thermal noise of a cantilever can be quantified using this theorem [23, 24]. The equipartition theorem states that if a system is in thermal equilibrium, every independent quadratic term in its total energy has a mean value equal to $1/2k_B T$, where k_B is the Boltzmann constant and T is the absolute temperature. The equipartition theorem relates this total energy to the potential energy of a rectangular cantilever with a mean square deflection of the cantilever caused by thermal vibrations as follows [25]:

$$\frac{1}{2}\kappa\langle x^2 \rangle = \frac{1}{2}k_B T,$$
$$\therefore \langle x^2 \rangle = k_B T/\kappa, \tag{4}$$

where κ is the spring constant of a rectangular cantilever with finite thickness and length provided that the bending is

small. From (4), one can determine the thermal displacement of a cantilever provided that the spring constant is known. The deflection factor can hence be calculated if this thermal displacement can be related to the deflection obtained on a PSD.

Combining (2) and (4),

$$\left[G\frac{I_1 - I_2}{I_1 + I_2}\frac{l_{psd}}{2}\right]^2 = \frac{k_B T}{\kappa}. \tag{5}$$

Hence, deflection factor

$$G = \frac{2}{l_{psd}}\sqrt{\frac{k_B T}{\kappa\left(\dfrac{I_1 - I_2}{I_1 + I_2}\right)^2}}. \tag{6}$$

The term $((I_1 - I_2)/(I_1 + I_2))^2$ in the above equation is obtained from the PSD signals, using a power spectral analysis program (Virtual instrument, Labview, National Instruments) normalized to the sum signal of the PSD and is the area under the first resonance peak of a cantilever beam of known spring constant. The program essentially obtains the power spectrum which is a computation of the single-sided, scaled spectrum of the time domain signal from the PSD into the frequency domain. For a signal $x(t)$, the complex spectrum is obtained by a fast Fourier transform (FFT) defined as (in the frequency domain)

$$X(f) \equiv \int_{-\infty}^{\infty} x(t)e^{-2\pi f t}dt. \tag{7}$$

This gives, furthermore, the definition of the one sided power spectrum (in Sq. Amplitude/Hz) which is defined as

$$\text{Power spectrum}, \phi(f) \equiv \frac{|X(f)|^2}{n^2} \equiv \frac{|X(f)||X(f)|^*}{n^2}, \tag{8}$$

where n is the number of points in the signal, and $*$ denotes the complex conjugate. The integral of the power spectrum (area under the curve) provides the final value according to the Parseval's theorem which states that the area under the energy spectral density curve is equal to the total energy.

It is important to note that only the area under the first resonance peak is considered in further measurements, neglecting the higher modes since their contribution was seen to be minor (modelled as a simple harmonic oscillator with one degree of freedom). The spring constant of the calibration cantilevers hence needs to be measured as well. There are several methods available to perform such calibration to obtain spring constants [26–32] including the most frequently used thermal noise method. We chose the thermal calibration module in the Asylum MFP-3D AFM [33, 34] (Asylum research, USA) which has been shown to measure the values with relatively good accuracy and reproducibility [34]. The method records the change in PSD position as a function of cantilever angular bending when pressed against a hard surface using a closed loop piezo actuator and then converts it into values for cantilever spring constant using a predetermined sensitivity factor called inverse optical lever sensitivity. With the rest of the terms known in the equation, the calibration factor can be calculated.

TABLE 1: Manufacturer specifications of the cantilevers used for calibration factor measurement.

Specifications	Mikromasch CSC38/AIBS "B"			NTMDT CSCS12 "E"		
	Min	Typical	Max	Min	Typical	Max
Length (l) μm		350			350	
Width (w) μm		35			35	
Thickness, μm	0.7	1.0	1.3	0.9	1.0	1.1
Resonant frequency (kHz)	7	10	14	8	10	12
Force constant (N/m)	0.01	0.03	0.08	0.02	0.03	0.04

TABLE 2: Spring constants κ of the calibration cantilevers.

Spring constant	Micromasch B cantilevers		NTMDT cantilevers E	
	B1	B2	E1	E3
κ (pN/nm)	69.66	166.74	32.64	53.13
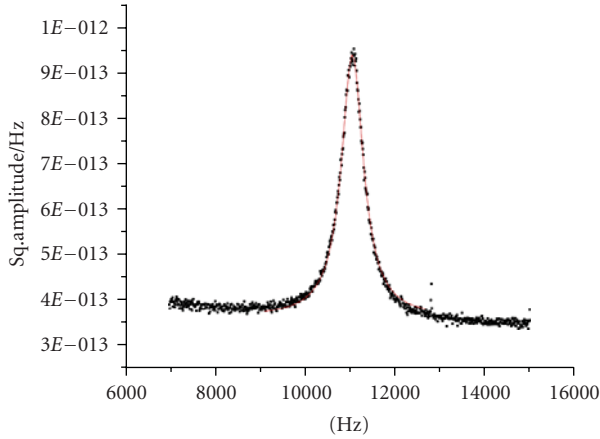
Data: Data2_B
Model: Lorentz
Equation: $y = y0 + (2*A/\mathrm{PI})*(w/(4*(x - xc)^2 + w^2))$
Weighting
y No weighting
$\chi^2/\mathrm{DoF} = 9.2491E-29$
$R^2 = 0.99638$

$y0 = 3.6454E-13 \pm 8.8807E-16$
$xc = 11057.05225 \pm 1.02355$
$W = 591.40258 \pm 3.88807$
$A = 5.3566E-10 \pm 3.2412E-12$

FIGURE 2: Thermal noise power spectrum of NTMDT cantilever E1 on trial 2 for calibration of Setup 2. The area obtained under the peak after a Lorentzian fit (uniform broadening and best fitting parameters) is later used for determining the calibration factor.

2. Materials and Methods

Different sets of commercially available AFM cantilevers were used namely Mikromasch CSC38/AIBS "B" (Mikromasch, Estonia) and NTMDT CSCS12 "E" (NT-MDT, Russia) cantilevers for the measurement of the thermal noise spectrum and final calibration. The cantilevers were calibrated using the Asylum MFP-3D AFM to get individual values for their spring constants κ. Table 1 enlists manufacturer specifications for these AFM cantilevers.

The power spectrum of the thermal noise was obtained using a 150 kHz band pass position-sensitive detector (SiTek, Sweden). This detector is a modified version of the low-pass 5 Hz sensor which is used for performing static mode biological experiments. A Labview program was used to obtain the averaged power spectrum from the differential and sum signals from the PSD. The parameters for obtaining the power spectrum had to be chosen so as to eliminate effects like aliasing which leads to truncated or artificially small resonance peaks and also electronic noise. Also it was necessary to choose the number of samples and the sampling frequency such that it avoided overloading the system and the data acquisition card (DAQ, National instruments). Keeping in mind all these details and following the Nyquist theorem (signal must be sampled at a rate at least greater than twice the highest frequency component of the signal) the parameters which were chosen for the power spectral analysis were as follows: sampling frequency: 100 kHz, number of samples: 10,000, and number of averages: 5000. The area under the first resonance peak was obtained using a Lorentzian fit in origin graphical software (OriginLab Corporation, USA). The area hence calculated along with the spring constant values was then used to determine the value of G for a particular setup. Two different cantilevers were used for the calibration of each setup with three trials on each cantilever, and the values were finally averaged. Between each trial, the cantilever was taken out of the holder chamber and reinserted. The laser power and the temperature of the chamber were kept constant for all trial measurements.

3. Results

3.1. Geometric Method for Calibration Factor. For our present instrumental scheme, the geometrical calculation for both the setups is the same as derived below. For: $s = 61$ mm (for instrument 1 and 2) and $L = 500 \mu$m.

Equation (1) can be modified to obtain

$$\Delta x = \frac{\Delta d}{488} \qquad (9)$$

TABLE 3: Calibration factors for the cantilever deflection Setups.

		Area under curve	G	Average G
		Deflection factor G setup 1		
Cant B1 ($\kappa = 69.66$ pN/nm)	Trial 1	$5.20E-10$	2128	2077.5
	Trial 2	$4.51E-10$	2284	
	Trial 3	$4.98E-10$	2175	
Cant B2 ($\kappa = 166.74$ pN/nm)	Trial 1	$2.49E-10$	1986	
	Trial 2	$2.50E-10$	1982	
	Trial 3	$2.70E-10$	1910	
		Deflection factor G setup 2		
Cant E1 ($\kappa = 32.64$ pN/nm)	Trial 1	$7.93E-10$	2517	2679.5
	Trial 2	$5.36E-10$	3062	
	Trial 3	$6.01E-10$	2891	
Cant E3 ($\kappa = 53.13$ pN/nm)	Trial 1	$3.92E-10$	2807	
	Trial 2	$5.50E-10$	2368	
	Trial 3	$5.22E-10$	2432	

Substituting Δd from (3)

$$\Delta x = 2049 \frac{I_1 - I_2}{I_1 + I_2} \frac{l_{\text{psd}}}{2}. \tag{10}$$

Comparing (2) and (10) the deflection factor G from geometric calculations is 2049 for the particular geometry and is the same for any instrument made to this scheme.

3.2. Calibration Factor G Using Equipartition Theorem

3.2.1. Determination of Spring Constants for the Cantilevers Using Asylum AFM. The spring constants for the calibration cantilevers were determined as an average of three trials during which the cantilevers were removed and replaced in the AFM setup in order to average out errors. The averaged values of the cantilevers are summarized in Table 2.

3.2.2. Thermal Noise Data Acquisition from the Instrumental Setups. Calibration factor, G was calculated for two different deflection setups both identical with respect to geometrical design using the previously mentioned cantilever sets. The power spectrum was obtained when keeping the differential signal as close as possible to zero (centre of the PSD) and the sum signal as high as possible. Figure 2 shows a sample powers pectrum obtained for Cantilever E1 on the second trial. According to the power spectrum analysis, we relate the vibrational amplitude in ambient air to the spring constant using (4).

Table 3 summarizes the results for the calibration of the instruments using the above set of cantilevers and substituting the values of the spring constant and the area under the power spectrum into (6).

From the above set of values of the G factor, it can be seen that the two setups differ from the theoretical geometric value and also from each other. The difference between the two values (the value of s differs by ~ 13.518 mm between the two when back calculated from the obtained

calibration factors) indicates that the two setups despite having similar geometry have different travel lengths of the laser from the cantilever surface to the PSD. This could be attributed mainly to the change in position and tilt of the mirror, small differences in the setting up and machining of the home made systems and angles of the cantilever holders and hence the manner in which the lasers spot is reflected by the mirror onto the PSD. It is, hence, important to note that modifications of any kind to such laser deflection systems require a recalibration especially when the differential measurements are close ranged. When compared to results from the geometric method, it is clear that the method we propose shows the variation between individual deflection setups despite their similar geometric design within reasonable error margins (5–10%).

4. Conclusions

The importance of having sensitive measurements especially in systems involving a differential analysis is of foremost significance for ensuring the reliability of cantilever sensor systems. Establishing the occurrence of an event of interest on the cantilever surface using *in situ* reference cantilevers is absolutely essential to eliminate convoluted environmental signals. Hence, a reliable method to calibrate the deflection of the cantilever is mandatory.

We demonstrate here a simple and reliable method for rapid calibration of laser-based deflection systems. Using commercially available AFM cantilevers, we can show that the relationship between the spot movement on the PSD and the actual cantilever deflection can be determined although within the accuracy of the assumptions and the thermal calibration method ($\sim$5–10%) [35]. The method was used to calibrate comparable cantilever array systems with a mirror used for deflecting the laser onto the PSD because of space restrictions. This indicates the application of the method

to more complex geometries without the need for accurate measurement of other physical parameters of the geometry.

Acknowledgments

References

[1] M. Watari, J. Galbraith, H. P. Lang et al., "Investigating the molecular mechanisms of in-plane mechanochemistry on cantilever arrays," *Journal of the American Chemical Society*, vol. 129, no. 3, pp. 601–609, 2007.

[2] F. Huber, M. Hegner, C. Gerber, H. J. Güntherodt, and H. P. Lang, "Label free analysis of transcription factors using microcantilever arrays," *Biosensors & Bioelectronics*, vol. 21, no. 8, pp. 1599–1605, 2006.

[3] J. Mertens, C. Rogero, M. Calleja et al., "Label-free detection of DNA hybridization based on hydration-induced tension in nucleic acid films," *Nature Nanotechnology*, vol. 3, no. 5, pp. 301–307, 2008.

[4] V. Tabard-Cossa, M. Godin, L. Y. Beaulieu, and P. Grütter, "A differential microcantilever-based system for measuring surface stress changes induced by electrochemical reactions," *Sensors and Actuators B*, vol. 107, no. 1, pp. 233–241, 2005.

[5] T. Braun, M. K. Ghatkesar, N. Backmann et al., "Quantitative time-resolved measurement of membrane protein-ligand interactions using microcantilever array sensors," *Nature Nanotechnology*, vol. 4, no. 3, pp. 179–185, 2009.

[6] B. Ilic, Y. Yang, and H. G. Craighead, "Virus detection using nanoelectromechanical devices," *Applied Physics Letters*, vol. 85, no. 13, pp. 2604–2606, 2004.

[7] G. H. Wu, H. Ji, K. Hansen et al., "Origin of nanomechanical cantilever motion generated from biomolecular interactions," *Proceedings of the National Academy of Sciences of the United States of America*, vol. 98, no. 4, pp. 1560–1564, 2001.

[8] J. K. Gimzewski, C. Gerber, E. Meyer, and R. R. Schlittler, "Observation of a chemical reaction using a micromechanical sensor," *Chemical Physics Letters*, vol. 217, no. 5-6, pp. 589–594, 1994.

[9] R. Berger, C. Gerber, J. K. Gimzewski, E. Meyer, and H. J. Güntherodt, "Thermal analysis using a micromechanical calorimeter," *Applied Physics Letters*, vol. 69, no. 1, pp. 40–42, 1996.

[10] T. Braun, N. Backmann, M. Vögtli et al., "Conformational change of bacteriorhodopsin quantitatively monitored by microcantilever sensors," *Biophysical Journal*, vol. 90, no. 8, pp. 2970–2977, 2006.

[11] G. Meyer and N. M. Amer, "Novel optical approach to atomic force microscopy," *Applied Physics Letters*, vol. 53, no. 12, pp. 1045–1047, 1988.

[12] S. Alexander, L. Hellemans, O. Marti et al., "An atomic-resolution atomic-force microscope implemented using an optical lever," *Journal of Applied Physics*, vol. 65, no. 1, pp. 164–167, 1989.

[13] K. A. Walther, J. Brujić, H. Li, and J. M. Fernández, "Sub-angstrom conformational changes of a single molecule captured by AFM variance analysis," *Biophysical Journal*, vol. 90, no. 10, pp. 3806–3812, 2006.

[14] C. A. J. Putman, B. G. De Grooth, N. F. Van Hulst, and J. Greve, "A theoretical comparison between interferometric and optical beam deflection technique for the measurement of cantilever displacement in AFM," *Ultramicroscopy*, vol. 42–44, pp. 1509–1513, 1992.

[15] E. J. Lee, Y. Park, C. S. Kim, and T. Kouh, "Detection sensitivity of the optical beam deflection method characterized with the optical spot size on the detector," *Current Applied Physics*, vol. 10, no. 3, pp. 834–837, 2010.

[16] A. Garcia-Valenzuela and J. Villatoro, "Noise in optical measurements of cantilever deflections," *Journal of Applied Physics*, vol. 84, no. 1, pp. 58–63, 1998.

[17] A. Garcia-Valenzuela, "Limits of different detection schemes used in the optical beam deflection method," *Journal of Applied Physics*, vol. 82, no. 3, pp. 985–988, 1997.

[18] Z. Y. Hu, T. Seeley, S. Kossek, and T. Thundat, "Calibration of optical cantilever deflection readers," *Review of Scientific Instruments*, vol. 75, no. 2, pp. 400–404, 2004.

[19] M. Godin, V. Tabard-Cossa, P. Grütter, and P. Williams, "Quantitative surface stress measurements using a microcantilever," *Applied Physics Letters*, vol. 79, no. 4, pp. 551–553, 2001.

[20] T. Miyatani and M. Fujihira, "Calibration of surface stress measurements with atomic force microscopy," *Journal of Applied Physics*, vol. 81, no. 11, pp. 7099–7115, 1997.

[21] N. P. D'Costa and J. H. Hoh, "Calibration of optical lever sensitivity for atomic force microscopy," *Review of Scientific Instruments*, vol. 66, no. 10, pp. 5096–5097, 1995.

[22] L. Y. Beaulieu, M. Godin, O. Laroche, V. Tabard-Cossa, and P. Grütter, "Calibrating laser beam deflection systems for use in atomic force microscopes and cantilever sensors," *Applied Physics Letters*, vol. 88, no. 8, Article ID 083108, 3 pages, 2006.

[23] G. Binnig, "Force microscopy," *Ultramicroscopy*, vol. 42–44, pp. 7–15, 1992.

[24] Y. Martin, C. C. Williams, and H. K. Wickramasinghe, "Atomic force microscope-force mapping and profiling on A sub 100-Å scale," *Journal of Applied Physics*, vol. 61, no. 10, pp. 4723–4729, 1987.

[25] H. J. Butt and M. Jaschke, "Calculation of thermal noise in atomic force microscopy," *Nanotechnology*, vol. 6, no. 1, pp. 1–7, 1995.

[26] R. Levy and M. Maaloum, "Measuring the spring constant of atomic force microscope cantilevers: thermal fluctuations and other methods," *Nanotechnology*, vol. 13, no. 1, pp. 33–37, 2002.

[27] S. K. Jericho and M. H. Jericho, "Device for the determination of spring constants of atomic force microscope cantilevers and micromachined springs," *Review of Scientific Instruments*, vol. 73, no. 6, pp. 2483–2485, 2002.

[28] J. L. Hutter and J. Bechhoefer, "Calibration of atomic-force microscope tips," *Review of Scientific Instruments*, vol. 64, no. 7, pp. 1868–1873, 1993.

[29] J. E. Sader, J. W. M. Chon, and P. Mulvaney, "Calibration of rectangular atomic force microscope cantilevers," *Review of Scientific Instruments*, vol. 70, no. 10, pp. 3967–3969, 1999.

[30] H. L. Ma, J. Jimenez, and R. Rajagopalan, "Brownian fluctuation spectroscopy using atomic force microscopes," *Langmuir*, vol. 16, no. 5, pp. 2254–2261, 2000.

[31] J. P. Cleveland, S. Manne, D. Bocek, and P. K. Hansma, "A nondestructive method for determining the spring constant of cantilevers for scanning force microscopy," *Review of Scientific Instruments*, vol. 64, no. 2, pp. 403–405, 1993.

[32] J. E. Sader, I. Larson, P. Mulvaney, and L. R. White, "Method for the calibration of atomic force microscope cantilevers,"

Review of Scientific Instruments, vol. 66, no. 7, pp. 3789–3798, 1995.

[33] D. A. Walters, J. P. Cleveland, N. H. Thomson et al., "Short cantilevers for atomic force microscopy," *Review of Scientific Instruments*, vol. 67, no. 10, pp. 3583–3590, 1996.

[34] R. Proksch, T. E. Schäffer, J. P. Cleveland, R. C. Callahan, and M. B. Viani, "Finite optical spot size and position corrections in thermal spring constant calibration," *Nanotechnology*, vol. 15, no. 9, pp. 1344–1350, 2004.

[35] N. A. Burnham, X. Chen, C. S. Hodges et al., "Comparison of calibration methods for atomic-force microscopy cantilevers," *Nanotechnology*, vol. 14, no. 1, pp. 1–6, 2003.

Research Article

Measurement of Hepatitis B Surface Antigen Concentrations Using a Piezoelectric Microcantilever as a Mass Sensor

Sangkyu Lee,[1] Jongyun Cho,[1] Yeolho Lee,[2] Sangmin Jeon,[3] Hyung Joon Cha,[3] and Wonkyu Moon[1]

[1] *Department of Mechanical Engineering, Pohang University of Science and Technology, Pohang 790-784, Republic of Korea*
[2] *Corporate Technology Operations SAIT, Samsung Electronics Co., Ltd., Yongin 446-712, Republic of Korea*
[3] *Department of Chemical Engineering, Pohang University of Science and Technology, Pohang 790-784, Republic of Korea*

Correspondence should be addressed to Wonkyu Moon, wkmoon@postech.ac.kr

Hepatitis B surface antigen (HBsAg) concentrations were measured using a piezoelectric microcantilever sensor (PEMS) developed by the authors. The developed PEMS is label-free and detects the sensing signal electrically. It was designed to measure the mass of biomolecules attached to it using an accurate mass-microbalancing technique; its probe area is confined to the end of the cantilever, and its equivalent spring constant is relatively high to minimize the effect of changes in the surface stress when the biomolecules are attached to it. The "dip- and-dry" technique was used to enable the probe area of the sensor to react with reagents in controlled environmental conditions. HBsAg was detected by an immunoreaction whereas the reaction time, antibody density, and its area on the probe were kept at a constant level. The mass of the detected HBsAg was measured in the range of 0.1–100 ng/mL.

1. Introduction

Hepatitis B virus (HBV) infection causes the disease hepatitis B and may also lead to cirrhosis and hepatocellular carcinoma [1]. An estimated two billion people worldwide have been infected by HBV, and of these, 350 million are chronically infected. Hepatitis B surface antigen (HBsAg) forms part of the surface of the virus and is used as a biomarker for the HBV infection [1]. We need to detect HBsAg in very low concentrations to accurately diagnose HBV. In hospitals, chemiluminescence immunoassay is widely used to detect HBsAg, and its detection limit is approximately 0.05 ng/mL [2].

A piezoelectric microcantilever sensor (PEMS) offers many advantages as a biosensor and is suitable for the detection of HBsAg. A PEMS is a highly sensitive label-free sensor that is sufficiently small to be developed as a portable device; multiplexed detection and electrical readout are also available [3]. Many studies have been conducted using a PEMS to detect various biomarkers [4].

The principle of detection in a PEMS is based on changes in the resonant frequency of the PEMS before and after a target protein is attached to it; target proteins are captured on the probe area of the PEMS by an immunoreaction. The frequency changes depend on changes in the surface stress and mass loading due to the attached biomolecules. The influence of the surface stress on the resonant frequency decreases as the effective stiffness (spring constant) of the PEMS increases [5, 6]. If we use a PEMS as a mass sensor based on a mass-microbalancing technique [7], the effective stiffness should be sufficiently large, and then, the resonant frequency will vary only in response to the mass loading effects.

The experimental setup consists of a part that measures the resonant frequency and a part that enables the probe area of the sensor to react with reagents. An impedance analyzer is usually used to measure the resonant frequency of the PEMS by detecting the peak point of the phase angle [8], dielectric loss [6], and so forth. The "dip- and-dry" technique is widely used in detection experiments [9]. The PEMS is dipped into reagents to either immobilize the antibody or bind the antigen, and the resonance frequencies are detected in air. The quality factor of the PEMS should be large because it is related to the accuracy of the detection of the resonant

frequency change. A number of studies in the literature have reported the detection of biomolecules with a PEMS that is operated in a liquid, but the quality factor is greatly reduced in liquids [10]. Environmental conditions such as humidity and temperature must be controlled at a constant level because the resonance frequency of a PEMS can be affected by these conditions.

In this study, we demonstrate the measurement of HBsAg concentrations with a PEMS we developed that functions as a mass sensor. In order for the PEMS to function as a mass sensor, it was designed to have relatively large effective stiffness and the probe area was confined to the end of the device. The "dip- and-dry" technique was used, and the masses of detected HBsAg were measured in different concentrations and with different reaction times. Moreover, a control test using other proteins was performed.

2. Piezoelectric Microcantilever as Mass Sensor

The developed PEMS was previously designed by the authors to have sufficient sensitivity and reliability as a mass sensor [7, 11]; the geometrical shape and dimensions of the sensor are shown in Figure 1(a). The piezoelectric layer is composed of lead zirconate titanate (PZT), whose composition is $Pb(Zr_{52}Ti_{48})O_3$, and the cantilever structure is made of silicon. Gold is patterned on the end of the cantilever in the probe area.

A mechanical lumped parameter model, which is shown in Figure 1(b), is used to understand the mechanical characteristics of the PEMS. The lumped parameters are calculated from the modal analysis results of the PEMS using a commercial finite element analysis tool, COMSOL Multiphysics software. The material properties and the calculated value of the lumped parameters are listed in Table 1.

The mass sensitivity of the developed PEMS is over a million times higher than that of a commercial quartz crystal microbalance (QCM). The mass sensitivity of the PEMS is approximately 175 Hz/pg, which is calculated from an eigenvalue analysis before and after the addition of mass on the probe area (Figure 1(a)), and the mass sensitivity of the widely used QCM with a 5 MHz crystal is approximately 79 Hz/μg [13]. On the other hand, both sensors are comparable in the mass sensitivity per area because the probe area of the QCM ($\sim$1.267 cm^2) is over a million times larger than that of the PEMS ($\sim$50 μm^2). The mass sensitivity per area of the PEMS is 87.5 Hz/(μg/cm^2) and that of the QCM is 100 Hz/(μg/cm^2).

Because the surface stress effect on the resonant frequency of the developed PEMS is quite small, the PEMS can be used as a mass sensor. If we assume that the initial surface stress s is zero and that the probe area covers the entire area on one side of the rectangular-shaped microcantilever, the surface stress sensitivity is shown as follows [5]:

$$\frac{1}{f_0}\frac{df}{ds} = \frac{3}{16}\frac{1}{K_{eff}}.$$ (1)

The surface stress sensitivity is inversely proportional to the effective stiffness. If the probe area is reduced to one-tenth
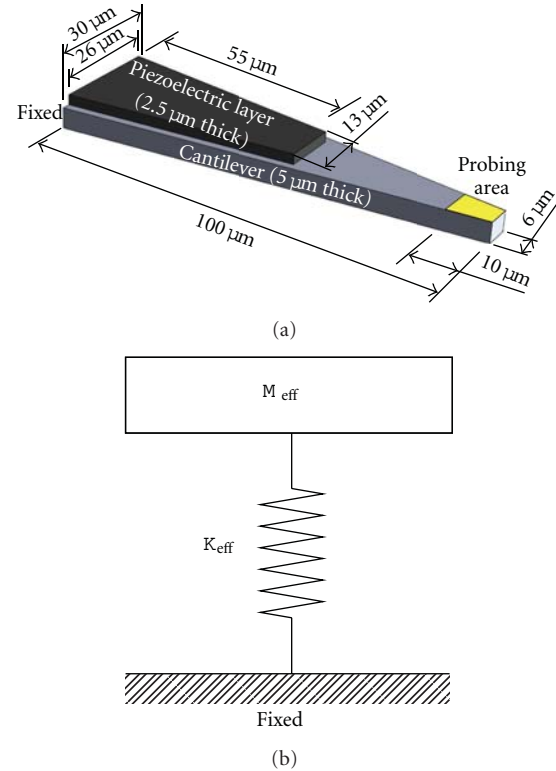

(a)

(b)

Figure 1: (a) Schematic diagram and (b) mechanical lumped parameter model of piezoelectric microcantilever sensor (PEMS).

of its original area and that area is located at the end of the cantilever, the surface stress sensitivity is reduced to approximately one quarter of its original value. The change in surface stress that is induced by the attached biomolecules is typically in the range of 0.01–0.08 N/m [6], and therefore, the change in the resonant frequency is calculated to be approximately in the range of 2.7–21.6 Hz. The frequency changes due to surface stress are less than or equal to the frequency resolution of our PEMS.

The developed PEMS was fabricated using a standard micromachining technique, the details of which are described in our previous paper [14]. Figure 2(a) shows a cross-sectional diagram, and Figure 2(b) shows an optical image of the developed PEMS. The deep trench that can be seen in Figure 2(b) was created to improve the electrical properties of the PEMS.
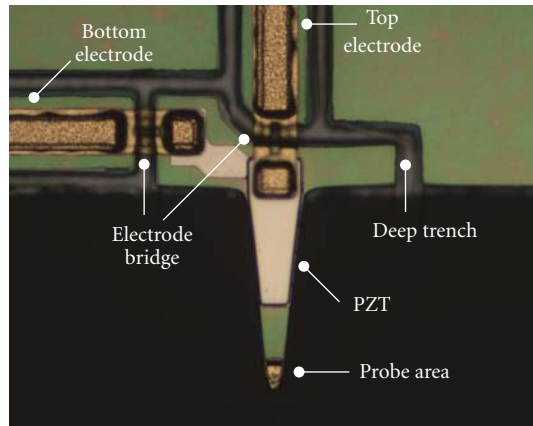
3. Experiments

3.1. Materials. Recombinant HBsAg, monoclonal anti-HBsAg, and alpha-fetoprotein (AFP) were purchased from HBI (South Korea). Phosphate-buffered saline (PBS, pH 7.4) and bovine serum albumin (BSA) were purchased from Affymetrix. Thiolated protein A/G (Protein A/G—SH) was prepared in the Magic Laboratory (POSTECH, South Korea) using Protein A/G (BioVision) and Traut's reagent (2-iminothiolane hydrochloride) according to the instructions for the Traut's reagent (number 26101, Thermo Scientific).

Table 1: Material properties and parameters used in mechanical lumped parameter model of piezoelectric microcantilever sensor (PEMS) [12].

Quantity	Unit	Value	Expression	Remark
Silicon				
E	GPa	170	Young's modulus	
ρ	kg/m^3	2329	Density	
ν		0.28	Poisson's ratio	
Piezoelectric layer				
E	GPa	Anisotropic		PZT5H
ρ	kg/m^3	7500		
Resonance frequency (f_0)	MHz	1.345479	$f_0 = (1/2\pi)\sqrt{K_{\text{eff}}/M_{\text{eff}}}$ In fundamental mode	Theoretical data
Effective stiffness (K_{eff})	N/m	234	$K_{\text{eff}} = 2E_{\text{strain}}/\delta_{\max}^2$, where E_{strain} is strain energy and $\delta_{\max}$ is the maximum displacement of the free end of the PEMS in fundamental mode	Theoretical data
Effective mass (M_{eff})	ng	3.272	$M_{\text{eff}} = k_{\text{eff}}/4\pi^2 f_0^2$	Theoretical data
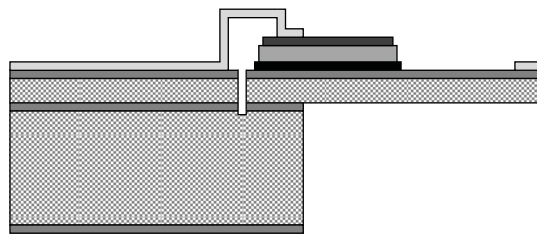
(a)

(b)

Figure 2: (a) Schematic cross-sectional diagram and (b) optical image of developed PEMS.

2-Propanol(isopropyl alcohol), ethanol, and methanol were purchased from Avantor Materials.

3.2. Experimental Setups. Figure 3 shows the experimental setups for the detection of HBsAg using the PEMS. The probe area of the PEMS was dipped into a droplet ($<10\,\mu$L) of biochemical solution, and the dipping depth was controlled using a linear stage for monitoring through a CCD camera. The resonant frequency of the PEMS was measured using a PXI system, which is a computer-based measurement device. The peak point of the conductance spectra of the PEMS is the mechanical resonant frequency [15], and the frequency at the peak point was calculated using a program developed using LabVIEW, a graphical program language. A thermo-hygrostat was used to maintain a constant humidity and temperature during the experiment.

3.3. Detection Procedure. The detection procedure used for HBsAg is shown in Figure 4, and its detailed steps are listed in Table 2. First, the sensor was subjected to a cleaning process that employed ultraviolet (UV) light (254 nm, UV-5D Short-Wave Lamp, Spectronics), and wet cleaning was also applied. Second, the gold surface on the probe area was reacted with the thiolated protein A/G, which was used to bind the antibody. Third, the sensor was passivated with BSA to prevent nonspecific binding. Fourth, anti-HBsAg was immobilized on the reaction site of the sensor. Fifth, a control test using PBS and AFP was performed for comparison with the detection results of HBsAg. Finally, the HBsAg was detected at a specific concentration while controlling the reaction time. PBS rinsing and DI water rinsing were carried out at every step, and the resonant frequency of the PEMS was also measured at every step after drying with nitrogen (N$_2$) gas. The mass of the detected HBsAg was calculated using the difference in the resonant frequency before and after detection of the HBsAg and the mass sensitivity of the PEMS. In the process of immobilizing the anti-HBsAg, the concentration and reaction time at every step was determined experimentally, as listed in Table 2. The biochemical solution in the form of droplets was replaced several times to compensate for the effect of evaporation on the concentration.
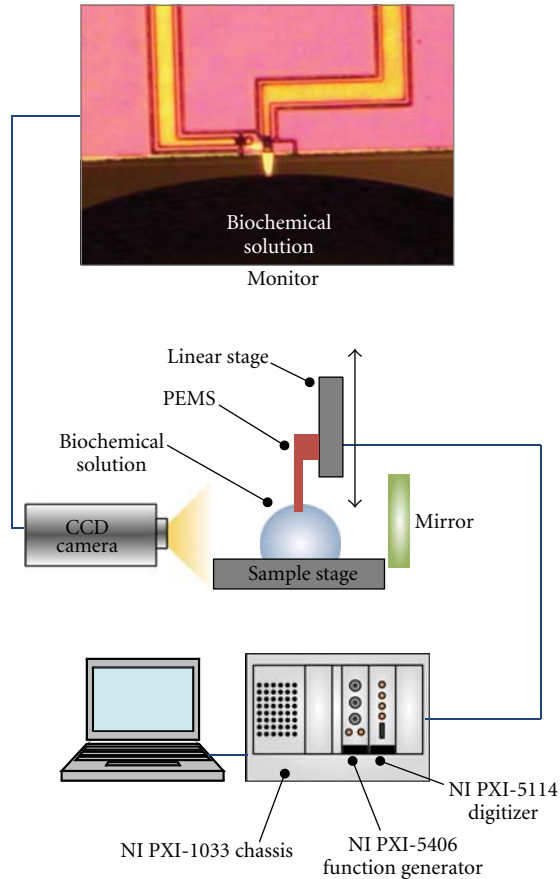
Figure 3: Experimental setups for detection of HBsAg with PEMS using "dip- and-dry" technique.

Table 2: Procedures and time requirements in detection process of HBsAg.

	Procedure	Time (min)
Sensor cleaning	UV cleaning	30
	2-Propanol cleaning	10
	Ethanol cleaning	30
	Methanol cleaning	10
	DI water rinsing	5
Protein A/G-SH	Protein A/G-SH (5 μg/mL)	40
	PBS rinsing	5
	DI rinsing	5
	N$_2$ gas dry	1
BSA	BSA (0.01%)	30
	PBS rinsing	5
	DI rinsing	5
	N$_2$ gas dry	1
Anti-HBsAg	Anti-HBsAg (25 μg/mL)	30
	PBS rinsing	5
	DI rinsing	5
	N$_2$ gas dry	1
Control	PBS	10
	DI rinsing	5
	N$_2$ gas dry	1
	AFP	10
	PBS rinsing	5
	DI rinsing	5
	N$_2$ gas dry	1
HBsAg	HBsAg	10
	PBS rinsing	5
	DI rinsing	5
	N$_2$ gas dry	1

4. Results and Discussion

The resonant frequency of the PEMS decreases after biomolecules are attached to it. Figure 5 shows the conductance spectra of the PEMS at every step in the process of immobilization of the anti-HBsAg on the probe area. The resonant frequency decreases progressively at each step. It takes less than 20 s to obtain a conductance spectrum, and the quality factor of the PEMS is approximately 200.

The mass amount of the detected HBsAg depends on the concentration of the target solution, the reaction time, the density of the immobilized anti-HBsAg, and the area it occupies on the probe. The reaction time with the target was maintained at a constant level for 10 min. Furthermore, the anti-HBsAg density and its area on the probe were almost maintained at a constant level because the probe area was defined by identical patterned gold and employing the same processes used for immobilization of the antibody. In this way, the mass amount of the HBsAg depends only on the concentration; that is, the PEMS could measure the concentration of HBsAg in the target solution by measuring the mass of the detected HBsAg.

Figure 6 shows the mass amount of detected HBsAg in the range of 0.1–100 ng/mL. As the concentration increases, the binding speed of the HBsAg also increases. Therefore, the mass amount of detected HBsAg during the reaction
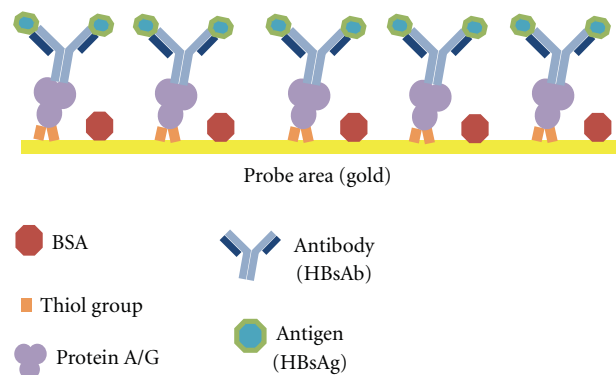

Figure 4: Procedure for detection of HBsAg with PEMS.

time of 10 min increased as expected. Figure 6 also shows the results of the measured mass that were obtained from control tests using PBS and AFP. The results for PBS are related to the minimum detectable mass, and the results for AFP are related to the binding selectivity of the detection test of HBsAg performed with the PEMS.
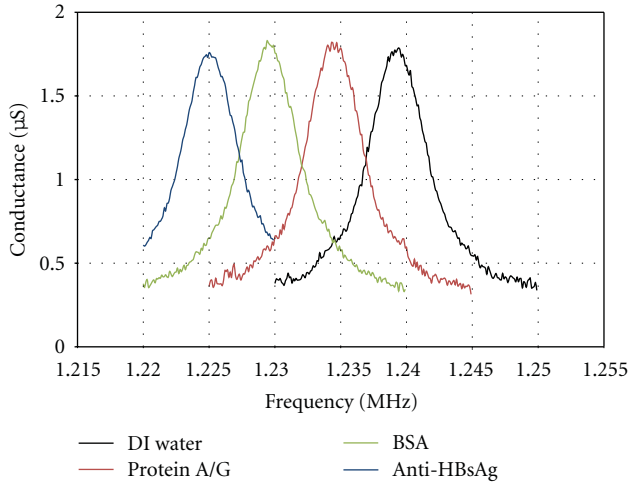
FIGURE 5: Conductance spectra of PEMS in the process of immobilizing anti-HBsAg on probe area.
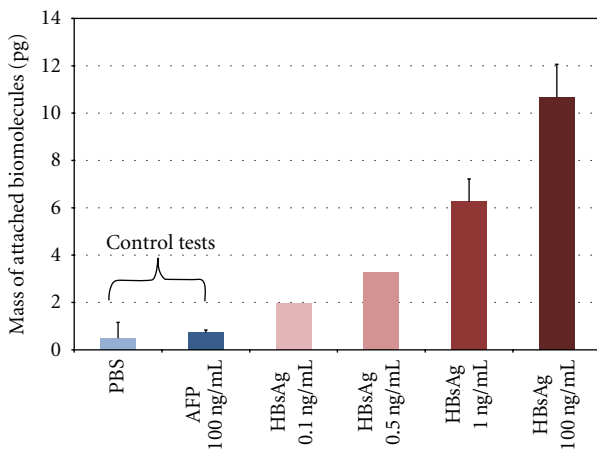

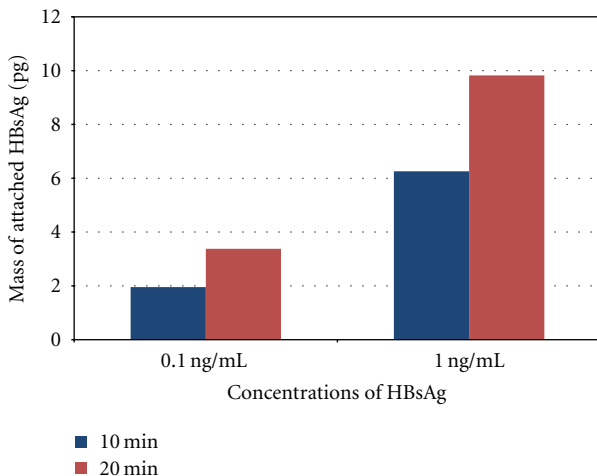FIGURE 6: Mass of detected HBsAg in several concentrations.

FIGURE 7: Time dependence of immunoreaction for different concentrations of HBsAg.

Figure 7 shows the time dependence of the immunoreaction for different concentrations. The mass increased by approximately 73% at a concentration of 0.1 ng/mL and 57% at a concentration of 1 ng/mL, as the reaction time increased twofold. The binding speed of the HBsAg may decrease as the reaction time increases because the binding speed will be zero at the saturation point; therefore, the increasing ratios of the mass of detected HBsAg are less than 100%. In addition, the increasing ratio has a lower value at a higher concentration of HBsAg because the binding speed of the HBsAg increases and then the binding reaction quickly reaches the saturation point. We need to maintain a constant reaction time while measuring the concentration of HBsAg, but we need to adjust the reaction time as the detection region of the concentration. That is, a shorter reaction time is needed in the lower concentration region and a longer reaction time is needed in the higher concentration region.

In the immunoassay, flow injection analysis (FIA) is also widely used; it allows tracking the kinetics of the immunoreaction [9] and it is relatively useful for multiplexed detection or automated system. However, FIA needs more complicated systems compared to the analysis using "dip-and-dry" technique. Furthermore, a PEMS operating in liquid has lower quality factor and lower resonant frequency due to viscous damping effect and added mass effect of the liquid [4, 7]; thus, FIA could deteriorate the reliability and sensitivity of the PEMS. Therefore, "dip- and-dry" approach is appropriate for measuring the concentration of HBsAg with the developed PEMS.

5. Conclusions

In this paper, HBsAg concentrations were measured in the range of 0.1–100 ng/mL using a PEMS that was developed for use as a mass sensor. The "dip- and-dry" technique was used, and the concentration was measured by measuring the mass of the detected HBsAg while keeping the reaction time for the target solution, the anti-HBsAg density, and its area on the probe constant. From the results obtained, we expect that the piezoelectric microcantilever mass sensor can be utilized for the measurement of the concentration of HBsAg and can also be used for sensitive diagnostic testing for HBV infection.

Acknowledgments

References

[1] S. P. S. Monga, Ed., *Molecular Pathology of Liver Diseases (Molecular Pathology Library 5)*, Springer, New York, NY, USA, 2011.

[2] S. C. Lou, S. K. Pearce, T. X. Lukaszewska, R. E. Taylor, G. T. Williams, and T. P. Leary, "An improved Abbott ARCHITECT® assay for the detection of hepatitis B virus surface antigen (HBsAg)," *Journal of Clinical Virology*, vol. 51, no. 1, pp. 59–63, 2011.

[3] K. S. Hwang, S. M. Lee, S. K. Kim, J. H. Lee, and T. S. Kim, "Micro- and nanocantilever devices and systems for biomolecule detection," *Annual Review of Analytical Chemistry*, vol. 2, pp. 77–98, 2009.

[4] S. Xu and R. Mutharasan, "Cantilever biosensors in drug discovery," *Expert Opinion on Drug Discovery*, vol. 4, no. 12, pp. 1237–1251, 2009.

[5] Q. Ren and Y. P. Zhao, "Influence of surface stress on frequency of microcantilever-based biosensors," *Microsystem Technologies*, vol. 10, no. 4, pp. 307–314, 2004.

[6] S. Shin, J. P. Kim, S. J. Sim, and J. Lee, "A multisized piezoelectric microcantilever biosensor array for the quantitative analysis of mass and surface stress," *Applied Physics Letters*, vol. 93, no. 10, Article ID 102902, 2008.

[7] Y. Lee, G. Lim, and W. Moon, "A piezoelectric micro-cantilever bio-sensor using the mass-micro-balancing technique with self-excitation," *Microsystem Technologies*, vol. 13, no. 5-6, pp. 563–567, 2007.

[8] D. W. Chun, K. S. Hwang, K. Eom et al., "Detection of the Au thin-layer in the Hz per picogram regime based on the microcantilevers," *Sensors and Actuators A: Physical*, vol. 135, no. 2, pp. 857–862, 2007.

[9] L. Nicu, M. Guirardel, F. Chambosse et al., "Resonating piezoelectric membranes for microelectromechanically based bioassay: detection of streptavidin-gold nanoparticles interaction with biotinylated DNA," *Sensors and Actuators B: Chemical*, vol. 110, no. 1, pp. 125–136, 2005.

[10] T. Kwon, K. Eom, J. Park, D. S. Yoon, H. L. Lee, and T. S. Kim, "Micromechanical observation of the kinetics of biomolecular interactions," *Applied Physics Letters*, vol. 93, no. 17, Article ID 173901, 2008.

[11] Y. Lee, *Mass detection technique using piezoelectric micro cantilever and its application to bio sensor*, Ph.D. thesis, Pohang University of Science and Technology, Pohang, Republic of Korea, 2008.

[12] S. Lee et al., "Improvements in electrical properties of piezoelectric microcantilever sensors by reducing parasitic effects," *Journal of Micromechanics and Microengineering*, vol. 21, Article ID 085015, 2011.

[13] D. Lee, M. Yoo, H. Seo et al., "Enhanced mass sensitivity of ZnO nanorod-grown quartz crystal microbalances," *Sensors and Actuators B: Chemical*, vol. 135, no. 2, pp. 444–448, 2009.

[14] Y. Lee, S. Lee, H. Seo, S. Jeon, and W. Moon, "Label-free detection of a biomarker with piezoelectric micro cantilever based on mass micro balancing," *Journal of the Association for Laboratory Automation*, vol. 13, no. 5, pp. 259–264, 2008.

[15] IEEE Standard, "177-1966—IEEE Standard Definitions and Methods of Measurements for Piezoelectric Vibrators," 1966.

Research Article

Predictions of the Compressible Fluid Model and its Comparison to Experimental Measurements of Q Factors and Flexural Resonance Frequencies for Microcantilevers

Jason Jensen and Martin Hegner

Centre for Research on Adaptive Nanostructures and Nanodevices (CRANN) and School of Physics,
Trinity College Dublin, Dublin 2, Ireland

Correspondence should be addressed to Jason Jensen, jensenja@tcd.ie and Martin Hegner, hegnerm@tcd.ie

The qualitative agreement between experimental measurements of the Q factors and flexural resonance frequencies in air of microcantilevers and calculations based on the compressible fluid model of Van Eysden and Sader (2009) is presented. The Q factors and resonance frequencies observed on two sets of cantilever arrays were slightly lower than those predicted by the model. This is attributed to the individual design and geometry of the microfabricated hinged end of the cantilever beams in the array.

1. Introduction

The introduction of the atomic force microscope [1] and the improvement of silicon fabrication technologies resulted in the ready availability of high-quality, reproducible, and inexpensive silicon cantilevers. Applications for micron-scale cantilevers as a sensing tool have been found in the fields of genomics [2–6], proteomics [7–9], microbiology [10–14], and many others. Many of these applications make use of the microcantilever as a sensitive mass detector. It has been shown that operating the cantilever at higher resonance modes increases the mass sensitivity of the device [15]. This increase in the sensitivity is linked to the increased Q factor observed for the higher flexural resonance modes of the cantilever [15]. Along with increased interest in possible applications came the need for improved understanding of the dynamics of cantilevers on this scale and models which can predict their behaviour in a range of situations. In general the higher the Q factor of the resonance peak the smaller the minimum observable frequency shift is. Thus it is desirable to obtain the highest Q factor possible during experiments to maximise the sensitivity of the experiment. Models indicating the dynamics of the cantilever

are useful when planning such experiments and determining the expected minimum response required for successful detection of the target.

Many models detailing the behaviour of microcantilevers have been proposed, including the Elmer-Dreier model [16] and Sader's viscous [17] and extended viscous models [18]. Sader's extended model includes the 3D flow field of the fluid around the cantilever beam and can be applied for arbitrary mode number.

The models mentioned above assume that the fluid in which the cantilever is vibrating is incompressible, and in general have good agreement with experimental results [19]. However, recent papers by Van Eysden and Sader [20, 21] which detail a model for a cantilever beam oscillating in a compressible fluid indicate that this unbounded increase of the quality factor is not always valid. They predict that as the mode number increases and passes a "coincidence point" (which is determined by the thickness to length ratio of the cantilever and the fluid in which the cantilever is vibrating) the Q factor will begin to decrease.

This coincidence point occurs when the length scale of spatial oscillations of the cantilever beam reduces to a point where it is comparable with the acoustic wavelength of the
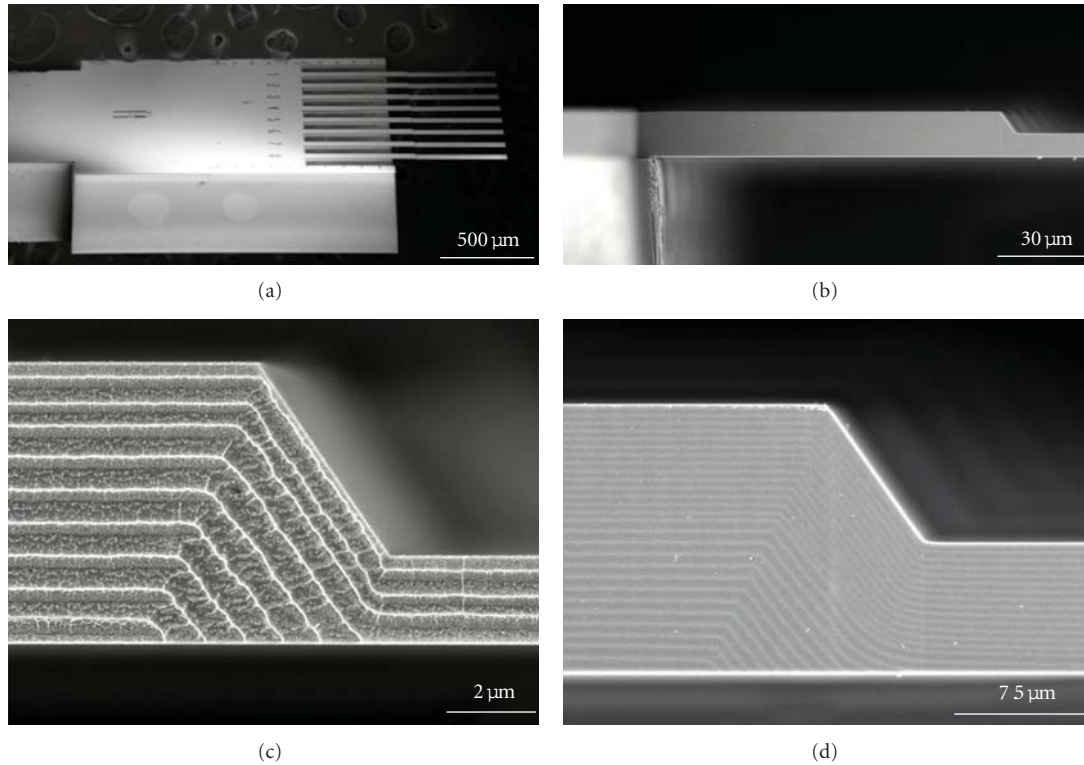
(a)

(b)

(c)

(d)

FIGURE 1: (a) SEM image of typical cantilever array used for these measurements. (b) Closer view of the hinged end of one of the $7\,\mu$m thick cantilever showing the $120\,\mu$m long hinged design that connects the cantilever with the main body of the array. (c), (d) Two closer views of the hinged portion of the 2 and $7\,\mu$m thick cantilevers, respectively. The hinge is approximately twice the thickness of the cantilever for the $7\,\mu$m thick cantilevers and approximately three times the thickness on the $2\,\mu$m thick cantilevers.

media in which the cantilever is vibrating. At this point it is possible that energy can be dissipated by the generation of acoustic waves.

For practical applications of microcantilevers (such as mass sensing) this is not an issue when operating the cantilever in liquid. However, if the cantilever is vibrated in air then it can be possible to observe this effect at higher modes. For a cantilever which is $100\,\mu$m wide, $500\,\mu$m long, and $7\,\mu$m thick the scaling analysis from the compressible fluid model [20] predicts that there should be a turning point at the $n = 3$ mode which occurs below 1 MHz. For a $2\,\mu$m thick cantilever of the same size the predicted mode is much higher ($n = 12$) and occurs around 3.6 MHz.

2. Materials and Methods

2.1. Cantilevers. The cantilevers used in these experiments are Si cantilever arrays (orientation: 110) with eight cantilevers per array (IBM Research Laboratory, Rüschlikon, Switzerland). The cantilevers had a pitch of $250\,\mu$m and were $500\,\mu$m long and $100\,\mu$m wide. The thickness of the cantilevers was measured in a scanning electron microscope (SEM, Zeiss Ultra, Cambridge, UK) and were found to be $7.2 \pm 0.5\,\mu$m and $1.972 \pm 0.005\,\mu$m thick (Figure 1). The variation in the thicknesses of the cantilevers was shown to depend on their position on the production wafer. As shown in Figure 1 the cantilevers are connected to the main

body of the chip via a $\sim 120\,\mu$m long segment which is approximately twice as thick as the cantilever itself for the $7\,\mu$m thick cantilevers and three times the thickness for the $2\,\mu$m thick cantilevers. This design was implemented to facilitate better definition between the hinge (clamping point) of the cantilever and the main body of the array.

2.2. Optical Beam Deflection Device. Thermal actuation of the cantilevers does not provide sufficient vibration of the cantilever beam to allow measurement of higher resonance modes in the current device. The cantilevers are clamped on top of a piezo electric actuator (EBL Products Inc., East Hartford, Conn, USA). The energy from the piezo is efficiently transferred to the cantilevers and provides sufficient vibration amplitudes to allow readout of the vibration modes using optical beam deflection. The cantilevers are excited at various vibrating modes by a linear frequency sweep of a sinusoidal signal which is provided by a frequency generator (NI PCI 5406, National Instruments, Tex, USA) which is controlled via a LabVIEW interface. The drive amplitude of the piezo actuator was kept low to avoid nonlinearities in the response of the cantilevers.

Optical beam deflection was used to detect the resonance frequency of the cantilever vibrations. A schematic of the device is shown in Figure 2. A single wavelength fibre coupled laser (632.99 nm, Free space power >2.4 mW, SWL 7504-P;
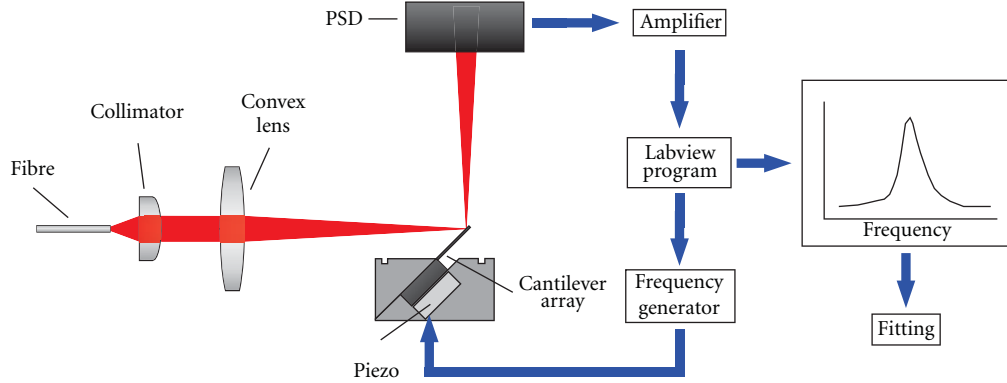
FIGURE 2: Schematic of the optical beam deflection readout procedure. The cantilever array is actuated by a piezo electric ceramic which is excited by a signal from the frequency generator. A laser spot focused onto the tip of the cantilever is deflected onto the surface of a PSD. The output from the PSD is then analysed with the signal from the frequency generator in a LabVIEW program which results in a frequency spectrum, the peaks of which correspond to the flexural resonance modes of the cantilever.

Newport, Calif, USA) was collimated into a 3.5 mm beam diameter (F280 APC-B; Thorlabs, Cambridgeshire, UK) and then focussed onto a $12\,\mu$m diameter spot on the surface of the cantilever using a 50 mm focal length convex lens (AC254-050-A1-ML; Thorlabs, Cambridgeshire, UK). The output of the laser was attenuated to avoid saturating the PSD using a neutral density filter (OD 1.3 NE513B; Thorlabs Cambridgeshire, UK).

The optic cage system which maintains the optic axis of the collimator, lens and neutral density filter was mounted on a system of two automated translation stages (M110.1DG & M122.2DD; Physik Instrumente, Bedford, UK) which allowed precise readout from each of the cantilevers in the array in a sequential manner. The motion of the stages is controlled by a LabVIEW interface. An additional microtranslation stage (Gothic Arch 9061-XYZ; Newport, Calif, USA) allows initial positioning of the laser spot at the tip of the cantilever prior to the start of an experiment.

The laser beam is deflected from the tip of the cantilever onto a linear position sensitive detector (PSD, Sitek, Partille, Sweden). The current output from the PSD is converted to a voltage with a cutoff frequency of 2 MHz (due to the response time of the optical detector). The output from the PSD is amplified (SR560 Low-Noise Preamplifier; Stanford Research Systems, Calif, USA) then digitised (NI PCI 5112; National Instruments, Tex, USA) before being analysed with the output from the frequency generator in a LabVIEW program where the time domain signal is converted into a frequency spectrum. The peaks of the spectrum correspond to the flexural resonant modes of the cantilever.

The entire device is housed inside a box which is kept at a constant temperature of $23.0 \pm 0.1°$C to avoid any drifts in the measurement due to temperature changes. The temperature is kept constant by a fuzzy logic controller which is implemented in LabVIEW.

Cantilever arrays were taken at random from the production wafers and multiple measurements of the first four flexural resonance modes were taken for the $7\,\mu$m thick cantilevers and of the first seven modes of the $2\,\mu$m thick cantilevers.

The resonance peaks obtained can be described by a simple harmonic oscillator model [22]

$$A(f) = A_{\mathrm{bl}} + \frac{A_0 f_{R,n}^2}{\sqrt{\left(f^2 - f_{R,n}^2\right)^2 + f^2 f_{R,n}^2/Q^2}},\qquad(1)$$

where A_{bl} is the amplitude of the baseline, A_0 is the zero frequency amplitude, f is the frequency, $f_{R,n}$ is the resonance frequency of mode n, and Q is the quality factor. The Q factor and resonance frequencies were extracted from the best fit of the resonance peaks with the above model using a Levenberg-Marquardt algorithm [23]. The mean and standard deviation of the resonance frequencies and Q factors of each of the modes was then calculated from the fitted data.

3. Results and Discussion

3.1. Numerical Calculations. Van Eysden and Sader's extended viscous [18] and compressible fluid models [20] were used to predict the resonance frequency and Q factor of modes of the $7\,\mu$m thick cantilevers which were below 2 MHz and the modes of the $2\,\mu$m thick cantilevers below 1 MHz. The compressible fluid model is very sensitive to the thickness of the cantilever for a given length. As shown above the thickness of the cantilevers in the array can vary significantly across the production wafer. As a result of the variation of thicknesses observed the models were used to predict the Q factors and resonance frequencies predicted for the middle and the limits of the range of thicknesses (7.2 $\pm$ 0.5 μm for the $7\,\mu$m thick cantilevers and 1.972 $\pm$ 0.005 μm for the $2\,\mu$m thick cantilevers).

The material and fluid properties were chosen to match the experimental conditions. Young's Modulus of Si: 169 GPa; density of Si (ρ_{Si}): 2330 kg/m^3; density of air (ρ_{air}) (at RT): 1.1839 kg/m^3; viscosity of air (at RT): 1.78 $\times$ 10^{-5} kg/(m s); speed of sound in air (at RT): 346.18 m/s.
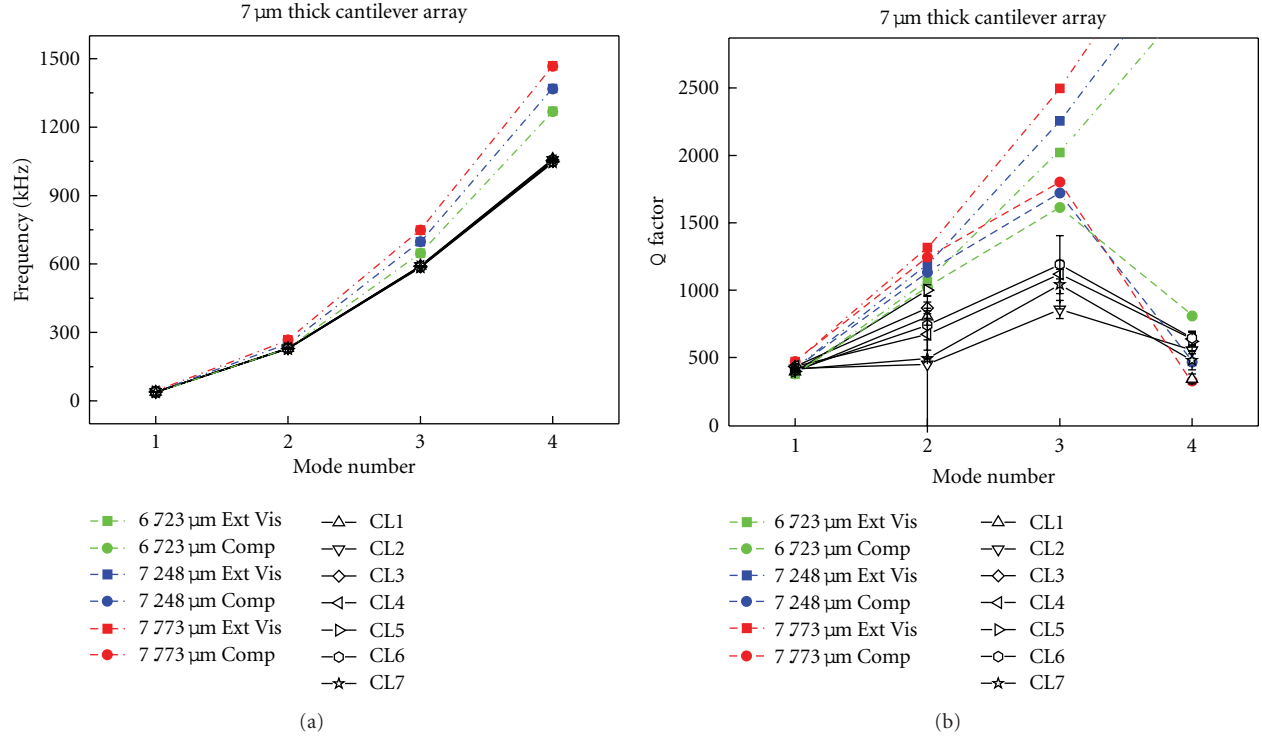
(a)

(b)

FIGURE 3: Resonance frequency and Q factor versus mode number comparison between theory and experiment for the 7 μm thick cantilevers. The solid square symbols with dotted lines correspond to the extended viscous model, while the solid circles with dashed lines correspond to the compressible fluid model. The open symbols with solid lines correspond to the experimental data. In the frequency plot the experimental data are overlapping.

The general equations for the resonance frequency and Q factor of a given mode are [18, 20]

$$
\begin{aligned}
f_{R,n} &= \frac{f_{\mathrm{vac},n}}{\sqrt{1 + (\pi\rho_{\mathrm{air}}b/4\rho_{\mathrm{Si}}t)\Gamma_r(f_{R,n}, n)}}, \\
Q &= \frac{(4\rho_{\mathrm{Si}}t/\pi\rho_{\mathrm{air}}b) + \Gamma_r(f_{R,n}, n)}{\Gamma_i(f_{R,n}, n)},
\end{aligned}
\tag{2}
$$

where t is the thickness of the cantilever, b is the width of the cantilever, $f_{\mathrm{vac},n}$ is the vacuum resonance frequency of mode n of the cantilever, and $\Gamma(f_{R,n}, n)$ is the dimensionless hydrodynamic function and the subscripts r and i refer to the real and imaginary components, respectively. The calculations of the Q factor and resonance frequencies required finding the hydrodynamic function for each of the models (it is this term that the compressibility of the fluid affects). This involved solving the systems of linear equations given in [18, equation (11)] and in [20, equation (7)]. The integer M described in the models was chosen to be 36 and was shown to provide sufficient convergence of the solution for the higher modes of vibration (data not shown). For further information on the characteristics of these functions and their convergence see references [18, 20, 24]. Mathematica 8.0 was used to perform the calculations.
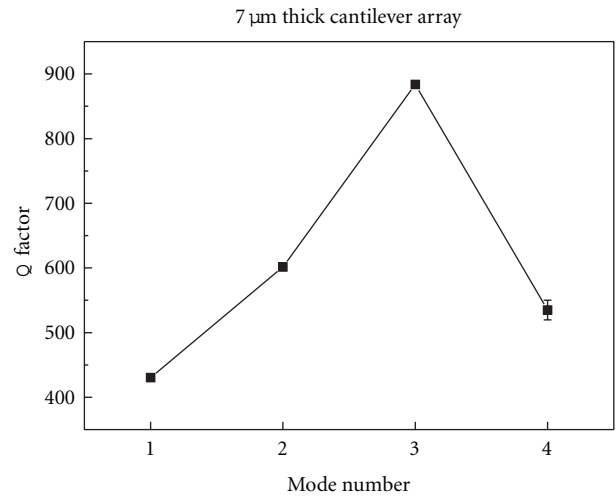

FIGURE 4: Repeated measurement of the Q factor versus mode number for a single cantilever without removing the array between measurements. The standard deviation of the Q factors for modes 1–3 is 0.003% and the standard deviation for mode 4 is 0.02%. This indicated that the previously observed larger standard deviations were due to difference in the coupling between the cantilever and the piezo between experiments.

3.2. Comparison between Theory and Experiment

3.2.1. 7 μm Thick Cantilevers. It was found that there was a decrease in the Q factor of the seven cantilever beams
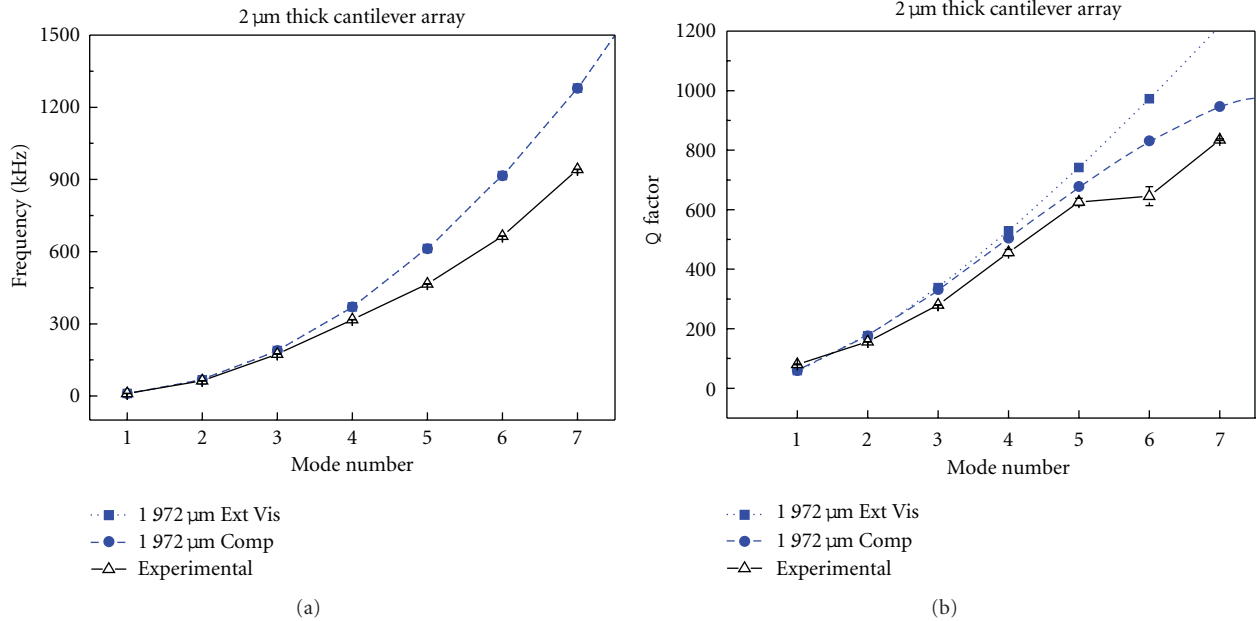
FIGURE 5: Resonance frequency and Q factor versus mode number comparison between theory and experiment for the 2 μm thick cantilever. The solid square symbols with dotted lines correspond to the extended viscous model, while the solid circles with dashed lines correspond to the compressible fluid model. The open symbols with solid lines correspond to the experimental data.

between the third and fourth modes which agrees with the prediction of the scaling analysis mentioned above that the "coincidence point" being the $n = 3$ mode. This decrease in Q factor can be clearly seen in Figure 3.

The large error bars of the experimental data shown in Figure 3 correspond to the standard deviation of the Q factor as measured from five experiments where the cantilever was unclamped and reclamped between experiments and is an indication of the coupling between the piezo and the cantilever. The standard deviation of the resonance frequencies measured for each cantilever were on the order of 0.001%. There was a difference of ~400 Hz in the fundamental frequency between cantilever 1 and cantilever 7. A similar decrease was also noted in the higher modes of the cantilevers and is an indication that there is a noticeable difference in thickness of the cantilevers within the array.

The resonance frequencies measured experimentally at the first mode agreed well with the models, however as the mode number increased the measured frequencies were increasingly lower than those predicted by the models. The lower frequencies observed are consistent with a cantilever which is longer than the cantilevers used here, but shorter than the cantilever and hinge section added together (~620 μm total length, data not shown). The strong dependence of the predictions of the compressible fluid model on the thickness of the cantilever can be observed in Figure 3.

A repeat of the experiment where the cantilever was not removed from the holder between measurements is shown in Figure 4. Here ten measurements were taken and it should be noted that the standard deviation is considerably smaller.

3.2.2. 2 μm Thick Cantilevers. The "coincidence point" predicted for a 2 μm thick cantilever was mode 12 with a resonance frequency of ~3.6 MHz. Using the current device it is not possible to observe the flexural resonance modes at such a high frequency, and therefore only the modes up to 1 MHz were observed. The hinge portion of the array is relatively thicker for these arrays than for the 7 μm thick cantilever arrays and as such should have less of an effect on the dynamics of the cantilever.

Figure 5 shows the comparison between the experimental data and the predictions of the extended viscous and compressible fluid models. It is clear that the resonance frequencies are still below those predicted by the models; however they match better than for the 7 μm thick cantilever array (16% compared to 29% difference at mode 4). This is an indication that the comparatively thinner hinge portion of the array is making a significant contribution to the dynamics of the 7 μm thick cantilever arrays.

It is clear from Figure 5 that there are differences in the predicted Q factors of the two models well below the "coincidence point". The experimental values match well with those predicted by the compressible fluid model (20% lower for the compressible fluid model compared to 75% lower for the extended viscous at mode 7).

3.3. Discussion. It is clear that the experimental data agrees qualitatively with the predictions of the compressible fluid model of Van Eysden and Sader, but that absolute quantitative agreement is not demonstrated here. Deviations of the resonance frequency and Q factors of the cantilevers between the predictions from the compressible fluid model

and the experimental findings could be due to the hinge of the cantilever being only approximately twice or three times the thickness of the cantilever (Figure 1). This may not provide a sufficiently stiff support and there may be some degree of mechanical coupling between the hinge and the cantilever beam. This is significantly more noticeable for the $7\,\mu$m thick cantilevers where the hinge is comparatively thinner and as such is an indication that the hinge is the cause of the observed deviations from the compressible fluid model predictions. The models are based on an ideal cantilever extending from a fixed support and as such should not be expected to predict exactly the behaviour of cantilevers with a hinge design such as the one used here, however theoretical geometric assumptions are not always translatable into physical microfabricated devices.

Another possible reason for a qualitative and not a quantitative result could be that the model is based on thermal actuation of the cantilever beam and here a piezo actuator is used to amplify the motion of the cantilever, and while efforts are made to keep the cantilever operating within the linear regime of the vibrations this may not be 100% successful. It should also be noted that the model is valid for cantilevers with a large aspect ratio and here the cantilevers used to conduct the experiment have a ratio of 5 which places them very near the boundary for which the theory is valid.

In conclusion it was observed that there is at least qualitative agreement with the compressible fluid model for practical microcantilevers with a thickness to length ratio of $\sim 7:500$ and an aspect ratio of 5. The prediction from the scaling analysis of Van Eysden and Sader of a "coincidence point" at mode 3 for the $7\,\mu$m thick cantilever is accurate and is clearly observed in the experimental data. The lower than predicted Q factors and resonant frequencies are likely attributed to the geometry and design of the hinge portion of the cantilever. The compressible fluid model should be considered when planning experiments involving the use of higher resonant modes of relatively thick microcantilevers in air.

Acknowledgments

References

[1] G. Binnig, C. F. Quate, and C. Gerber, "Atomic force microscope," *Physical Review Letters*, vol. 56, no. 9, pp. 930–933, 1986.

[2] R. McKendry, J. Zhang, Y. Arntz et al., "Multiple label-free biodetection and quantitative DNA-binding assays on a nanomechanical cantilever array," *Proceedings of the National Academy of Sciences of the United States of America*, vol. 99, no. 15, pp. 9783–9788, 2002.

[3] F. Huber, M. Hegner, C. Gerber, H. J. Guntherodt, and H. P. Lang, "Label free analysis of transcription factors using microcantilever arrays," *Biosensors & Bioelectronics*, vol. 21, no. 8, pp. 1599–1605, 2006.

[4] L. M. Lechuga, J. Tamayo, M. Alvarez et al., "A highly sensitive microsystem based on nanomechanical biosensors for genomics applications," *Sensors and Actuators B*, vol. 118, no. 1-2, pp. 2–10, 2006.

[5] J. Mertens, C. Rogero, M. Calleja et al., "Label-free detection of DNA hybridization based on hydration-induced tension in nucleic acid films," *Nature Nanotechnology*, vol. 3, no. 5, pp. 301–307, 2008.

[6] D. Ramos, M. Arroyo-Hernandez, E. Gil-Santos et al., "Arrays of dual nanomechanical resonators for selective biological detection," *Analytical Chemistry*, vol. 81, no. 6, pp. 2274–2279, 2009.

[7] P. S. Waggoner, M. Varshney, and H. G. Craighead, "Detection of prostate specific antigen with nanomechanical resonators," *Lab on a Chip*, vol. 9, no. 21, pp. 3095–3099, 2009.

[8] N. Backmann, C. Zahnd, F. Huber et al., "A label-free immunosensor array using single-chain antibody fragments," *Proceedings of the National Academy of Sciences of the United States of America*, vol. 102, no. 41, pp. 14587–14592, 2005.

[9] T. Braun, M. K. Ghatkesar, N. Backmann et al., "Quantitative time-resolved measurement of membrane protein-ligand interactions using microcantilever array sensors," *Nature Nanotechnology*, vol. 4, no. 3, pp. 179–185, 2009.

[10] B. Ilic, Y. Yang, and H. G. Craighead, "Virus detection using nanoelectromechanical devices," *Applied Physics Letters*, vol. 85, no. 13, pp. 2604–2606, 2004.

[11] N. Nugaeva, K. Y. Gfeller, N. Backmann, H. P. Lang, M. Duggelin, and M. Hegner, "Micromechanical cantilever array sensors for selective fungal immobilization and fast growth detection," *Biosensors & Bioelectronics*, vol. 21, no. 6, pp. 849–856, 2005.

[12] K. Y. Gfeller, N. Nugaeva, and M. Hegner, "Rapid biosensor for detection of antibiotic-selective growth of Escherichia coli," *Applied and Environmental Microbiology*, vol. 71, no. 5, pp. 2626–2631, 2005.

[13] K. Y. Gfeller, N. Nugaeva, and M. Hegner, "Micromechanical oscillators as rapid biosensor for the detection of active growth of Escherichia coli," *Biosensors & Bioelectronics*, vol. 21, no. 3, pp. 528–533, 2005.

[14] D. Ramos, J. Tamayo, J. Mertens, M. Calleja, L. G. Villanueva, and A. Zaballos, "Detection of bacteria based on the thermomechanical noise of a nanomechanical resonator: origin of the response and detection limits," *Nanotechnology*, vol. 19, no. 3, Article ID 035503, 2008.

[15] M. K. Ghatkesar, V. Barwich, T. Braun et al., "Higher modes of vibration increase mass sensitivity in nanomechanical microcantilevers," *Nanotechnology*, vol. 18, no. 44, Article ID 445502, 2007.

[16] F.-J. Elmer and M. Dreier, "Eigenfrequencies of a rectangular atomic force microscope cantilever in a medium," *Journal of Applied Physics*, vol. 81, no. 12, pp. 7709–7714, 1997.

[17] J. E. Sader, "Frequency response of cantilever beams immersed in viscous fluids with applications to the atomic force microscope," *Journal of Applied Physics*, vol. 84, no. 1, pp. 64–76, 1998.

[18] C. A. Van Eysden and J. E. Sader, "Frequency response of cantilever beams immersed in viscous fluids with applications to the atomic force microscope: arbitrary mode order," *Journal of Applied Physics*, vol. 101, no. 4, Article ID 044908, 2007.

[19] M. K. Ghatkesar, T. Braun, V. Barwich et al., "Resonating modes of vibrating microcantilevers in liquid," *Applied Physics Letters*, vol. 92, no. 4, Article ID 043106, 2008.

[20] C. A. Van Eysden and J. E. Sader, "Frequency response of cantilever beams immersed in compressible fluids with applications to the atomic force microscope," *Journal of Applied Physics*, vol. 106, no. 9, Article ID 094904, 2009.

[21] C. A. V. Van Eysden and J. E. Sader, "Compressible viscous flows generated by oscillating flexible cylinders," *Physics of Fluids*, vol. 21, no. 1, Article ID 013104, 2009.

[22] J. W. M. Chon, P. Mulvaney, and J. E. Sader, "Experimental validation of theoretical models for the frequency response of atomic force microscope cantilever beams immersed in fluids," *Journal of Applied Physics*, vol. 87, no. 8, pp. 3978–3988, 2000.

[23] K. Levenberg, "A method for the solution of certain problems in least squares," *Quarterly of Applied Mathematics*, vol. 2, pp. 164–168, 1944.

[24] C. A. Van Eysden and J. E. Sader, "Resonant frequencies of a rectangular cantilever beam immersed in a fluid," *Journal of Applied Physics*, vol. 100, no. 11, Article ID 114916, 2006.

Research Article

Fibre Optic Readout of Microcantilever Arrays for Fast Microorganism Growth Detection

N. Maloney,[1] G. Lukacs,[1] N. Nugaeva,[2] W. Grange,[3] J. P. Ramseyer,[4] J. Jensen,[1] and M. Hegner[1]

[1] *The School of Physics and The Centre for Research on Adaptive Nanostructures and Nanodevices (CRANN), Trinity College Dublin, Dublin 2, Ireland*
[2] *Toronto Western Hospital, UHN, 399 Bathurst Street, Toronto, ON M5T 2S8, Canada M5T 2S8*
[3] *Institut Jacques Monod, CNRS-Université Paris Diderot, 75205 Paris Cedex 13, France*
[4] *Department of Chemistry, University of Basel, Klingelbergstrasse 80, 4056 Basel, Switzerland*

Correspondence should be addressed to N. Maloney, maloneng@tcd.ie

We present a fibre-optic-based device for the automated readout of microcantilever arrays for fast microorganism growth detection. We determined the ability of our device to track shifts in resonance frequency due to an increase in mass on the cantilever surface or changes in mechanical stiffness. The resonance frequency response of $7\,\mu$m thick agarose-functionalised cantilevers was tracked as humidity levels were varied revealing a mass responsivity of $\sim 51 \pm 1$ pg/Hz. The resonance response of microcantilevers coated with *Aspergillus niger (A. niger)* spores was monitored for >48 h revealing a growth detection time of >4 h. The growth of mycelium along the cantilevers surface is seen to result in an increase in resonance frequency due to the reinforcement of the cantilever structure. The use of our fibre optic detection technique allows data to be recorded continuously and faster than previously reported.

1. Introduction

Microbial infection through contamination still poses a threat in areas such as the pharmaceutical, cosmetic, and food industries. For this reason, quality control tests are performed to ensure that microbial contamination does not occur and that preservatives are functional. The survival of a microbial population is dependent on the provision of suitable nutrition and environmental conditions (relative humidity > 93%, temperature = 25°C–37°C). Conventional methods to date rely on contaminating a sample containing preservatives with prescribed inocula of microorganism on a petri dish, followed by counting the colonies present. An example of this would be a preservative efficacy test for a pharmaceutical product [1] where, under the effect of the preservative living bacteria should show a log reduction of 3 after 24 h and fungi should show a log reduction of 2 after 7 days. These inexpensive manual methods provide the desired sensitivity and growth information but are time consuming and require highly skilled personnel to perform them. For

this reason, there is a need for the development of automated, highly sensitive, label-free and real-time detection systems.

The reported use of microcantilever resonators as biosensors has risen in recent years. Typically, detection is based on either (i) tracking the deflection caused by induced surface stress changes on the cantilever surface by adsorption of target biomolecules (static mode) [2, 3] or (ii) tracking the resonance frequency changes caused by mass adsorption on the cantilever surface (dynamic mode). Using static mode, single base pair mismatches have been detected in DNA hybridization experiments [4] while the detection of *Escherichia coli* (*E. coli*) has also been reported using an antibody-immobilized microcantilever with a detection limit of 1×10^6 cfu/mL [5]. Using dynamic mode, a mass resolution of 1 attogram (10^{-18} g) has been achieved [6], while the detection of bacterial cells [7], virus particles [8, 9], and biomolecules [10] has also been described. The use of microcantilever arrays for the detection of viable microorganism growth has previously been reported in [11–14]. These measurements, based on the optical beam deflection method

[15], were performed using a scanning probe MultiMode head operated in a controlled environment. Manual manipulation of the laser spot was required for the readout of several cantilevers. This paper presents the development and successful application of an automatised fibre-optic-based readout technique of cantilever arrays for microorganism growth detection. The principle of operation relies on the modulation of the optical signal, by an oscillating cantilever, carried by the optic fibres to a photodiode detector. The mechanism of detection is similar to that used in [11, 12] where the absorption of water on the functionalised cantilever surface due to microorganism growth results in a resonance frequency shift.

2. Materials and Methods

2.1. Chemicals and Reagents. All chemicals and reagents are of analytical grade and were purchased from Sigma-Aldrich (Arklow, Ireland), unless otherwise stated.

2.2. Aspergillus niger Culture Method. Aspergillus niger (*A. niger*, CIP 1431.83) spores were obtained from Institut Pasteur (Paris, France). Spores were cultured on potato dextrose agar (PDA) (Oxoid, Basel, Switzerland) slants at 35°C for five days and then stored at 4°C until required. Spores were suspended in 4 mL of malt extract broth (ME). Spores were harvested by centrifugation (10,000 rpm, 5 min) (Genofuge 16M, Techne) of 3 mL of this suspension. The resulting pellet was resuspended in a 200 μL solution of ME and deionised water (1 : 10). These steps take an average of 20 mins to complete after which the spore suspension is used for cantilever functionalisation (Section 2.3).

2.3. Cantilever Array Preparation and Functionalisation. Cantilever arrays used were obtained from the microfabrication group located in the IBM Zurich Research Laboratory. Each array consists of eight cantilevers separated by a pitch of 250 μm with length, width, and thickness dimensions of 500 μm, 100 μm, and 7 μm, respectively. Two types of array (array A and array B) were prepared. Array type A were cleaned for 10 min in Piranha solution ($H_2SO_4 : H_2O_2$; 1 : 1) and subsequently washed in a solution of nanopure water and ethanol (1 : 1) and then nanopure water. This procedure was repeated twice, and the array was then washed using HPLC grade isopropanol. Array type B was cleaned by exposing it to 0.3 mbar O_2 plasma for 3 min (PICO Barrel Asher; Diener electronic GmbH + Co. KG, Nagolderstrasse 61, D-72224 Ebhausen, Germany). After cleaning, a self-assembled monolayer was formed on the arrays by immersion in a silane solution (3-glycidyloxypropyl-trimethoxysilane : N-ethyldiisopropylamine : water free toluene; 1 : 1 : 100) for 45 min and then washed twice in water-free toluene for 15 min. The array was dried using nitrogen gas and then stored under vacuum. This step provides an epoxy-activated surface which is reactive, in alkali conditions, towards primary hydroxyl groups (e.g., agarose).

Seakem Gold Agarose (Bioconcept; NH, USA) was dissolved in nanopure water at a concentration of 1%
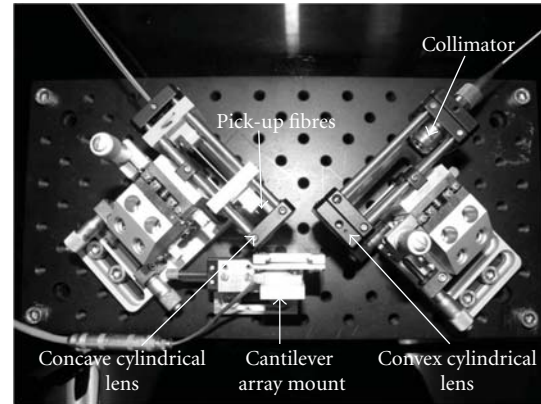

Figure 1: Photograph of fibre optic cantilever device. A collimated laser beam is focused into a line along a cantilever array using a convex cylindrical lens. The deflected signal from each cantilever is directed into one of eight optic fibres (one for each cantilever) using a concave cylindrical lens. The optical axis is maintained using two cage systems, which are mounted on two gothic arch XYZ translation stages. Horizontal distance from hole to hole is 25 mm on breadboard.

(wt/vol) and stored at 4°C. Prior to use the agarose gel solution was melted. The pH of the agarose solution was adjusted to ~11.9 by adding 2 M NaOH. Glass capillaries (King Precision Glass, Inc.; Calif, USA) were used to agarose functionalise the cantilever arrays as described in [16]. In order to prevent gelatinisation of the agarose solution in the capillary tubes, they were preheated using a radiation lamp (Osram; 8401 Winterthur, Switzerland). In the case of array type A, cantilevers were exposed to the agarose solution for 1 second. In the case of array type B, cantilevers were exposed to the agarose solution for 1, 5, or 10 seconds to obtain a different agarose thickness on each cantilever. The nutritional soaking of the agarose layer and deposition of *A. niger* spores on the cantilever were performed in parallel using glass capillaries as previously mentioned. The spore suspension used was prepared as discussed in Section 2.2. Cantilevers on array type A were immersed in the spore suspension for 10 min. The in situ reference cantilever was immersed in 10% ME broth without spores for 10 min. The array was immediately placed inside the test chamber at 94% RH and 30°C.

2.4. Apparatus and Measurement. All components were purchased from Thorlabs (Cambridgeshire CB7 4EX, UK), unless otherwise stated.v Experiments were performed using a custom built device (Figure 1) based on the optical beam deflection method. The deflected optical beam is captured using optic fibres. When actuated at its resonance frequency, the motion of a cantilever results in a modulation in the intensity of the optical beam captured by the optic fibres. By recording the intensity modulation, the resonance frequency of a cantilever can be determined and tracked. The optical axis of the device is maintained using 16 mm cage plates (SP03) and cage rods (SR3) which are mounted on two gothic-arch XYZ translation stages (9061 XYZ, Newport,
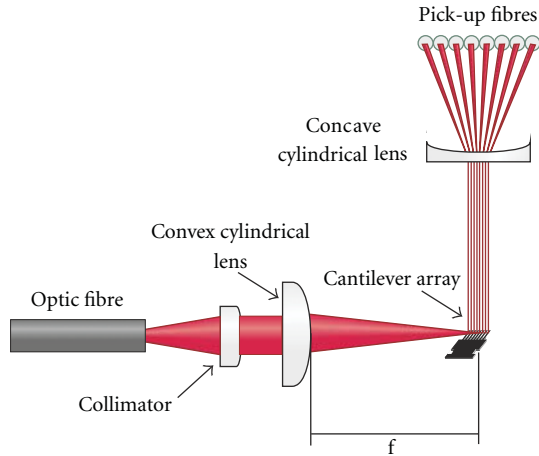
FIGURE 2: Illustration outlining optics of fibre optic cantilever device. Description is given in Section 2.4.
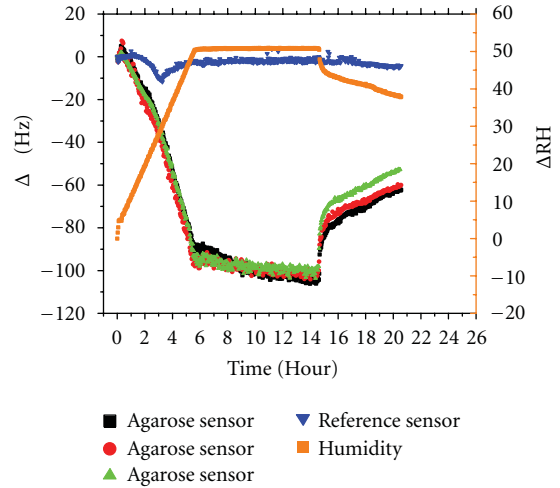

FIGURE 3: Resonance frequency response of agarose functionalised cantilevers. Agarose functionalized cantilevers show an increased response to changes in humidity. Zero point on right hand axis corresponds to 44% RH.

Calif, USA). A collimated laser beam (beam diameter = 3.4 mm) is provided to the system using a pig-tailed laser diode (LPS-830-FC, λ = 830 nm, maximum power 12 mW) which is accompanied by a collimator (F280FC-B). The laser diode is driven with an external module (ITC502-Benchtop Laser Diode and Temperature Controller ±200 mA/16 W) and is temperature controlled (TCLDM9-TE-Cooled Mount). The collimated beam is focused into a line, with a width of $\sim6\,\mu$m, along a cantilever array using a convex cylindrical lens (47764, f = 20 mm; Edmund Optics, UK). The reflection from each cantilever is directed into eight pick-up fibres (BFL48-200, core diameter = 0.2 mm), one corresponding to each cantilever in the array, via a concave cylindrical lens (LK1363L1-B, f = -7.7 mm). Figure 2 shows an illustration of this setup. The pick-up fibres are coupled to a custom built photodetector device where a voltage is produced proportional to the intensity of the detected light. The voltage generated is amplified using a low-noise voltage preamplifier (SR560, Stanford Research Systems, Calif, USA). Actuation of the cantilever array is performed using a custom made stage containing a 15 mm × 15 mm × 1 mm piezo ceramic plate (EBL#2, EBL Products Inc.; Conn, USA).

LabVIEW (National Instruments, Tex, USA) is used to control our instrument and to measure the resonance frequencies of cantilevers in an array in a time multiplexed fashion. Three boards, NI PCI-5412 (100 MS/s, 14-Bit Arbitrary Waveform Generator; National Instruments, Tex, USA), NI PCI-6010 (16-Bit, 200 kS/s, 16 Analog Input Multifunction DAQ; National Instruments, Tex, USA), and NI 5112 (High speed digitiser; National Instruments, Tex, USA), allow us (i) to output voltages on the before-mentioned piezo plate, (ii) to acquire and process voltages from the custom built photodetector device, and (iii) to control the current applied to the pigtailed laser diode.

In order to obtain suitable conditions for microorganism growth, a custom environmental chamber (5500-8139 A; Electro Tech Systems Inc., Pa, USA) is used to regulate temperature and humidity. Temperature is generated using

a heating element housed inside the chamber. Humid air is pumped into the chamber using an ultrasonic humidification system (5472-3; Electro Tech Systems Inc.; PA 19038 USA). Humidity and temperature are regulated using a temperature-compensated humidity sensor (554; Electro Tech Systems Inc, Pa, USA) in conjunction with a microprocessor controller (5200 441-431; Electro Tech Systems Inc., Pa, USA).

3. Results and Discussion

The detection of *E. coli* and *A. niger* growth using cantilever arrays has been reported in [11–14]. However, as mentioned previously, this work was performed manually using a scanning probe MultiMode head with NanoScope control software (Digital Instruments, Santa Barbara, Calif, USA). For our fibre optic device, the following tests were performed to ensure that continuous resonance frequency changes, due to increasing mass on the cantilever surface, can be detected.

3.1. Response of Agarose-Functionalised Cantilevers in Varying Humidity Conditions. Figures 3 and 4 show the resonance frequency response of cantilevers, from array types A and B, to changes in humidity, respectively. Agarose-functionalised cantilevers show an increased response to changes in humidity. This is due to an increase in mass on the cantilever surface caused by the absorption of water by the agarose layer. Increasing the incubation time in agarose solution during functionalisation results in a thicker layer and hence a greater response to humidity fluctuations (Figure 4). There is seen to be a correlation between frequency noise levels in the device and the incubation time of the cantilevers in the agarose solution during functionalisation. For incubation times of 1, 5, and 10 seconds, noise levels are found to be in the order of 4, 5.5, and 7 Hz, respectively, at experimental conditions (94% RH, 30°C) (data not shown). The mass responsivity
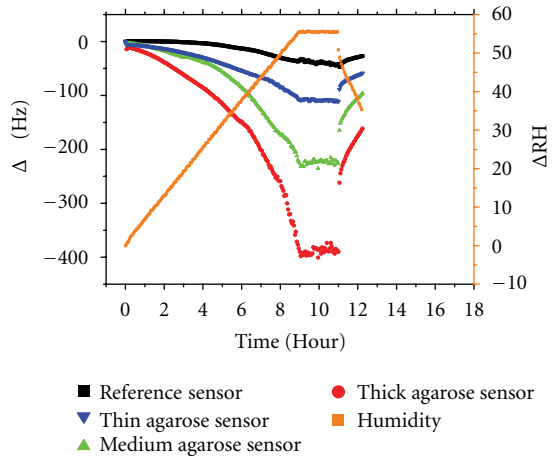
FIGURE 4: Resonance frequency response of agarose-functionalised cantilevers. The thin, medium and thick agarose sensors correspond to 1-, 5-, and 10-second incubation times during functionalisation, respectively. The response to humidity changes increases with increasing layer thickness. Frequency noise levels are also seen to increase slightly with increasing layer thickness. Zero point on right hand axis corresponds to 36% RH.

of our sensor when operated in its first resonance mode is ~51 ± 1 pg/Hz. It should be noted that the minimal detectable mass increases with the thickness of agarose on the cantilever surface due to increased noise levels.

3.2. Aspergillus niger Growth Detection. Figure 5 shows resonance frequency shift ($\Delta\omega = \omega_0 - \omega_1$) versus time for two *A. niger* spore-coated cantilevers. The observed shift is as a result of spores starting to germinate and spread mycelium along the cantilever. To put this into context, the mass of an individual spore (diameter ~4 μm) is ~34 pg, which increases to ~270 pg due to swelling before germination (diameter ~8 μm). This value is well within our detection limits indicated earlier. The growing mycelium assimilates nutrients and mostly water from the nutritive layer, which then absorbs water to remain in equilibrium with its surroundings. The detection of vital fungal growth is possible in less than 4 h. This value is in agreement with that reported in [13, 14]. The use of our fibre optic detection technique allows data to be recorded continuously. The use of an automated system allows experiments to be run over longer periods of time (>48 h) which provides further insight into the dynamics of mycelium growth. Approximately 28 h after the start of the experiment, an increase in resonance frequency, and hence most likely a rise in stiffness (k), was observed. We believe this increase to be as a result of the reinforcement of the cantilever by the growth of mycelium along its length (Figure 6). The effect of adsorbed mass stiffness and its position along the cantilever have been reported in [17, 18]. These effects may apply here; however, further work is required to clarify this as the online imaging of spore growth would be required. We believe the jumps in resonance frequency observed at ~33 and 42 h for the cantilever with the denser spore coating (Figure 6(A); black curve) could be interpreted as a temporary buckling of the
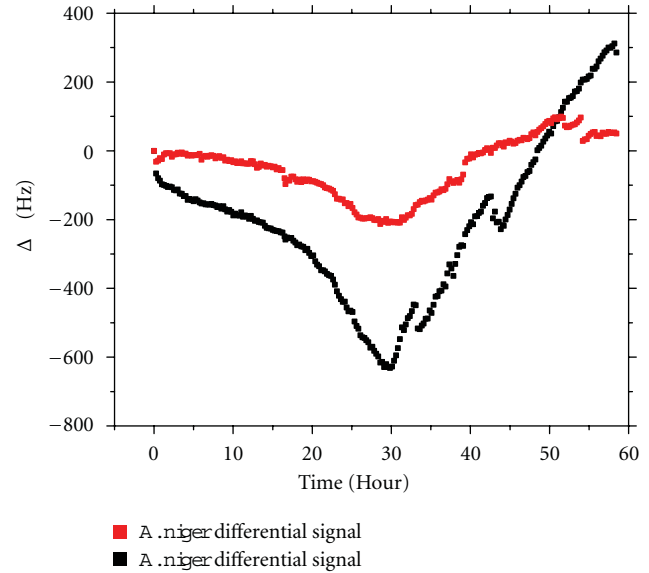

FIGURE 5: Differential nanomechanical response of *A. niger* functionalised cantilevers. The black and red curves correspond to Figure 6 (A and B, resp.). The agarose reference sensor remained stable with a standard deviation of ~15 Hz. Vital spore growth, which is manifested by a resonance frequency shift, is detected in less than 4 h. An increase in resonance frequency is also observed after ~28 h. This is due to reinforcement of cantilevers caused by the growth of mycelium along their lengths. Different numbers of viable spores on each cantilever result in different magnitudes of response; however, growth rates are the same.

strained mycelium. Different magnitudes of response can be linked to a higher number of viable spores on one cantilever than the other as can be seen in Figure 6. One point to note is that the rate of growth is the same on both cantilevers as the individual sensor response seems to scale with the number of viable spores deposited.

4. Conclusions

A new home-built cantilever array device for fast microorganism growth detection has been successfully set up. Measurements involving growth of microorganisms require high humidity and elevated temperatures that are regulated with high precision. A fibre optic detection scheme was chosen to prevent adverse humidity effects to electronic parts which would have to be placed close by the cantilever structure under these environmental conditions. The nanomechanical change, induced by the viable growth of spores on cantilever sensors, can be continuously tracked. We demonstrated that the use of fibre optic beam injection and fibre optic beam modulation readout can be used to track the resonance frequency of cantilevers in microcantilever arrays over an extended period of time under high humidity and temperature. The resonance frequency of agarose-functionalised cantilevers in varying humidity conditions was instantaneously tracked revealing a mass responsivity for the thin agarose-coated sensors of ~51 ± 1 pg/Hz. Frequency noise levels were also found to have a dependence on the thickness of the
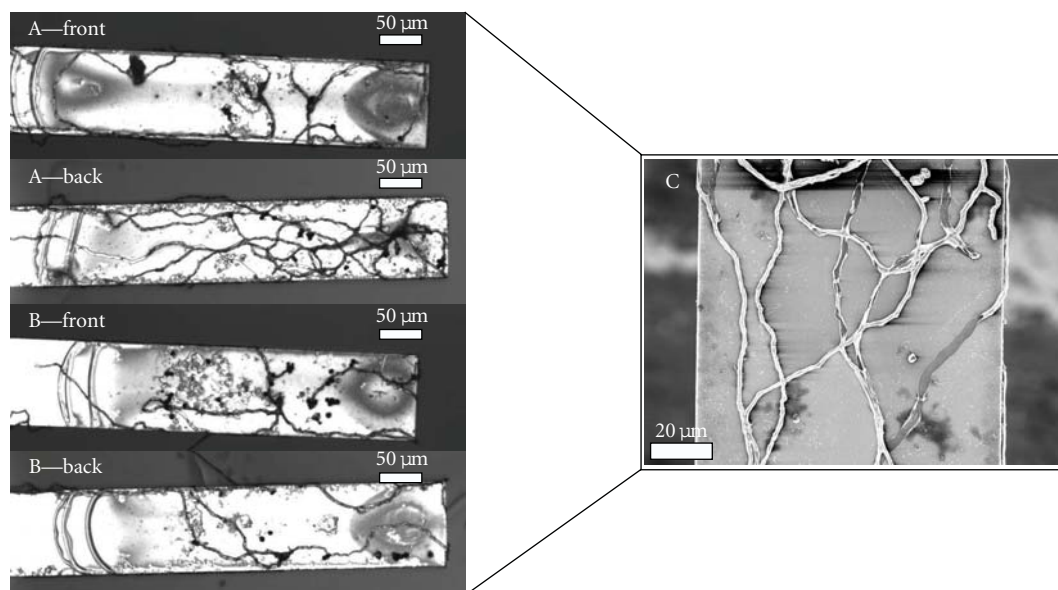
FIGURE 6: Optical microscope images of the front and backside of two *A. niger* coated cantilevers. **Figure** 6 (A and B) show the front and backsides of cantilevers which correspond to the black and red curves from **Figure** 5, respectively. Figure C shows an SEM image of mycelium on the surface of a cantilever. Mycelium thicknesses ($\sim 2\,\mu$m) are of the same order of magnitude when compared to the cantilever thickness (7 μm). The growth of mycelium proceeds at a rate of $\sim 9\,\mu$m/h along the length of cantilevers.

agarose layer favouring thin layers produced during 1 second functionalisations. The detection of growth of viable *A. niger* spores was recorded in less than 4 h. The use of an automated integrated detection system allowed nanomechanical data to be recorded continuously and growth of viable species to be monitored for >48 h, revealing additional insight into the dynamics of mycelium growth. We postulate that extended growth of micron-sized mycelium along the longitudinal axis of micron-sized cantilevers is inducing a reinforcement of the nanomechanical properties of the micron thin cantilever structures. It was observed that micromycelia are able to grow with a speed of up to $\sim 9\,\mu$m/h under optimal growth conditions and therefore have comparable dimensions to the sensors on which they are grown. The fast detection of viable microorganism, as demonstrated in this paper, is important for routine quality control tests which are required to ensure that microbial contamination does not occur and that preservatives are functional.

Acknowledgments

References

[1] EuropeanPharmacopoeia5.0, "Efficacy of Antimicrobial Preservation," 2005.

[2] N. Backmann, C. Zahnd, F. Huber et al., "A label-free immunosensor array using single-chain antibody fragments," *Proceedings of the National Academy of Sciences of the United States of America*, vol. 102, no. 41, pp. 14587–14592, 2005.

[3] T. Braun, N. Backmann, M. Vögtli et al., "Conformational change of bacteriorhodopsin quantitatively monitored by microcantilever sensors," *Biophysical Journal*, vol. 90, no. 8, pp. 2970–2977, 2006.

[4] J. Zhang, H. P. Lang, F. Huber et al., "Rapid and label-free nanomechanical detection of biomarker transcripts in human RNA," *Nature Nanotechnology*, vol. 1, no. 3, pp. 214–220, 2006.

[5] J. Zhang and H. F. Ji, "An Anti E. Coli O157:H7 antibody-immobilized microcantilever for the detection of Escherichia coli (E. coli)," *Analytical Sciences*, vol. 20, no. 4, pp. 585–587, 2004.

[6] M. Li, H. X. Tang, and M. L. Roukes, "Ultra-sensitive NEMS-based cantilevers for sensing, scanned probe and very high-frequency applications," *Nature Nanotechnology*, vol. 2, no. 2, pp. 114–120, 2007.

[7] B. Ilic, D. Czaplewski, M. Zalalutdinov et al., "Single cell detection with micromechanical oscillators," *Journal of Vacuum Science and Technology B*, vol. 19, no. 6, pp. 2825–2828, 2001.

[8] A. Gupta, D. Akin, and R. Bashir, "Single virus particle mass detection using microresonators with nanoscale thickness," *Applied Physics Letters*, vol. 84, no. 11, pp. 1976–1978, 2004.

[9] T. Braun, M. K. Ghatkesar, N. Backmann et al., "Quantitative time-resolved measurement of membrane protein-ligand interactions using microcantilever array sensors," *Nature Nanotechnology*, vol. 4, no. 3, pp. 179–185, 2009.

[10] A. K. Naik, M. S. Hanay, W. K. Hiebert, X. L. Feng, and M. L. Roukes, "Towards single-molecule nanomechanical mass spectrometry," *Nature Nanotechnology*, vol. 4, no. 7, pp. 445–450, 2009.

[11] K. Y. Gfeller, N. Nugaeva, and M. Hegner, "Rapid biosensor for detection of antibiotic-selective growth of Escherichia coli,"

Applied and Environmental Microbiology, vol. 71, no. 5, pp. 2626–2631, 2005.

[12] K. Y. Gfeller, N. Nugaeva, and M. Hegner, "Micromechanical oscillators as rapid biosensor for the detection of active growth of Escherichia coli," *Biosensors and Bioelectronics*, vol. 21, no. 3, pp. 528–533, 2005.

[13] N. Nugaeva, K. Y. Gfeller, N. Backmann et al., "An antibody-sensitized microfabricated cantilever for the growth detection of Aspergillus niger spores," *Microscopy and Microanalysis*, vol. 13, no. 1, pp. 13–17, 2007.

[14] N. Nugaeva, K. Y. Gfeller, N. Backmann, H. P. Lang, M. Düggelin, and M. Hegner, "Micromechanical cantilever array sensors for selective fungal immobilization and fast growth detection," *Biosensors and Bioelectronics*, vol. 21, no. 6, pp. 849–856, 2005.

[15] G. Meyer and N. M. Amer, "Novel optical approach to atomic force microscopy," *Applied Physics Letters*, vol. 53, no. 12, pp. 1045–1047, 1988.

[16] A. Bietsch, J. Zhang, M. Hegner, H. P. Lang, and C. Gerber, "Rapid functionalization of cantilever array sensors by inkjet printing," *Nanotechnology*, vol. 15, no. 8, pp. 873–880, 2004.

[17] J. Tamayo, D. Ramos, J. Mertens, and M. Calleja, "Effect of the adsorbate stiffness on the resonance response of microcantilever sensors," *Applied Physics Letters*, vol. 89, no. 22, Article ID 224104, 2006.

[18] D. Ramos, J. Tamayo, J. Mertens, M. Calleja, and A. Zaballos, "Origin of the response of nanomechanical resonators to bacteria adsorption," *Journal of Applied Physics*, vol. 100, no. 10, Article ID 106105, 2006.